UNIVERSITY OF CALIFORNIA
SANTA CRUZ

STRUCTURAL ENGINEERING OF CARBON AND METAL NANOSTRUCTURES FOR ANTIBACTERIAL APPLICATIONS

A dissertation submitted in partial satisfaction
of the requirements for the degree of

DOCTOR OF PHILOSOPHY

in

CHEMISTRY

by

Mauricio D. Rojas-Andrade

December 2017

The Dissertation of Mauricio D. Rojas-Andrade
is approved:

_____
Professor Shaowei Chen, Chair

_____
Professor Scott R. J. Oliver

_____
Professor Chad W. Saltikov

_____
Tyrus Miller
Vice Provost and Dean of Graduate Studies

TABLE OF CONTENTS

LIST OF FIGURES AND TABLES

ABSTRACT

STRUCTURAL ENGINEERING OF CARBON AND METAL NANOSTRUCTURES FOR ANTIBACTERIAL APPLICATIONS

by

Mauricio D. Rojas-Andrade

Antibiotic resistance is a particularly alarming issue in world health today, as the rise and prevalence of antibiotic-resistant microorganisms significantly increases death rates and costs of treatment in even the most developed nations. According to the World Health Organization, many countries around the world have observed last-resort antibiotics to be ineffective in over half of patients afflicted by common pathogenic bacteria such as *Escherichia coli* and *Staphylococcus Aureus*, necessitating the search for novel antibacterial agents. Recently, nanostructured materials have been utilized for this application, with promising results observed for a wide variety of different compositions and morphologies. This has prompted significant research efforts toward the understanding of the antimicrobial activities of nanostructured materials in order to determine the nature of their unique cytotoxic

mechanisms and consequently, the root of their antibacterial efficacy. This dissertation presents the antibacterial activities of novel carbon and metal nanostructures, focusing on the connection between their structural characteristics and their mechanisms of cytotoxicity.

In the first chapter, the antibacterial activity of silver nanostructures synthesized by a green, photochemical method is reported. By utilizing high-resolution transmission microscopy (HRTEM) and x-ray diffraction (XRD), a correlation between the surface morphology and crystal structure of silver nanostructures to their antibacterial activity is established. Silver nanostructures structures composed of (111) faceted surfaces are proposed to be more cytotoxic towards bacterial cells due to slow oxidation and fast dissolution kinetics outside and inside bacterial cells respectively. This chapter develops the foundation for silver nanostructure toxicity, with the fundamental mechanisms being applicable to all metal nanostructures.

In chapter 2, the antibacterial activities of Ag, Cu, and bimetallic, AgCu alloy nanoparticles is presented. A comprehensive characterization of Ag, Cu, and AgCu alloy nanoparticle structures is first presented, followed by a thorough analysis of their antibacterial activities. AgCu alloy nanoparticles with an average size of ~5 nm and an equal composition of Ag and Cu were found to be the most effective at inhibiting bacterial growth. The mechanisms of Ag, Cu, and AgCu alloy

nanoparticles cytotoxicity is then further investigated using fluorescence microscopy and electron paramagnetic resonance (EPR) experiments. AgCu alloy nanoparticles are concluded to exhibit their marked activity due to enhanced reactive oxygen species (ROS) generation resulting from increased Fenton reactions catalyzed by copper species stabilized in the homogenous bimetallic alloy structure.

Finally, in chapter 3, the antibacterial activity of graphene oxide quantum dots (GOQD) is reported. The as-prepared structures were synthesized through an established top-down approach, and a sodium borohydride-reduced derivative (rGOQD) was synthesized using these as the precursor. Using a variety of spectroscopic techniques, the structural properties are characterized and differences between as-prepared and reduced GOQD established. Their cytotoxicity toward bacterial cells with and without light irradiation is presented, with GOQDs demonstrating apparent activity under dark conditions, and rGOQD only under light irradiation. A mechanism of cytotoxicity and phototoxicty is proposed, which can be used to establish a foundation by which the cytotoxicity of all carbon nanostructures can be understood.

DEDICATION

I dedicate this work to my parents Isabel Andrade and Raul Rojas

The countless sacrifices you have both made throughout my life allowed me to excel further than anyone could have imagined. Your never-ending support of my educational goals gave me the strength to persevere through my greatest challenges and fulfill my dreams.

ACKNOWLEDGEMENTS

I would like to first and foremost thank my advisor, Shaowei Chen. You have been supportive throughout my academic career and taught me to think like a true scientist. I sincerely appreciate your encouragement for my interdisciplinary projects, and your considerable patience while I established the foundation for these works. Your deep insight into seemingly any science that is brought to your attention is something that I have always admired, and something I strive to achieve one day. Thank you for all the advice, guidance, and community you have shared with me on my long journey, I hope we continue to do science together for many more years to come.

Chad Saltikov, this thesis would not have been possible without your support for my work. Your council and sincere enthusiasm for my projects gave me the inspiration and motivation to do innovative interdisciplinary work, and your cheerful attitude made it enjoyable to seek your council.

Scott Oliver, you have supported me since I was a junior undergraduate and were one of the major influences for my decision to being academic research. You were always easy to talk to and come to for advice, I sincerely appreciate your encouragement and council throughout my career.

CHAPTER 1: Enhanced Antimicrobial Activity of Faceted Silver Nanostructures

1.1 Abstract

Faceted silver nanostructures including triangular nanoprisms, nanotetrahedra, and nanodecahedra were synthesized via a facile photochemical method at controlled wavelengths using spherical nanoparticles as the seeds. Scanning transmission electron microscopy studies showed that the resulting nanostructures were much larger in size (20–50 nm) than the spherical seed nanoparticles (under 5 nm), and X-ray diffraction as well as high-resolution transmission electron microscopy measurements confirmed that these nanostructures exhibited predominantly (111) faceted surfaces. Importantly, the silver nanostructures demonstrated markedly better antimicrobial activity than the spherical seed nanoparticles as evidenced by a lower minimum inhibitory concentration and more dramatic changes in both growth rate and lag phase at lower concentrations, which were attributed to the greater reactivity of the (111) faceted surfaces toward oxygen-rich bacterial surface moieties that allowed for more rapid localization to bacterial cells and increased interactions with structurally vital outer-membrane proteins. These results highlight the significance of surface morphologies of metal nanostructures in the manipulation of their antimicrobial activity.

1.2 Introduction

The biocidal effects of silver have been known for thousands of years as there is evidence of ancient Greeks incorporating silver into wound dressings to stimulate healing and storing water in silver vessels for preservation.[1] The medical uses of silver have since expanded, as the first scientific publication on its effectiveness for treating newborn postpartum eye infections opened many scientists' curiosity and led to a surge of research into the applications of silver as a biocidal agent.[2] Silver has been found to be the most promising bactericidal agent in a plethora of scenarios, attributed to its exceptional activity at relatively low concentrations and limited toxicity toward eukaryotic cells.[3] Its effectiveness stems from its broad-spectrum effect on bacterial cells, as silver ions interact with multiple cellular targets affording the biggest advantage over target-specific, small-molecule antibiotics. The mechanisms of silver toxicity have been thoroughly investigated by several groups, and there is general consensus on three primary mechanisms that lead to cell death: membrane lysis via peroxidation of structural lipids by reactive oxygen species (ROS), protein inactivation resulting from the binding and oxidation of thiol moieties on structurally relevant residues, and transcriptional arrest due to DNA condensation caused by the binding of silver ions to DNA molecules.[4] For instance, Kim *et al.* have shown evidence for ROS generation by silver ions through electron paramagnetic resonance (EPR) studies and membrane lysis of affected cells by transmission electron microscopy(TEM), lending evidence for silver's role as an initiator of membrane peroxidation.[5] In the same study, the role of free radicals as active species

was also supported as bacterial cultures having the antioxidant N-acetylcysteine added in addition to silver nanoparticles were found to have much higher survivability. Silver, as a soft acid, reacts preferentially with soft bases such as thiols which are essential components of protein tertiary structures. It has been shown that these soft–soft interactions are the underlying driving force behind silver's toxicity toward bacterial cells, as a study conducted by Xu *et al*. in 2012 comparing the toxicities of metal ions with varying softness found a trend in which softer metals such as silver, mercury, and cadmium demonstrated higher antimicrobial activity than harder metals such as zinc, nickel, and cobalt.[6] Several other groups have studied interactions of silver with thiol moieties of cysteine residues on proteins critical for cellular respiration, such as NADH dehydrogenase, which is responsible for causing cellular transcriptional arrest.[7-10] Additionally, silver has been found to react preferentially with N7 of the GC and AT base pairs of DNA and not the phosphate groups of the DNA backbone as previously thought, resulting in helix condensation and transcriptional arrest.[11] Due to the multitude of mechanisms by which silver elicits its antimicrobial activity, it has become the most promising candidate for antimicrobial applications such as surface coatings, medical wound dressings, and water filtration.

With the advent of nanotechnology, highly effective silver nanostructures have now been developed which have a markedly enhanced activity when compared to silver salts.[5, 12-15] Recent advancements have been made in delivery mechanisms for biocidal silver, with hydrogels, polymers, and porous

structures such as zeolites being utilized for both structural support and release of silver ions.[16-18] This improved activity is largely attributed to silver nanostructures having an exceptionally large surface area-to-volume ratio with smaller particles having a larger degree of exposed surface area. This enhanced active surface area affords a greater level of contact with bacterial cell walls and allows for increased rates of silver ion dissolution thereby resulting in higher bactericidal activity.[19] Pal *et al.* recently found evidence that bactericidal activity is also shape-dependent, with triangular silver nanoprisms having predominantly (111) facets demonstrating superior activity when compared to spherical and cubical nanoparticles of similar size.[20] This study indicates that the activity is highly dependent on surface structure and suggests that the silver (111) facet is most favorable for antimicrobial applications due to its high atom density. This surface structure not only increases the likelihood of silver atoms binding to bacterial cell membrane and cell wall constituents but also enhances dissolution rate of silver atoms from the nanoparticle surface via oxidation by molecular oxygen and hydroxide molecules as evidenced by cyclic voltammetry studies comparing the dissolution between different silver facets.[21] Given the evidence, nanostructures with predominantly (111) faceted surfaces warrant further investigation to shed light on the nature of their enhanced antimicrobial activity. This is the primary motivation of the present study.

Photochemical synthesis of silver nanoprisms has gained much attention since Jin *et al.* first reported a simple light-induced ripening of silver nanospheres into nanoprisms.[22] This process was found to produce triangular, hexagonal, and circular

nanoplates which were nearly flat (~10 nm thick) in high yield. The growth of these anisotropic nanostructures is the result of excitation of nanoparticle surface plasmon resonance (SPR) causing redox processes to occur preferentially at surfaces with more intense induced electromagnetic fields. Specifically, when the in-plane dipole resonance is excited, ‘‘hot’’ electrons and ‘‘hot’’ holes are generated and concentrated at surfaces on the nanoparticle in the same plane as the dipole excitation. At these surfaces, ‘‘hot’’ holes oxidize surface-bound citrate molecules into 1,3 acetonedicarboxylate and carbon dioxide though the photo-Kolbe mechanism, where the hydroxyl group of sodium citrate donates an electron pair to the central carbon atom forming a carbon–oxygen double bond which subsequently causes the central carbon to undergo heterolytic cleavage with the rest of the citrate molecule thereby releasing carbon dioxide.[23] NMR studies have previously shown supporting evidence of emerging 1,3-acetonedicarboxylate, with a corresponding peak at $\delta = 3.49$ ppm, upon photoexcitation of the silver nanospheres into triangular nanoprisms.[24] Localization of hot holes onto surface-bound citrate molecules initiates these irreversible decarboxylation reactions which transfer electrons to the silver nanoparticle causing in-plane surfaces to charge cathodically. This subsequently reduces Ag^+ ions in solution to Ag^0 resulting in selective in-plane growth.[23-25] Triangular nanoprisms are found to have a maximum induced electromagnetic field localized at the tips from electron energy loss spectroscopy (EELS) when their in-plane SPR is excited. This allows for these photo-induced redox cycles to occur most rapidly on these surfaces, which explains why these structures dominate the final

particle population after prolonged irradiation. This has indeed been observed experimentally.[26] Such a plasmon-mediated growth method provides a unique control of the structural morphology through synthetic parameters such as pH, silver ion concentration, citrate concentration, and most interestingly, excitation wavelength.[27-29] Triangular nanoprisms with varying edge-length have indeed been synthesized using the same synthetic conditions by merely varying the irradiation wavelength to excite the in-plane surface plasmon. Recently, light emitting diodes (LEDs) have also been utilized as cost-effective radiation sources and found to produce triangular nanoprisms similar in morphology and at equivalent yields.[25, 30] These resulting nanoplate structures have predominantly (111) faceted surfaces, providing a facile, energy-efficient method for the synthesis of anisotropic silver nanostructures that can be utilized to shed light on the structural root of silver nanoparticle antimicrobial activity.

In this study, a facile photochemical synthesis route is used for the preparation of anisotropic silver nanostructures by utilizing LEDs as the radiation source and only sodium citrate as the stabilizing agent. The resulting nanostructures were found to be markedly larger than the silver seed nanoparticles and comprised predominantly (111) surfaces as evidenced by HRTEM and XRD measurements. The antimicrobial efficacy of these faceted nanostructures was quantified and compared to that of the silver seed nanoparticles within the context of MIC, growth rates, and lag phase duration over a dilution series. The results indicate that the antimicrobial activity is sensitively dependent on the nanoparticle surface morphologies.

1.3 Experimental section

1.3.1 Materials

Silver nitrate (99.9 %, STREM Chemicals), sodium citrate dihydrate (Fisher), sodium borohydride powder (98 %, ACROS), Miller Luria broth (Fisher), and 4-(2-hydroxyethyl)-1-piperazineethanesulfonic acid (HEPES, 1 M, GIBCO) were used as received. All solvents were obtained from typical commercial sources and used without further treatment. Water was supplied by a Barnstead Nanopure water system (18.3 MΩ•cm).

1.3.2 Photochemical synthesis of faceted silver nanostructures

To prepare faceted silver nanostructures, silver seed nanoparticles were first synthesized through reduction of silver nitrate (0.1 mM) with sodium borohydride (0.5 mM) in the presence of sodium citrate (0.6 mM). In brief, a 250 mL three-neck flask was filled with 96.5 mL of nanopure water, and to this, 0.5 mL of 20 mM silver nitrate and 2 mL of 30 mM sodium citrate were added. The flask was bubbled with nitrogen for 30 min in an ice bath; then 1 mL of a freshly prepared, 50 mM ice-cold sodium borohydride solution was added rapidly under vigorous stirring. The solution initially turned pale yellow, then gradually into brighter yellow after about 5 min of stirring indicating the formation of small silver nanoparticles. This solution was stirred for 10 min to allow for complete reduction, and then the flask was removed from the ice bath and placed between two 40 W blue LEDs (Hongke Lighting λem =

455–475 nm) for up to 24 h, leading to the production of silver nanostructures of varied shapes. Characterizations HRTEM images were acquired with a Phillips CM300 at 300 kV, and STEM images were taken by a FEI Quanta 3D FEG dual beam SEM/FIB. About 300 individual nanostructures were counted in HRTEM and STEM images to determine particle size and shape distributions. XRD patterns were collected with a Rigaku SmartLab PXRD within the range of 20 to 80 (2 h) at a rate of 1/min and a 0.02 step size under CuKa radiation (k = 1.5418 Å). Solutions of the samples were first mixed with acetonitrile at a 1:1 ratio and lyophilized for 48 h. The resulting solid was then placed on a glass microscope slide for characterization and analyzed using PDXL-2 software. UV–vis spectra were acquired by an Agilent Cary-60 UV–vis spectrometer, and bacterial optical density was measured in a Molecular Devices VERSAmax microplate reader.

1.3.3 Bacterial Growth Assays

Escherichia coli (ATCC# 25922) was first grown by spreading frozen liquid culture (20 % glycerol, -72 C) on Luria broth (LB) agar and incubating at 37 °C overnight. From this plate, a single colony was selected and used to inoculate 3 mL of liquid LB and allowed to shake at 37 °C for 18 h. The resulting overnight liquid culture was centrifuged at 5000 rpm for 5 min and re-suspended in a sterile aqueous 20 mM HEPES solution. The re suspension was diluted with fresh HEPES solution to

an optical density of 0.10 at 600 nm and used for inoculation. A 96-well plate was used to contain all of the growth solutions with each wellbeing filled to a final volume of 200 μL with 80 μL of sterile LB, 20 μL of the inoculation solution, and varying volumes (100, 90, 80, 70, 60, 50, and 40 μL) of each antimicrobial agent and enough water to bring the final volume to 200 μL. Immediately upon inoculation, the 96-well plate was placed in the plate reader where the optical density at 600 nm for each well was measured every minute with 10 s mixing periods between reads over the 18 h incubation period at 37 °C.

1.4 Results and Discussion

1.4.1 Photochemical Synthesis and Characterizations of Faceted Silver Nanostructures

Silver seed nanoparticles were first prepared by chemical reduction of silver nitrate with sodium borohydride in the presence of sodium citrate in water. **Figure 1 a** depicts a representative TEM micrograph of the resulting nanoparticles. One can see that the seed nanoparticles are mostly spherical in shape, and statistical analysis based on about 300 nanoparticles showed a nearly unimodal distribution of the particle size with approximately 80 % of the particles having a diameter less than 5 nm, and the average diameter was estimated to be 4.76 ± 3.88 nm, as manifested in the core size histogram in panel (c). In addition, well-defined crystalline lattice fringes can be seen in high-magnification TEM studies, as manifested in the top inset to panel (a) where the lattice spacing was estimated to be 0.231 nm, closely matching

the value for fcc Ag(111) planes.[31] Consistent results were obtained in selected-area electron diffraction (SAED) that is depicted in the lower inset, where the circles are consistent with fcc Ag(111). Interestingly, three dotted lines can also be seen, suggesting the formation of an hcp phase within the nanoparticles, which is consistent with results from the XRD measurements (*vide infra*).[32] In contrast, after irradiation for 24 h by blue LEDs (455–475 nm), the size and shape of the silver nanoparticles exhibited a drastic change, as shown in **Figure 1b**. First, one can see that the nanoparticles are now significantly larger and composed of a number of interesting shapes. For instance, both sharp-tipped and truncated triangular nanoprisms can be seen in the micrograph with the edge-lengths varying from 10 to 40 nm, as depicted in panel (D). Other unique nanostructures such as decahedra and tetrahedra can also be identified, which were likely formed by thickening and edge-selective fusion of the triangular nanoprisms.[33, 34] Such structures have also been observed in early studies and thought to originate from crystal twinning of the initial seed nanoparticles.[25, 35-40] For instance, Zheng *et al.* studied the effect of LED excitation wavelength on the shape distribution of the resulting nanostructures and found that under 455 nm irradiation, nanodecahedra were the predominant species, but when 519 nm light was used, triangular nanoprisms were the major species.[38] In the present study, the structural distribution (**Figure S1**) obtained

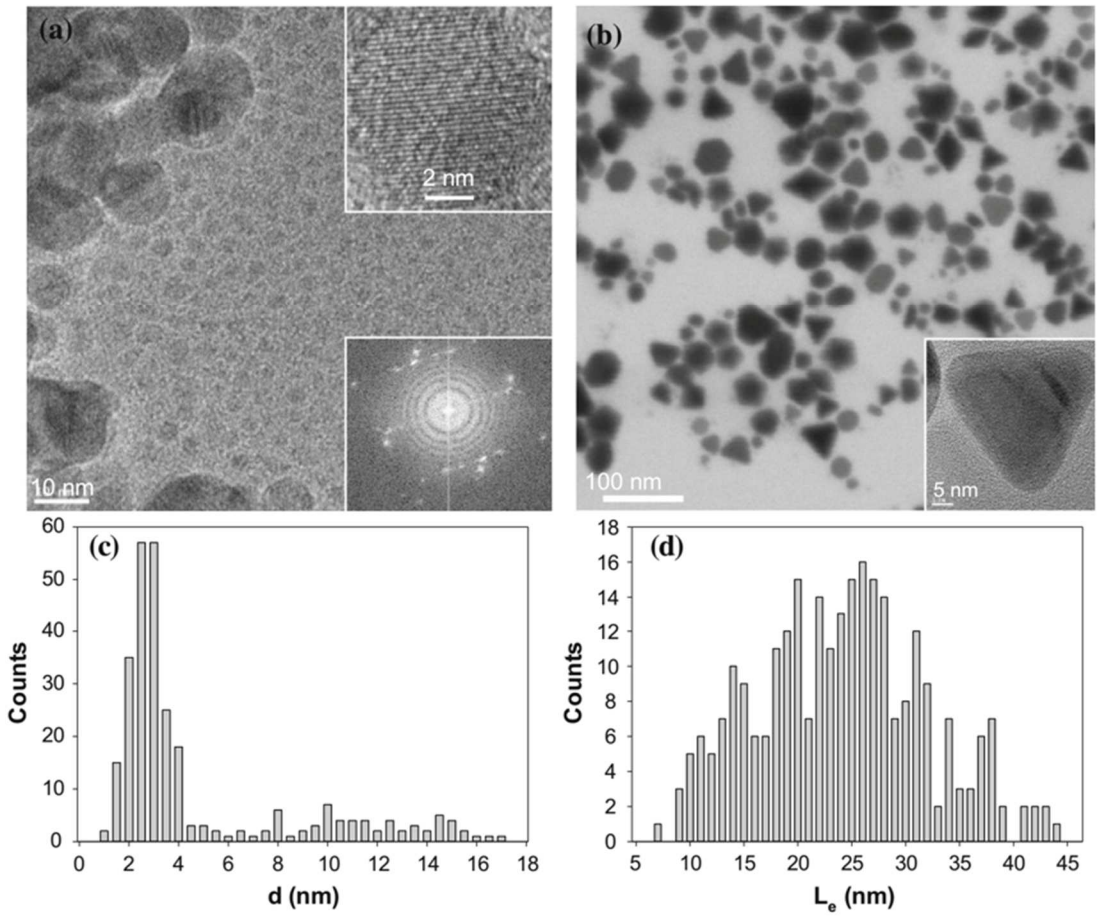

Figure 1. Representative TEM images of (a) silver seed nanoparticles and (b) nanostructures prepared by irradiation of silver seeds for 24 h. Scale bar in a 10 and 200 nm in (b). Top inset to pane a is a representative HETEM image that highlights the silver lattice fringes (Scale bar 2 nm) and the bottom inset is a diffraction pattern acquired from selected area electron diffraction. Inset to panel (b) is a representative HRTEM image of a silver nanoprism. Scale bar 5 nm. Histograms of **c** particle diameter for silver seed nanoparticles and (d) edge length for irradiated nanoparticles

from the TEM study presented above shows that decahedral nanoparticles accounted for only 27 % of all structures observed, whereas sharp-tipped and truncated triangular nanoprisms represented approximately 50 % of the population. In contrast, the overall yield of decahedral structures obtained by Zheng *et al.* was much higher

(~90 %). This is likely due to their use of PVP as a shape directing stabilizer, as it binds preferentially to silver (100) facets and likely promotes the growth of triangular nanoprisms into nanotetrahedra and their subsequent fusion into nanodecahedra. Lattice fringes of the resulting silver nanostructures are also very well defined, as depicted by the high-resolution TEM image in the inset to **Figure 1b**, where fcc Ag(111) crystal planes can be identified with an interlayer spacing of 2.37 Å . Additionally, domains with a somewhat larger lattice spacing of 2.47 Å can also be seen (**Figure S2**). This might be attributed to internal stacking faults parallel to the basal (111) faces that created local hcp regions within the nanostructure and hence caused elongation along the (111) direction.[41, 42] Consistent results were obtained in XRD measurements (vide infra). The structural evolution was manifested in UV–vis absorption spectroscopic measurements, as depicted in **Figure 2**. It can be seen that for the seed nanoparticles (black curve), an absorption band at λ_{max} = 390 nm can be readily identified, which is the characteristic SPR of small silver nanoparticles.[43] Upon irradiation by the LED lights, the nanoparticle solution gradually changed in color from yellow to orange indicating the formation of anisotropic silver nanostructures. In fact, this might be monitored directly by acquiring the solution's UV–vis profiles over a 4 h irradiation period with a 30-min induction period as depicted in **Figure 2**. One can see that upon irradiation, the absorption at 390 nm began to decline and concurrently, new peaks at 475 and 343 nm started to emerge and grow (black arrows), forming an isosbestic point at about 435 nm (red arrow). These new absorption features were characteristic of the in-plane dipole (475

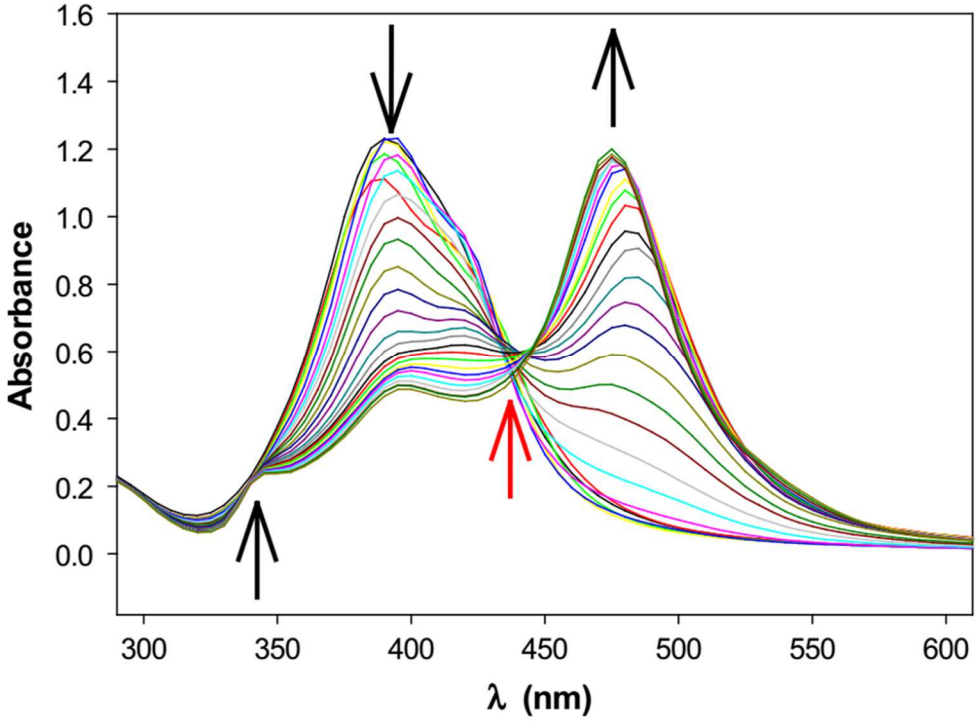

Figure 2. UV–Vis spectra of a silver nanoparticle solution over a 4 h irradiation period illustrating the process of photo-conversion from spherical seed particles to nanoprisms. Black arrows signify the evolution of the absorption peaks and red arrow indicates the isosbestic point.

nm), in-plane quadrupole (390 nm), and out-of-plane dipole (343 nm) plasmon resonances of silver nanoprisms, respectively.[27, 29] Similar absorption features have also been observed with silver nanotetrahedra and nanodecahedra.[35, 38] Additionally, the in-plane dipole resonance peak was found to blue shift somewhat over more prolonged irradiation time going from 475 nm after 4 h of irradiation to 465 nm after 24 h of irradiation, which is likely due to gradual truncation of the as-formed triangular nanoprisms. This truncation is caused by a decline of preferential in-plane growth, likely due to diminishing citrate concentration resulting in a decreasing

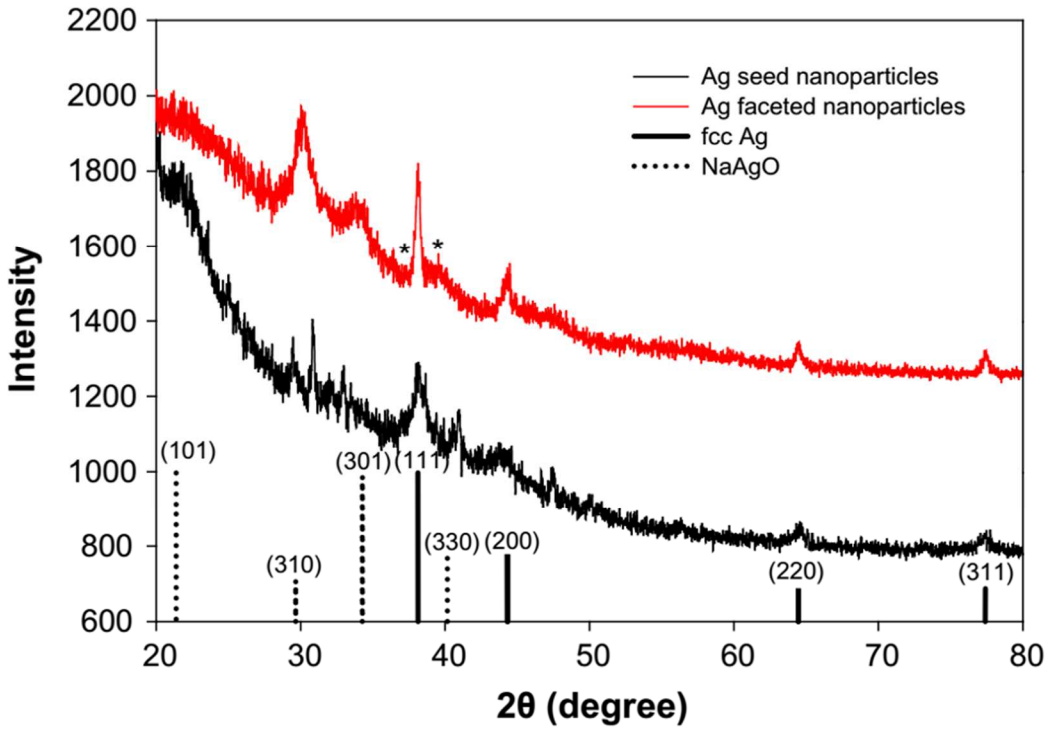

Figure 3. XRD spectra of silver seed nanoparticles and faceted nanostructures with reference lines corresponding to fcc metallic silver and NaAgO obtained from the ICDD database. Asterisks signify the hcp peaks.

surface coverage of the (111) facets by the protecting ligands, as well as gradual excitation of the in-plane quadruple SPR of existing triangular nanoprisms which caused localization of hot charge carriers along the edges of triangular nanoprisms and promoted growth perpendicular to the basal (111) planes of the structures.[24, 44] Note that once irradiation was turned off, the resulting faceted nanoparticles remained structurally stable in ambient as manifested by a virtually invariant UV–vis absorption profile. More insights about the crystalline structures were obtained in XRD measurements. It can be seen from **Figure 3** that the faceted nanostructures (red

curve) exhibited a series of diffraction peaks that are consistent with fcc silver (solid bars, JCPDS 00-004 0783) at 37.9° (111), 44.5° (200), 64.5° (220), and 77.5° (311). Three additional peaks can also be seen at 21.8, 30.0, and 34.4 that might be assigned to the diffractions of NaAgO (101), (310), and (311) crystalline planes (dotted bars, JCPDS 01-088-1567), respectively, suggesting the formation of silver oxide on the nanostructure surface. Furthermore, the faceted nanostructures also exhibited a broad peak at 39.2°, along with an even weaker one at 37.2° (labeled with asterisks), which suggests the formation of an hcp lattice arrangement, consistent with the TEM results presented above in **Figure 1**.[32, 39, 42] A similar diffraction profile can be seen with the seed nanoparticles as well (black curve), except that the diffraction for the silver oxide (330) at 40.9° became apparent, whereas the (301) peak at 34.4° diminished. One may also see that the Ag(111) diffraction peak was much more intense with the faceted nanostructures than with the seed nanoparticles, indicating a marked increase of the crystalline (111) facets, in agreement with HRTEM studies (**Figure 1**).[45] Overall, one can see an increase in size of the faceted nanostructures from the initial spherical particles after irradiation, as evidenced by measurements of the particle diameter if spherical and edge-length if triangular, tetragonal, or decahedral. This is expected as photoexcitation results in an increased rate of photo-induced redox cycles for structures having SPR modes in the LED emission range leading to growth along the planes of the excited SPR over time. This process is also reflected in the almost complete absence of spherical particles after 24 h of irradiation as oxidation of the small (<10 nm) particles provides the source of Ag^+ ions for nanoprism growth due to

their lower redox potentials than those of larger particles.[46, 47] Due to this photo-mediated growth process, solutions irradiated for longer periods of time exhibited a higher concentration of silver nanostructures with surfaces composed primarily of (111) facets. These nanostructures therefore serve as an appropriate means by which to relate the nanoparticle surface structure to antimicrobial activity, as detailed below.

1.4.2 Antimicrobial Activity

The antimicrobial activity of the silver seed nanoparticles and faceted nanostructures was then quantified and compared by monitoring the growth of *E. coli* cultures in liquid media over time. A 96-well plate with a dilution series of each sample was used to characterize the concentration dependence of relevant growth parameters. The most important of these parameters is the minimum inhibitory concentration (MIC), defined as the concentration of an antimicrobial agent at which bacterial cultures demonstrate no observed growth throughout the incubation period as evidenced by a lack of increase in optical density at 600 nm that corresponds to light scattering of bacterial cells. In this study, 20 μL of an *E. coli* suspension with an optical density of 0.1 at 600 nm (corresponding to an initial cell density of approximately 1.67×10^7 cells/mL[48]) in aqueous 20 mM HEPES was added to a dilution series of the silver seed nanoparticles and faceted nanostructures prepared by irradiation for 24 h. From the growth curves depicted in **Figure 4**, two general trends were noted. First, from these growth curves, it is clear that solutions of both the as-prepared seed nanoparticles and LED-irradiated silver nanostructures exhibited an

inhibitory effect on the growth of the *E. coli* colonies when compared with the blank control. Second, the faceted nanostructures clearly showed enhanced antimicrobial activity as compared to the seed nanoparticles, with an MIC of 4.9 and 5.4 μg/mL, respectively. This is somewhat surprising as the seed nanoparticles are much smaller in size than the faceted nanostructures (**Figure 1**), and thus, with their greater effective surface area, one would anticipate greater membrane penetration capability. In fact, such a behavior has been observed by Agnihotri *et al.* in a study of the antimicrobial activity of silver nanoparticles within the size range of 5–100 nm.[49] However, in the present study, as depicted in **Figure 1c** and **1d**, size distributions acquired by analysis of TEM images show that the faceted nanostructures contained mostly particles between 20 and 40 nm in diameter/edge-length with only 10 % of the particles having a diameter less than 10 nm. In stark contrast, 80 % of the seed nanoparticles had a diameter of less than 5 nm and only 14 % having diameters greater than 10 nm. Therefore, the enhanced activity of the faceted nanostructures strongly suggests that surface morphologies might actually play a dominant role in the determination of the antimicrobial activity. As triangular nanoprisms, nanotetrahedra, and nanodecahedra are faceted predominantly by highly reactive (111) surfaces, these nanostructures exhibit an exceptionally strong affinity to sulfur-containing membrane proteins and oxygen-containing functional groups of lipopolysaccharide molecules which constitute 25 % and 75 % of cell wall surfaces, respectively.[21, 50, 51] This would allow these highly faceted silver nanostructures to efficiently localize to *E. coli* cell walls, penetrate the outer membrane, and release

silver ions into the periplasmic space. These ions would then bind to peptidoglycan polymers, resulting in disruption of cell wall synthesis and rapid entry of silver ions into the cytoplasm which allows silver to exert its toxic effects to intercellular targets such as DNA, as well as eventual membrane lysis from turgor pressure. Additionally, due to their larger size, these nanostructures might easily cause a major disruption of the cell membrane once localized as they would interact with a greater number of cell wall targets per particle compared with the smaller, spherical seed nanoparticles. Localization of these larger structures to the cell walls would therefore result in physical membrane lysis through structural distortion as well as through free radical-induced peroxidation of membrane lipids due to ROS generation, which has been suggested by previous studies.[4, 52] Furthermore, membrane disruption also causes changes in membrane permeability which would adversely affect cellular respiration and inhibit the metabolism of bacterial cells, the effects of which could be observed in changes in the growth rate and the duration of lag phase for colonies treated with these silver nanostructures. The growth of bacterial colonies is typically modeled as a first-order reaction:

$$dN/dt = kN \quad (1)$$

where N is the number of bacteria at time t, and k is the first-order rate constant. As the optical density of bacteria is proportional to the concentration,[48] this equation can be rearranged to:

$$\ln(A/A_o) = kt \quad (2)$$

where A and A_0 are the absorbance at 600 nm of the bacterial solution at time t and zero, respectively. Thus, a linear regression of $\ln(A/A_0)$ versus t should yield a quantitative assessment of the growth rate constant k of the bacterial culture. Additionally, the lag phase (t_L), defined as the time between inoculation and initiation of the log phase, is a measure of the amount of work required for a bacterial colony to adapt to its environment and provides another perspective by which to view changes in growth kinetics.[53] This value is typically measured from growth curves as the point at which the slope of the exponential growth phase intersects a horizontal line drawn from the initial absorbance value of the colony. From the growth curves in **Figure 4**, the values of growth rate constants were then calculated by linear regression, and the lag-phase durations were measured for *E. coli* in solutions of the as-prepared

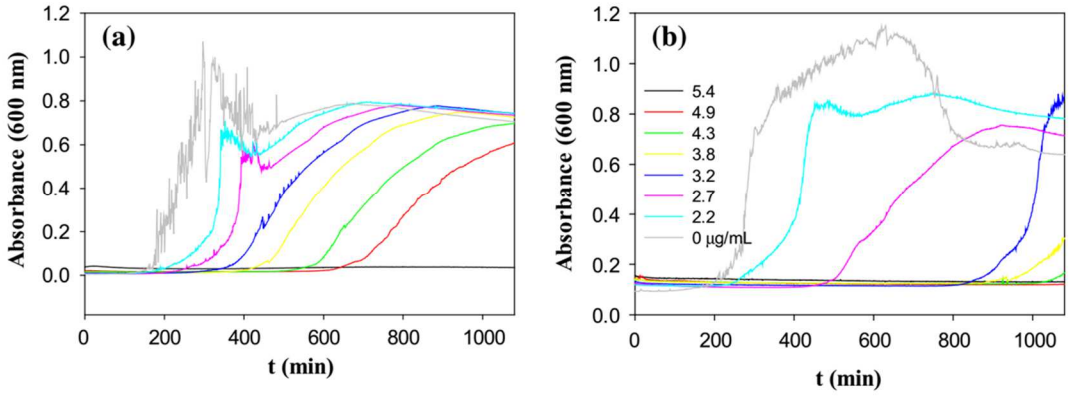

Fig. 4 Growth curves of *E. coli* cultures in Luria broth containing (a) silver seed nanoparticles and (b) faceted nanostructures formed by irradiation for 24 h. Nanoparticle concentrations are specified in figure legends.

seed nanoparticles and faceted silver nanostructures. The results are shown graphically in **Figure 5** (and summarized in **Table S1**). A clear difference can be

observed in the growth kinetics for *E. coli*, where faceted nanostructures (red bars) exhibited markedly enhanced activity in inhibiting bacterial growth than the as-prepared seed particles (black bars), with a lower growth rate constant (*k*) (i.e., slower growth) and longer lag-phase duration (t_L) at all particle concentrations, in good agreement with the MIC values estimated above. Notably, the difference in lag-phase duration is quite marked, with the silver seed nanoparticles having 2, 3, and 4 times shorter duration periods than the faceted nanostructures at 2.2, 2.7, and 3.2 μg/mL solution concentrations, respectively. At higher concentrations, this difference appears to decline going from less than three times the duration at 3.8 μg/mL to slightly above two times the duration at 4.3 μg/mL, indicating that a maximum difference in growth inhibition occurred at lower concentrations where mechanisms of toxicity are more resolved. This is further supported by values of the growth rate constant calculated at these concentrations, with the most dramatic difference between the two silver nanostructure samples occurring at 2.7 μg/mL where the *E. coli* cultures treated with silver seed nanoparticles exhibited a growth rate constant of 6.0×10^{-3} min^{-1}, almost twice as much as that of the faceted nanostructures (3.1×10^{-3} min^{-1}). Both solutions of silver nanostructures displayed a concentration at which they exerted their maximal effects on bacterial growth and lag-phase duration independently, with the growth rate being affected maximally at lower concentrations than lag-phase duration. This is expected as bacterial cells may withstand a certain degree of inhibition before having their growth drastically affected. Silver seed

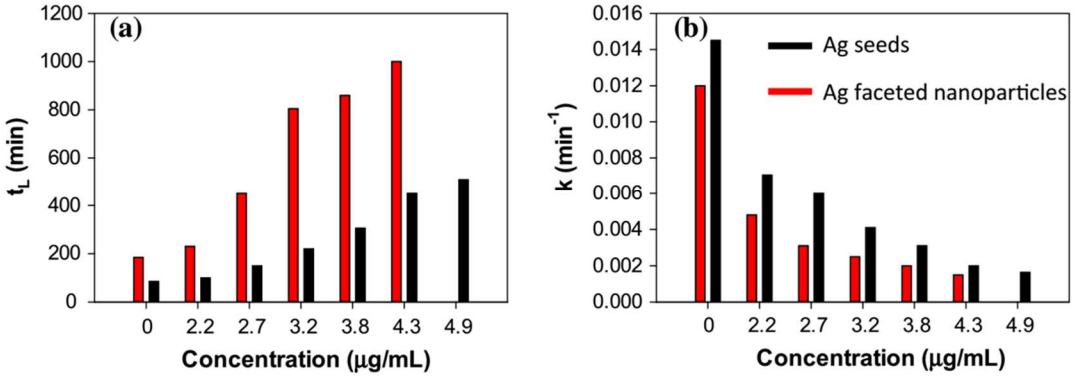

Figure 5. Bar charts summarizing (a) lag-phase durations (t_L) and (b) growth rate constants (k) calculated from the growth curves in **Figure 4** for the seed nanoparticles (black bars) and the irradiated nanostructures (red bars) at various concentrations.

nanoparticles demonstrated their maximum decline in growth rate between 2.7 and 3.2 µg/mL at which growth rate constants decreased from 6.0 x 10^{-3} to 4.1 x 10^{-3} min^{-1} and a maximum increase in lag-phase duration between 3.8 and 4.3 µg/mL at which lag-phase duration increased by 145 min (from 305 to 450 min). The changes of these critical growth parameters occurred at lower concentration for the faceted nanostructure solutions, with a maximum decline in growth rate occurring between 2.2 and 2.7 µg/mL where growth rate constant decreased from 4.8 x 10^{-3} to 3.1 x 10^{-3} min^{-1} and a maximum increase in lag-phase duration between 2.7 and 3.2 µg/mL at which lag-phase duration increased by almost 6 h (from 450 to 805 min), respectively. This difference in critical concentrations at which these growth parameters are maximally affected is likely due to the different mechanisms of inhibition acting on the bacterial cells. Because silver seed nanoparticles are smaller and more prone to oxidation, they would affect bacterial cells primarily by releasing

silver ions into and around the bacterial cells which will subsequently penetrate the outer-membrane and bind respiratory chain dehydrogenases embedded in the inner-membrane.[8, 54] This mechanism is supported by surface enhanced Raman spectroscopy (SERS) studies performed by Zeiri *et al.* which suggest that silver ions localize near flavin-containing cellular components, two of which are likely NADH:ubiquinone oxidoreductase and succinate dehydrogenase that contain flavin mononucleotide and flavin adenine dinucleotide, respectively.[55] This is particularly likely as both of these proteins contain a high density of sulfur-containing moieties such as structurally significant cysteine residues and a large number of iron-sulfur clusters involved in their redox processes.[56, 57] Binding of silver ions to these proteins likely causes a severe disruption of their function and eventually leads to a complete collapse of membrane-potential through leakage of protons and intracellular potassium ions.[58-60] In contrast, faceted silver nanostructures are much larger and, due to their highly (111) faceted surface structure, have an enhanced affinity for the oxygen-containing groups of the O-antigen domain of lipopolysaccharide molecules resulting in attractive forces which allow for rapid localization to gram-negative bacterial outer membranes. This is advantageous as these nanostructures will more likely have a significant fraction of their mass intact upon localizing to a bacterial cell resulting in a much larger silver ion reservoir at the site of activity. Upon localization, these structures could also exert additional structural damage by binding to OmpA and Lpp proteins which are major constituents of the outer-membrane and provide a physical linkage between the outermembrane and the peptidoglycan layer.[58, 61]

Because these proteins cover much of the surface, large silver nanostructures can bind to multiple units and cause severe perturbation of the outer-membrane structure resulting in pit formation and cell lysis.[54] Because these larger nanostructures can physically lyse bacterial cells as well, a lower concentration is required to cause severe inhibitory effects and is reflected in both the larger change in lag-phase duration, and lower MIC values. Both seed and faceted nanostructures have similar maximal decreases in growth rate constant, and this could be attributed to the role of the inhibitory actions of silver ions that dominate at lower concentrations as the probability of large silver nanostructures localizing to a significant population of bacterial cells is low. This supports the idea of faceted silver nanostructures having an enhanced inhibitory effect on bacterial growth via additional membrane disruption mechanisms, despite a marked increase in size, and warrants a closer investigation in future studies as to the exact processes responsible for this activity. From a more fundamental structural viewpoint however, (111) faceted silver nanostructures are known to be less favorably oxidized than other high-index facets as indicated by O_2 adsorption energies calculated by Wang *et al.* and more favorably dissolved in acidic environments as reported by *Lyu et al*.[62, 63] These oxidation and dissolution kinetics therefore predict (111) faceted silver nanostructures to be more efficient at Ag-delivery then those with different surface crystal structures. By avoiding oxidation

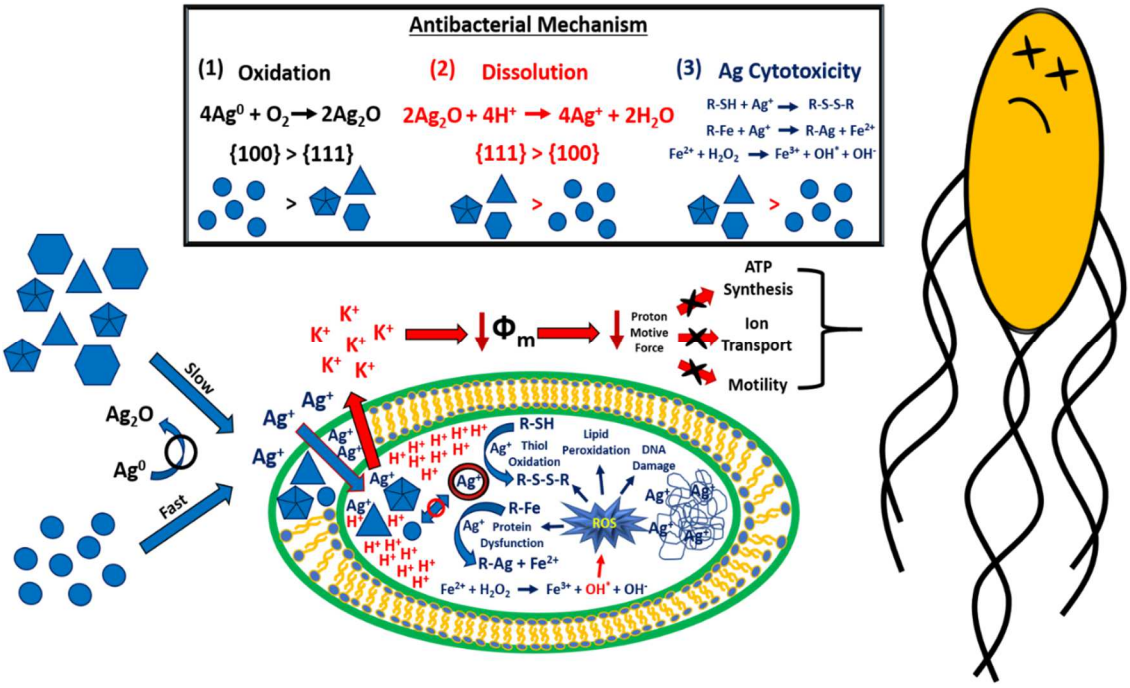

Figure 6. Proposed antibacterial mechanisms of spherical and {111} faceted silver nanostructures.

and maintaining most of its Ag content in the metallic state before entering a bacterial cell, then rapidly releasing cytotoxic Ag^+ ions in the acidic environment around cellular inner membranes, Ag-toxicity is maximized. This proposed mechanism of enhanced Ag^+ toxicity by (111) faceted structures is depicted in **Figure 6**, which emphasizes the Ag^+ release processes and subsequent Ag^+ toxicity mechanisms for these two structures. Comprehensive elucidation of these underlying mechanisms will require additional biological experiments such as transcriptomic analysis and thorough microscopic studies of silver nanostructure-treated bacterial cells in order to substantiate this model, and is the subject of future work.

1.5 Conclusion

A variety of faceted silver nanostructures, including triangular nanoprisms, nanodecahedra, and nanobipyramids were synthesized by irradiation of silver seed nanoparticles with blue LEDs and demonstrated enhanced antimicrobial activity when compared with smaller, spherical silver nanoparticles. TEM studies revealed that these nanostructures had predominantly (111) faceted surfaces which not only aided in binding to bacterial cell walls but also in the effective delivery of silver ions into bacterial cells. Growth kinetics measurements revealed that the faceted silver nanostructures demonstrated a lower MIC as well as lower concentrations at which growth rate constant and lag-phase duration were critically affected. This is postulated to be due to larger, (111) faceted silver nanostructures having favorable oxidation and dissolution kinetics, and causing additional physical disruption of bacterial cell walls through binding of outer-membrane proteins crucial for cell wall integrity in addition to the typical inhibitory mechanisms exhibited by ionic silver. These findings suggest that the antimicrobial activity of silver nanostructures is more structure-dependent than is generally accepted and provides a structural and biochemical basis for this. Further inquiry into the effects of (111) faceted silver nanostructures on the cellular components of bacterial cells will shed light on these mechanisms.

1.6 Acknowledgements

This work was supported in part by the National Science Foundation (CHE-1012258, CHE-1265635 and DMR-1409396). TEM work was carried out at the National Center for Electron Microscopy at the Lawrence Berkeley National Laboratory as part of a user project. The PXRD data in this work were recorded on a Rigaku SmartLab instrument supported by the NSF Major Research Instrumentation (MRI) Program under Grant DMR-1126845.

1.7 Supporting Information

Table S1. Summary of growth kinetic parameters obtained through analysis of growth curves in **Figure 5**.

	Ag Seed Nanoparticles		Ag Faceted Nanostructures	
C_{Ag} (μg/mL)	t_L (min)	k (min^{-1})	t_L (min)	k (min^{-1})
5.4	–	–	–	–
4.9	510	1.6×10^{-3}	–	–
4.3	450	2.0×10^{-3}	1000	1.5×10^{-3}
3.8	305	3.1×10^{-3}	860	2.0×10^{-3}
3.2	220	4.1×10^{-3}	805	2.5×10^{-3}
2.7	150	6.0×10^{-3}	450	3.1×10^{-3}
2.2	100	7.0×10^{-3}	230	4.8×10^{-3}
0	85	1.5×10^{-2}	185	1.2×10^{-2}

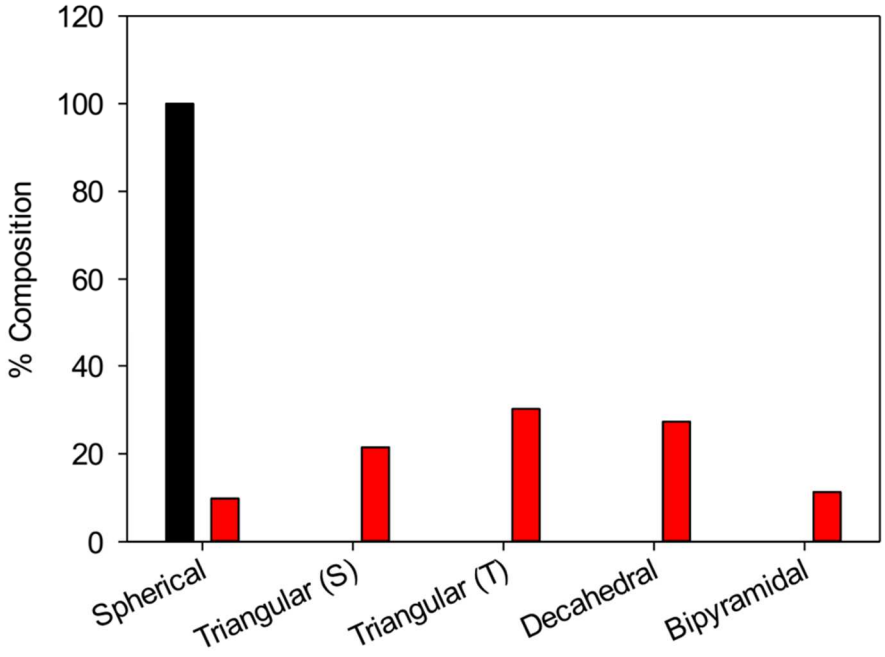

Figure S1. Shape distribution of faceted silver nanostructures prepared by irradiation (red bars) and Ag seed nanoparticles (black bars). Data are obtained from STEM measurements in **Figure 1**.

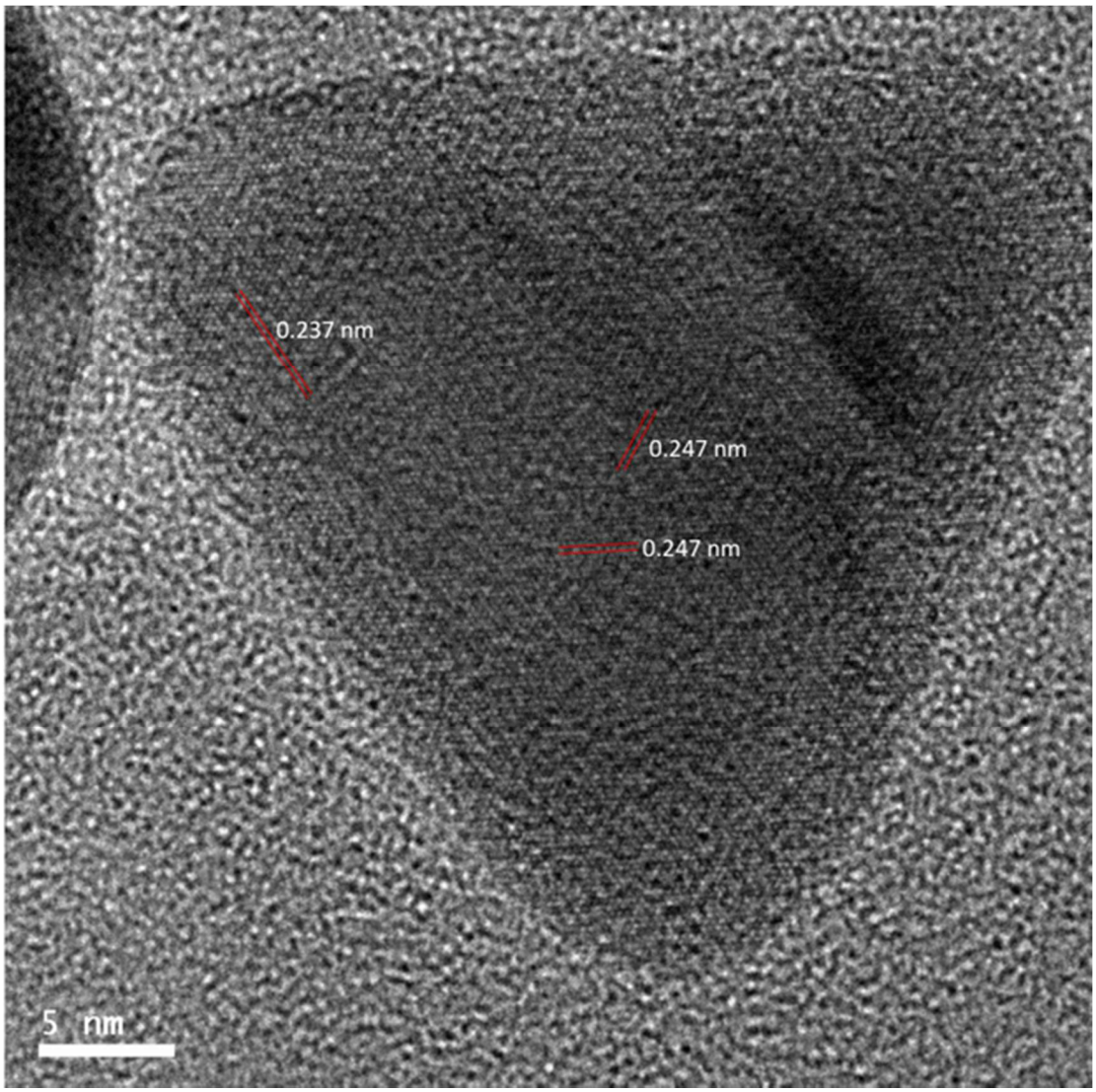

Figure S2. High-resolution TEM image of a triangular silver nanoprism with measured lattice spacings. This image is a zoom in of the inset in **Figure 1b**.

1.8 References

(1) Alexander, J. W. *Surgical Infections* **2009**, *10* (3), 289–292.

(2) Russell, A.; Hugo, W. *Progress in Medicinal Chemistry* **1994**, 351–370.

(3) Maillard, J. Y.; Hartemann, P. *Crit Rev Microbiol* **2013**, 39 (4), 373–383.

(4) Marambio-Jones, C.; Hoek, E. M. V. *J Nanopart Res* **2010**, 12 (5), 1531–1551.

(5) Kim, J. S.; Kuk, E.; Yu, K. N.; Kim, J.-H.; Park, S. J.; Lee, H. J.; Kim, S. H.; Park, Y. K.; Park, Y. H.; Hwang, C.-Y.; Kim, Y.-K.; Lee, Y.-S.; Jeong, D. H.; Cho, M.-H. *Nanomedicine: Nanotechnology, Biology and Medicine* **2007**, *3* (1), 95–101.

(6) Xu, F. F.; Imlay, J. A. *Applied and Environmental Microbiology* **2012**, 78 (10), 3614–3621.

(7) Liau, S.; Read, D.; Pugh, W.; Furr, J.; Russell, A. *Letters in Applied Microbiology* **1997**, *25* (4), 279–283.

(8) Holt, K. B.; Bard, A. J. *Biochemistry* **2005**, *44* (39), 13214–13223.

(9) Petering, H. G. *Pharmacology & Therapeutics. Part A: Chemotherapy, Toxicology and Metabolic Inhibitors* **1976**, 1 (2), 127–130.

(10) Schreurs W. J.; Rosenberg, H. *Journal of Bacteriology* **1982**, 152 (1), 7–13.

(11) Yamane, T.; Davidson, N. *Biochimica et Biophysica Acta* **1962**, *55* (5), 609–621.

(12) Kvítek, L.; Panáček, A.; Soukupová, J.; Kolář, M.; Večeřová, R.; Prucek, R.; Holecová, M.; Zbořil, R. *The Journal of Physical Chemistry C* **2008**, 112 (15), 5825–5834.

(13) Raffi, M.; Hussain, F.; Bhatti, T. M.; Akhter, J. I.; Hameed, A.; Hasan, M. M. *J Mater Sci Technol* **2008**, 24 (2), 192–196.

(14) Smetana, A. B.; Klabunde, K. J.; Marchin, G. R.; Sorensen, C. M. *Langmuir* **2008**, 24 (14), 7457–7464.

(15) Vertelov, G. K.; Krutyakov, Y. A.; Efremenkova, O. V.; Olenin, A. Y.; Lisichkin, G. V. *Nanotechnology* **2008**, 19 (35), 355707.

(16) Porel, S.; Ramakrishna, D.; Hariprasad, E.; Gupta, A. D.; Radhakrishnan, T. P. *Current Science India* **2011**, 101 (7), 927–934.

(17) Jones, S. A.; Bowler, P. G.; Walker, M.; Parsons, D. *Wound Repair and Regeneration* **2004**, 12 (3), 288–294.

(18) Leaper, D. J. *International Wound Journal* **2006**, 3 (4), 282–294.

(19) Morones, J. R.; Elechiguerra, J. L.; Camacho, A.; Holt, K.; Kouri, J. B.; Ramírez, J. T.; Yacaman, M. J. *Nanotechnology* **2005**, *16* (10), 2346–2353.

(20) Pal, S.; Tak, Y. K.; Song, J. M. *Applied and Environmental Microbiology* **2007**, *73* (6), 1712–1720.

(21) Horswell, S. L.; Pinheiro, A. L. N.; Savinova, E. R.; Danckwerts, M.; Pettinger, B.; Zei, M.-S.; Ertl, G. *Langmuir* **2004**, 20 (25), 10970–10981.

(22) Jin, R. *Science* **2001**, 294 (5548), 1901–1903.

(23) Thrall, E. S.; Steinberg, A. P.; Wu, X.; Brus, L. E. *The Journal of Physical Chemistry C* **2013**, 117 (49), 26238–26247.

(24) Xue, C.; Métraux Gabriella S.; Millstone, J. E.; Mirkin, C. A. *Journal of the American Chemical Society* **2008**, 130 (26), 8337–8344.

(25) Lu, H.; Zhang, H.; Yu, X.; Zeng, S.; Yong, K.-T.; Ho, H.-P. *Plasmonics* **2011**, 7 (1), 167–173.

(26) Pastoriza-Santos, I.; Liz-Marzán, L. M. *Journal of Materials Chemistry* **2008**, 18 (15), 1724.

(27 Jin, R.; Cao, Y. C.; Hao, E.; Métraux, G. S.; Schatz, G. C.; Mirkin, C. A. *Nature* **2003**, 425 (6957), 487–490.

(28) Millstone, J. E.; Hurst, S. J.; Métraux, G. S.; Cutler, J. I.; Mirkin, C. A. *Small* **2009**, 5 (6), 646–664.

(29) Callegari, A.; Tonti, D.; Chergui, M. *Nano Letters* **2003**, 3 (11), 1565–1568.

(30 Bastys, V.; Pastoriza-Santos, I.; Rodríguez-González, B.; Vaisnoras, R.; Liz-Marzán, L. M. *Advanced Functional Materials* **2006**, 16 (6), 766–773.

(31) Khan, M. A. M.; Kumar, S.; Ahamed, M.; Alrokayan, S. A.; Alsalhi, M. *Nanoscale Research Letters* **2011**, 6 (1), 434.

(32) Liu, T.; Li, D.; Yang, D.; Jiang, M. *Chemical Communications* **2011**, 47 (18), 5169.

(33) Mceachran, M.; Kitaev, V. Chemical Communications **2008**, 0, 5737.

(34) Gao, Y.; Jiang, P.; Song, L.; Wang, J.; Liu, L.; Liu, D.; Xiang, Y.; Zhang, Z.; Zhao, X.; Dou, X.; Luo, S.; Zhou, W.; Xie, S. *Journal of Crystal Growth* **2006**, 289 (1), 376–380.

(35) Zhang, J.; Li, S.; Wu, J.; Schatz, G. C.; Mirkin, C. A. *Angewandte Chemie International Edition* **2009**, 48 (42), 7787–7791.

(36) Wiley, B. J.; Xiong, Y.; Li, Z.-Y.; Yin, Y.; Xia, Y. *Nano Letters* **2006**, 6 (4), 765–768.

(37) Pietrobon, B.; Kitaev, V. *Chemistry of Materials* **2008**, 20 (16), 5186–5190.

(38) Zheng, X.; Zhao, X.; Guo, D.; Tang, B.; Xu, S.; Zhao, B.; Xu, W.; Lombardi, J. R. *Langmuir* **2009**, 25 (6), 3802–3807.

(39) Rocha, T. C. B. A. C. R.; Zanchet, D. *The Journal of Physical Chemistry C* **2007**, 111 (19), 6989–6993.

(40) Zhou, J.; An, J.; Tang, B.; Xu, S.; Cao, Y.; Zhao, B.; Xu, W.; Chang, J.; Lombardi, J. R. *Langmuir* **2008**, 24 (18), 10407–10413.

(41) Germain, V.; Li, J.; Ingert, D.; Wang, Z. L.; Pileni, M. P. *The Journal of Physical Chemistry B* **2003**, 107 (34), 8717–8720.

(42) Aherne, D.; Ledwith, D. M.; Gara, M.; Kelly, J. M. *Advanced Functional Materials* **2008**, 18 (14), 2005–2016.

(43) Creighton, J. A.; Eadon, D. G. *J. Chem. Soc., Faraday Trans*. **1991**, 87 (24), 3881–3891.

(44) Kelly, K. L.; Coronado, E.; Zhao, L. L.; Schatz, G. C. *The Journal of Physical Chemistry B* **2003**, 107 (3), 668–677.

(45) Xu, S.; Tang, B.; Zheng, X.; Zhou, J.; An, J.; Ning, X.; Xu, W. *Nanotechnology* **2009**, 20 (41), 415601.

(46) Gutierrez, M.; Henglein, A. *The Journal of Physical Chemistry* **1993**, 97 (44), 11368–11370.

(47) Jiang, Z.-J.; Liu, C.-Y.; Li, Y.-J. *Chemistry Letters* **2004**, 33 (5), 498–499.

(48) Sezonov, G.; Joseleau-Petit, D.; Dari, R. *Journal of Bacteriology* **2007**, 189 (23), 8746–8749.

(49) Agnihotri, S.; Mukherji, S.; Mukherji, S. *RSC Adv*. **2014**, 4 (8), 3974–3983.

(50) Feng, Q. L.; Wu, J.; Chen, G. Q.; Cui, F. Z.; Kim, T. N.; Kim, J. O. *Journal of Biomedical Materials Research* **2000**, 52 (4), 662–668.

(51) Rietschel, E. T.; Kirikae, T.; Schade, F. U.; Mamat, U.; Schmidt, G.; Loppnow, H.; Ulmer, A. J.; Zahringer, U.; Seydel, U; Di Padova, F. *The FASEB Journal* **1994**, 8 (2), 217–225.

(52) Park, H.-J.; Kim, J. Y.; Kim, J.; Lee, J.-H.; Hahn, J.-S.; Gu, M. B.; Yoon, J. *Water Research* **2009**, 43 (4), 1027–1032.

(53) Robinson, T. *International Journal of Food Microbiology* **1998**, 44 (1-2), 83–92.

(54) Li, W.-R.; Xie, X.-B.; Shi, Q.-S.; Zeng, H.-Y.; Ou-Yang, Y.-S.; Chen, Y.-B. *Applied Microbiology and Biotechnology* **2009**, 85 (4), 1115–1122.

(55) Zeiri, L.; Bronk, B. V.; Shabtai, Y.; Eichler, J.; Efrima, S. *Applied Spectroscopy* **2004**, 58 (1), 33–40.

(56) Friedrich, T. *Biochimica et Biophysica Acta (BBA) - Bioenergetics* **1998**, 1364 (2), 134–146.

(57) Cecchini, G.; Schröder, I.; Gunsalus, R. P.; Maklashina, E. *Biochimica et Biophysica Acta (BBA) - Bioenergetics* **2002**, 1553 (1-2), 140–157.

(58) Koebnik, R.; Locher, K. P.; Gelder, P. V. *Molecular Microbiology* **2000**, 37 (2), 239–253.

(59) Lok, C.-N.; Ho, C.-M.; Chen, R.; He, Q.-Y.; Yu, W.-Y.; Sun, H.; Tam, P. K.-H.; Chiu, J.-F.; Che, C.-M. *Journal of Proteome Research* **2006**, 5 (4), 916–924.

(60) Letellier, L.; Shechter, E. *European Journal of Biochemistry* **1979**, 102 (2), 441–

447.

(61) Sonntag, I.; Schwarz, H.; Hirota, Y.; Henning, U. *Journal of Bacteriology* **1978**, 136(1):280–285.

(62) Wang, Q.; Cui, X.; Guan, W.; Zhang, L.; Fan, X.; Shi, Z.; Zheng, W. *Journal of Power Sources* **2014**, 269, 152–157.

(63) Lyu, L.-M.; Huang, M. H. *The Journal of Physical Chemistry C* **2011**, 115 (36), 17768–17773.

CHAPTER 2: Antibacterial Activity of AgCu Alloy Nanoparticles

2.1 Abstract

Silver-copper alloy nanoparticles of varying composition were synthesized using a facile wet chemical method, and characterized by high-resolution transmission electron microscopy (HRTEM), ultra-violet visible absorption spectroscopy (UV-vis), X-ray photoelectron spectroscopy (XPS), and cyclic voltammetry (CV). Transmission electron micrographs revealed average nanoparticle diameters of 3.45 ± 0.99, 9.29 ± 2.24, 12.85 ± 9.75 nm, 13.10 ± 9.49 nm, 6.74 ± 4.81 nm, 5.37 ± 3.58 nm, and 4.52 ± 3.67 nm for Cu, Ag, $AgCu_3$, $AgCu_2$, AgCu, Ag_2Cu, Ag_3Cu alloy nanoparticles respectively. XPS measurements determined the composition of these alloy nanoparticles to be 86% (Ag_3Cu), 82% (Ag_2Cu), 47% (AgCu), 56% ($AgCu_2$), 56% ($AgCu_3$) silver by mass, which was generally dependent on the initial feeding ratio. Cyclic voltammetry measurements indicated the presence of both silver and copper surfaces on alloy particle surfaces, with the ratio also generally dependent on the initial feeding ratio. Silver-copper alloy nanoparticle solutions were found to be highly active in the inhibition of bacterial growth, with AgCu alloy nanoparticles demonstrating the most effective inhibition of *Escherichia coli* in liquid media. Fluorescence microscopy utilizing the reactive oxygen species (ROS) indicator CellROX demonstrated a marked increase in fluorescence upon addition of nanoparticles solutions, with the fastest increases observed for Cu, then AgCu alloy nanoparticles. This correlated with electron paramagnetic resonance

(EPR) results which showed a similar trend with hydroxyl radical formation in the presence of hydrogen peroxide. As AgCu alloy nanoparticles were similar in size as Ag nanoparticles, this enhanced generation of ROS inside cells is proposed to be due to Fenton reactions catalyzed by copper species. Spectrokinetic studies reveal the AgCu alloy nanoparticles are relatively stable towards oxidation, suggesting that their superior antibacterial activity observed can be attributed to the stabilization of copper atoms due to a homogeneous alloy structure. These results demonstrate the efficacy of silver-copper alloy nanoparticles for antibacterial applications, and provide for the first time, a thorough analysis of their mechanisms of action.

2.2 Introduction

Multi-drug resistant strains of pathogenic bacteria are becoming increasingly prevalent due to the misuse of traditional antibiotics, resulting in widespread infection in communities around the world. In order to address this increasingly serious global health issue, highly-effective antibacterial agents must be developed. Materials comprised of silver and copper have proven to be the leading candidates for this application as they exhibit broad-spectrum antimicrobial activity against a variety of microorganisms.[1,2] This affords the biggest advantage over conventional antibiotics, which are typically highly target-specific and therefore allow bacteria to easily evolve resistance mechanisms. Due to the unique reactivity of Ag and Cu, they can undergo reactions with a variety of biomolecules resulting in broad spectrum cytotoxicity. According to Pearson's definition, Ag^{+} and Cu^{+} ions are soft acids (Cu^{2+} is

borderline) and react readily with soft bases such as sulfur and phosphorous containing molecules.[3] Consequently, these metals can react with the thiol moieties of cysteine residues common to many proteins, resulting in oxidation and subsequent disulfide bond formation by the following mechanisms:

$$2Ag^{+} + 2RSH \rightarrow 2Ag^{0} + RSSR + 2H^{+} \quad (1)$$

$$2Cu^{+} + 2RSH \rightarrow 2Cu^{0} + RSSR + 2H^{+} \quad (2)$$

causing misfolding and alteration of enzymatic active sites, both of which result in protein dysfunction. Silver has a larger propensity for undergoing this type of reaction due to the larger magnitude of its single electron reduction potential (+0.799 V Ag^{+}/Ag) compared with that of copper (+0.521 V Cu^{+}/Cu) and should therefore exhibit superior cytotoxicity via this mechanism. Copper however, is also stable in the Cu^{2+} oxidation state which allows for two additional oxidation reactions to occur:

$$Cu^{2+} + 2RSH \rightarrow Cu^{0} + RSSR + 2H^{+} \quad (3)$$

$$2Cu^{2+} + 2RSH \rightarrow 2Cu^{+} + RSSR + 2H^{+} \quad (4)$$

where the one-electron reduction given by reaction (3) (+0.342 V Cu^{2+}/Cu) is more favorable than the two-electron reduction given by reaction (4) (+0.153 V Cu^{2+}/Cu^{+}) suggesting that copper may be more active in inhibiting cellular growth through this mechanism.[4] Aside from structural distortion, binding of these metals to $[Fe_4\text{-}S_4]^{2+}$ clusters, a common motif in protein structure, causes displacement of Fe atoms and subsequently converts a protein into its inactive form.[5] Many of these iron-sulfur

cluster-containing proteins are critical to metabolic and biosynthetic pathways, such as Complex I and II of the electron transport chain or dihydroxy-acid dehydratase which is responsible for branched-chain amino acid synthesis, and depend on these clusters for proper function, therefore disruption of these moieties leads to metabolic collapse which has been found to be one of the primary mechanisms of soft metal toxicity.[6-9] Binding of these iron-sulfur clusters not only disrupts enzymatic activity, but also releases Fe(II) which triggers an additional mechanism of cytotoxicity, oxidative stress via Fenton chemistry. As was suggested by Haber and Weiss, iron can catalyze the reduction of hydrogen peroxide into highly reactive hydroxyl radicals:

$$Fe^{2+} + H_2O_2 \rightarrow Fe^{3+} + OH^- + OH^{\cdot} \quad (5)$$

which can subsequently form additional reactive oxygen species (ROS) via the Haber-Weiss cycle:

$$H_2O_2 + OH^{\cdot} \rightarrow H_2O + O_2^{-\bullet} + H^+ \quad (6)$$

$$H_2O_2 + O_2^{-\bullet} \rightarrow O_2 + OH^- + OH^{\cdot} \quad (7)$$

with the production of hydroxyl radicals ($OH^{\cdot}$) and superoxide ($O_2^{-\bullet}$) anions causing cellular toxicity via lipid peroxidation, reduction of catalytically active metal centers, oxidation of amino acid residues, and oxidation of DNA base-pairs as well as their sugar-phosphate backbone resulting in single and double-stranded breaks.[10-13] Silver ions however, do not undergo Fenton reactions readily at the intracellular pH of 7.6 experimentally determined for *E. coli* due to the relatively high redox potentials of the

Ag/Ag^+ (+0.351 V) and Ag^+/Ag^{2+} (+1.53 V) species compared with the $H_2O_2/ OH^·$ (+0.292 V) redox couple.[14-16] The thermodynamics of this process is governed by the standard potential of the general redox reaction:

$$M^{n+} + H_2O_2 \rightarrow M^{(n+1)+} + OH^- + OH^· \quad (8)$$

which is defined as E_8, and given by the sum of the two half reactions:

$$M^{(n+1)+} + e^- \rightarrow M^{n+} \quad (9)$$

$$H_2O_2 + e^- \rightarrow OH^- + OH^· \quad (10)$$

where E_{10} and E_9 correspond to the reduction potentials of equation 10 and 9 respectively, yielding an overall expression of:

$$E_8 = E_{10} - E_9 \quad (11)$$

for the standard potential of the Fenton reaction catalyzed by metal ions. Since E_{10} = +0.279 V at intracellular pH, only metal ions with reduction potentials less positive than +0.279 V under these conditions will yield appreciable reaction rates as governed by the relationship between free energy and reaction potential, $\Delta G = -nFE_8$. Conversely, copper ions have much more favorable reduction potentials at intracellular pH for both $Cu^{2+/}Cu^+$ (+0.295 V) and Cu^{2+}/Cu^0 (+0.073 V) which are known to undergo Fenton reactions, primarily through the $Cu^{2+/}Cu^+$ species:

$$Cu^+ + H_2O_2 \rightarrow Cu^{2+} + OH^- + OH^· \quad (12)$$

$$Cu^{2+} + O^{2-•} \rightarrow Cu^+ + O_2 \quad (13)$$

$$2Cu^+ + 2H^+ + O_2 \rightarrow 2Cu^{2+} + H_2O_2 \quad (14)$$

which further propagates the chain of reactive oxygen species.[12,17] As oxidative stress is extremely detrimental to cellular functions, it is no coincidence that both silver and

copper ions have been found to effectively inhibit bacterial growth through these mechanisms.[18,19] Synergistic effects of oxidative stress and protein dysfunction are therefore expected, and have been observed experimentally by Djoko *et al.* in their study of copper-mediated inhibition of the heme biosynthetic pathway (HemN/KatC) of the *N. gonorrhoeae* bacterium.[20] This has a marked effect on cellular biochemistry as this pathway allows for the synthesis of heme subunits which are necessary for the activity of a wide range of enzymes, the most relevant of which in this case is catalase, the enzyme responsible for decomposing hydrogen peroxide into water and molecular oxygen thereby providing protection against oxidative stress.[20,21] By acting to both inhibit protein function globally and cause oxidative stress through generation of ROS indirectly through Fe(II) release and directly via Fenton chemistry in the case of copper, these two metals demonstrate remarkable potential as broad-spectrum antimicrobial agents. Therefore, the realization of materials which can effectively deliver these ions into pathogenic microorganisms will be essential for combating the growing antibiotic resistance crisis.

Silver and copper nanomaterials have been extensively studied for this application as they provide a stable Ag^{+} and Cu^{2+} reservoir which can release these cytotoxic ions in close proximity to bacterial cells thereby increasing local concentrations dramatically. Additionally, silver and copper nanostructures have demonstrated enhanced antimicrobial activity over simple ionic solutions which can be attributed to several factors: (1) targeted ion release as nanoparticles in solution can enter into bacterial cells before a significant fraction of their mass is dissolved,

thereby delivering most of their cytotoxic metal directly inside cells. (2) exceptionally large surface area which increases the probability of interaction with bacterial cell surfaces and also increases nanoparticle dissolution rate which can result in extreme local metal concentrations at the site of the particle (3) physical membrane disruption as nanoparticles passing into cells will become localized in plasma membranes which will distort long-range lipid and intermembrane protein structure, resulting in the formation of membrane "pits" which subsequently cause leakage of cellular components. Due to these additional cytotoxic mechanisms, there have been extensive studies demonstrating the effectiveness of both silver and copper nanoparticles as antimicrobial agents.[22-26] Copper oxide nanoparticles have also gained considerable attention as an antimicrobial agent as it is a simple, more cost efficient material to synthesize, and has been found to be an equally, if not, more effective bactericidal agent than silver nanoparticles.[27-29] Although copper oxide nanoparticles have been found to be effective, metallic copper nanoparticles have been shown to have even greater activity and thus offer the greatest potential for antimicrobial applications.[27] However, copper nanomaterials have one critical disadvantage which is their tendency to oxidize under ambient conditions. Oxidation occurs first at the surface of the nanoparticles, then the oxide layer progressively grows inward toward the copper core as oxygen diffuses through the oxide layer and eventually oxidizes the entire particle into CuO and Cu_2O.[30] Efforts to maintain copper nanostructures in the metallic state typically involve encapsulation in a polymer matrix which although effective in suppressing oxidation, prevents the

nanoparticles from entering cells, thereby nullifying the primary mechanisms of action that affords nanomaterials their biggest advantages.[31,32] A more effective strategy to stabilizing metallic copper nanomaterials is through alloying with more noble metals such as silver or gold. For example, Besner *et al.* reported an increased stability of Ag atoms within a Ag/Au alloy as manifested through a decreased dissolution rate of silver atoms from the nanostructure in the presence of ROS at gold mole fractions above 0.4.[33] This alloying affect is due to the charge-transfer from atoms of a less noble metal to a more noble one, thereby shifting the redox potentials of both atoms to an intermediate value. Although this effect is utilized frequently in the field of catalysis, there has not been a significant application towards antimicrobial materials, particularly copper, as is the case in this study.

In this investigation, we report the enhanced antibacterial activity of silver-copper alloy nanoparticles. A facile, wet-chemical reduction route was utilized to synthesize AgCu alloy nanoparticles of varying composition with the goal being to find the optimal alloy structure for inhibiting the growth of Escherichia coli cultures. cyclic voltammetry (CV) and x-ray photoemission spectroscopy (XPS) are used to determine the surface structure and composition of these alloy nanoparticles respectively, and time-resolved UV-vis spectroscopy is utilized to quantify their oxidation kinetics. These characterizations are then correlated to the observed antimicrobial activity and fluorescence microscopy images of *E. coli* cells incubated with the cellular reactive oxygen species indicator CellROX Green, in the presence of Ag,Cu, and AgCu alloy nanoparticle solutions. The observed changes in cellular

fluorescence are further investigated using electron paramagnetic resonance (EPR) studies, which quantify the *in-vitro* hydroxyl radical generation of these structures, giving a complete ROS generation profile for each. AgCu alloy nanoparticles synthesized with an initial Ag:Cu feeding ratio of 1:1 were concluded to yield the most effective nanostructures for inhibiting the growth of *E. coli* cells, with its activity attributed to optimal synergistic toxic effects of Ag and Cu, primarily due to enhanced oxidative stress caused by Cu-catalyzed Fenton chemistry. These results demonstrate the efficacy of bimetallic, silver-copper alloy nanoparticles for antimicrobial applications, and provide direct evidence for the predominant mechanisms of cytotoxicity Ag and Cu afford.

2.3 Experimental

2.3.1 Materials

Silver nitrate (99.9% STREM Chemicals), sodium citrate dihydrate (Fisher), sodium borohydride powder (98+% ACROS), copper acetate monohydrate (98+% Alfa Aesar), 1-hexanethiol (96% ACROS Organics), and Miller Luria broth (Fisher) were used as received. All solvents were obtained from typical commercial sources and used without further treatment. Water was supplied by a Barnstead Nanopure water system (18.3 MΩ•cm).

2.3.2 Synthesis of AgCu Alloy Nanoparticles

Silver-copper alloy nanoparticles were synthesized via a simple co-reduction of silver and copper salts in aqueous solution. In short, a 250 mL three-neck flask was first cleaned with *aqua regia*, then rinsed with excessive nanopure water to remove any remaining ions. Then, 96.5 mL of nanopure water and a total volume of 500 μL of 20 mM $AgNO_3$ and $Cu(OAc)_2$ solutions were added at varying Ag:Cu ratios (1:0, 3:1, 2:1, 1:1, 1:2, 1:3, 0:1). To this solution, 2 mL of a 50 mM tri-sodium citrate solution was added and the entire solution was stirred at 1000 rpm for 20 min with nitrogen purging. The flask was then placed in an ice bath and allowed to cool for 10 min with continued purging. Upon completion of this cooling period, 1 mL of an ice-cold, freshly-prepared, 50 mM $NaBH_4$ solution was rapidly injected into the flask. An immediate color change was observed ranging from faint yellow at high silver ratios to light amber with increasing copper ratio indicating the reduction of the metal salts into Ag/Cu alloy nanoparticles. This solution was then allowed to stir for an additional 15 minutes in the ice-bath under nitrogen to allow for complete reduction.

2.3.3 Hexanethiol Ligand-Exchange

A ligand-exchange reaction was utilized to protect the alloy nanoparticles from oxidation and maintain their initial composition for elemental analysis. This was performed by the addition of 4.3 μL of 1-hexanethiol in 20 mL of toluene into freshly synthesized silver-copper alloy nanoparticle solutions under vigorous stirring. In minutes, the aqueous nanoparticle solution became clear and the toluene phase turned

a dark red color, indicating the successful functionalization of the nanoparticles with 1-hexanethiol. The aqueous phase was then discarded, and the toluene phase was washed several times by centrifugation in methanol to eliminate any free thiol ligands and excess metal salts. These purified alkanethiol-protected nanoparticle solutions were then dried on silicone substrates for elemental analysis, and dropcast on electrode surfaces for electrochemical measurements.

2.3.4 Oxidation Effects on Optical Properties

A quartz micro-cuvette with a maximum volume of 700 μL was filled with each AgCu alloy nanoparticle solution and UV-vis spectra taken after successive inversions of the cuvette during which an air bubble would pass through the entire volume, causing oxidation of the nanoparticles in solution. These oxidation steps were repeated until no significant change was observed in the spectra.

2.3.5 Electrochemistry

Electrochemical measurements were carried out using a standard three-electrode cell connected to a Pine electrochemical workstation, with a platinum foil and Ag/AgCl (3M KCl) utilized as the counter and reference electrode respectively. To prepare the working electrode, 1-hexanethiol-functionalized nanoparticle solutions were first dropcast onto a polished glassy carbon electrode and allowed to dry in air. Then, 10 μL of a 20% v/v NAFION solution dissolved in ethanol was added onto the electrode and allowed to dry in air. Cyclic voltammetry measurements were performed in an aqueous 0.1 M NaOH solution at room temperature, with several

cycles across the working potential range first being run in order to desorb surface-bound hexanethiol ligands and stabilize the nanoparticle surfaces.

2.3.6 Characterization Methods

The size and morphology of the AgCu alloy nanoparticles were characterized by high resolution transmission electron microscopy (HRTEM) on a Phillips CM300 operating at 300 kV. Samples were prepared by immersing the TEM grid into AgCu nanoparticle solutions immediately after opening the flask to air, adding an additional drop onto the grid, and rapidly drying it in a vacuum chamber. At least 150 particles were counted on each grid to create an appropriate size histogram. UV-visible (UV-vis) spectra of the AgCu alloy nanoparticles were taken immediately after opening reaction flasks to air using an Agilent Cary 60 UV-vis spectrometer with a 1 cm quartz cuvette. X-ray photoemission spectra (XPS) were acquired with a PHI 5400/XPS instrument equipped with an Al Kα source operated at 350 W and 10^{-9} Torr.

2.3.7 Antimicrobial Assays

Escherichia coli (ATCC 25922) cells were obtained by first spreading frozen liquid cultures (20% glycerol, -72 °C) on Luria broth (LB) agar plates and incubating them at 37 °C overnight. From these plates, one individual colony was selected and used to inoculate 3 mL of sterile liquid LB and incubated at 37 °C for 18 h with constant shaking at 250 rpm. Upon completion of this growth period, a 1 mL aliquot of this culture was removed and centrifuged at 5000 rpm for 5 min. The supernatant

was discarded, and the pellet re-suspend 1 mL sterile nanopure water. This process was repeated once, and enough of the second re-suspension was added to 5 mL of sterile nanopure water to bring the optical density (O.D.) at 600 nm to 0.100. This process was repeated once, with enough of the second re-suspension added to 5 mL of sterile water to bring the optical density at 600 nm to 0.100. This new suspension at 0.100 optical density was subsequently used for all inoculations. A 96-well plate was utilized to obtain bacterial growth profiles, with each well having 20 µL of this bacterial inoculation suspension, 20 µL fresh LB, varying volumes (2-100 µL) of nanoparticle solutions, and enough nanopure water to bring the final volume to 200 µL. Silver-copper alloy nanoparticle solutions were added last to all wells, then the 96-well plate was immediately placed into a Molecular Devices VERSAmax microplate reader which was maintained at a constant temperature of 37 °C with measurements of each well's optical density at 600 nm taken every minute over a 24 h period with a 15 s mixing period between each acquisition. To obtain the minimum bactericidal concentration (M.B.C.), a 48-prong stamp was first sterilized, then inserted into each half of the 96 well plate separately to immobilize bacterial cells onto each prong. These prongs were pressed into a fresh LB agar petri dish, and incubated at 37°C for 24 hr. The concentrations at which no bacterial growth was observed on the agar plate after the incubation period was determined to be the M.B.C. for that nanoparticle solution.

2.3.8 Fluorescence Microscopy

Escherichia coli suspensions used for imaging were produced by washing overnight liquid cultures with nanopure water as described above, but excluding the final dilution to 0.100 optical density. The washed *E. coli* suspension was then incubated with 5 μM CellROX for 30 minutes in the dark, then a 2 μL drop of this suspension was placed onto a 1.5 microscope cover slip (0.17 mm thickness) and used for fluorescence imaging. Images were acquired on a Solamere Spinning disk confocal microscope equipped with a Nikon TE2000 inverted stand, a CSU-X1 spinning disk, and a Hamamatsu ImageEMX2 camera. A 488 nm laser with a 500-550 nm band-pass emission was utilized as the excitation source, and a 60x 1.4 NA Nikon Plan Apo was utilized as the objective lens. *E.coli* suspensions were imaged at 1 frame per second for a total of 12 minutes with a 100 ms exposure time. After a given time period, a 2 μL aliquot of nanoparticle solution was added to the 2 μL drop of the *E. coli* suspension being imaged, and the increase in CellROX fluorescence was observed over the remaining time.

2.3.9 Electron Paramagnetic Resonance

All EPR measurements were taken at room temperature using a Bruker EMX EPR spectrometer operating at an X-band frequency of approximately 9.4 GHz, and using a Bruker ER 4122SHQE resonator. The spin trap used in all experiments was α-(4-Pyridyl N-oxide)-N-tert-butylnitrone (4-POBN). Solutions consisting of 50 mM 4-POBN, 20 mM phosphate buffer (pH=2), 100 mM hydrogen peroxide, and 100 uM nanoparticles or metal salts. Once the nanoparticle solutions were added to the sample

mixture, it was quickly mixed by pipetting and a 50 uL aliquot was loaded into a capillary tube. This capillary tube was then inserted into a quartz EPR tube (Wilmad) with a 4 mm outer diameter, and loaded into the EPR cavity resonator. All samples were analyzed two minutes after reagents were mixed and signal averaged over eight scans. Spectra were recorded using a microwave power of 20.17 mW, a modulation amplitude of 1 Gauss, a modulation frequency of 100 kHz, a spectral window of 100 G, and a resolution of 1024 points.

2.4 Results/Discussion

2.4.1 Characterization of AgCu Alloy Nanoparticles

The size and morphology of Ag, Cu, and AgCu alloy nanoparticles were characterized via HRTEM with representative electron micrographs shown in **Figure 1 and S1**. At all Ag and Cu feeding ratios, quasi-spherical particles of varying size can be observed with the smallest and most monodispersed (**Figure 1 and S2**) nanoparticles observed in copper nanoparticle micrographs which exhibited an average diameter of 3.47 ± 0.99 nm. The largest, most polydispersed nanoparticles were formed at feeding ratios of 1:3 and 1:2 which afforded particles with an average diameter of 12.85 ± 9.75 and 13.10 ± 9.49 nm respectively. The average diameters of nanoparticles synthesized at all other ratios were relatively consistent, with feeding ratios of 1:1, 2:1, 3:1 and yielding particles with average diameters of 6.74 ± 4.81, 5.37 ± 3.58, and 4.52 ± 3.67 nm respectively, comparable to that of pure silver nanoparticles which had an average diameter of 9.29 ± 2.24 nm. The substantial difference in size distribution at larger copper ratios can be ascribed to the reduction

of silver ions being more thermodynamically favorable (+0.799 eV) than the copper ions (+0.342 eV) thereby resulting in a much higher initial concentration of silver nuclei in solution from which larger nanostructures are seeded. Subsequently reduced copper atoms add onto these silver seed particles forming an alloy structure until the silver ions in solution are depleted, at which point the remaining copper atoms will create shells around these silver-seeded alloy particles as well as larger, more thermodynamically stable copper nanoparticles. When the concentration of copper ions is substantially large, such as in the $AgCu_3$ or $AgCu_3$ solutions, the resulting particles become larger and more polydisperse as the number of initial silver and copper nuclei become comparable therefore a variety of different alloy structures are formed due to differences in growth kinetics. At equal concentrations of silver and copper ions, the expected inhomogeneity seems to relax as the average size and distribution is much smaller than that of higher copper content solutions. This may represent the threshold at which the reduction kinetics of silver and copper ions is optimal for initial silver nuclei formation and subsequent copper ion reduction resulting in homogenously alloyed structures. This seems likely as at any higher concentrations of silver (2:1, 3:1, and 1:0), similar size distributions are observed. As suggested by Tsuji *et al.* at higher concentrations of silver ions, the reduction of Ag^+ to Ag^0 proceeds for a longer duration and therefore allows for subsequently reduced copper nuclei to incorporate within the structure forming alloy structures. At higher concentrations of copper, the silver ion reduction completes with a large excess of free copper ions remaining which cannot be incorporated as alloy structures, and

instead form shells around existing Ag or AgCu alloy structures.[34] Evidence supporting this growth mechanism was further provided by observing the surface morphologies of these bimetallic nanoparticles via HRTEM with high-magnification images revealing that most particles are covered by a copper oxide layer with lattice spacings of 2.31, 2.47, and 2.51 Å corresponding to the CuO (111), Cu_2O (111), and Cu_2O (-111) respectively. This is expected as copper is much more prone to oxidation than silver and the surface energy of copper oxide is lower than that of pure silver providing the driving force for migration of the oxide layer to the nanoparticle surface.[35] Additionally, due to the difference in reduction potentials, a galvanic exchange of Ag^+ ions in solution with Cu atoms on nanoparticle surfaces likely occurs, resulting in additional segregation of silver and copper atoms within alloy structures. This galvanic exchange may explain the observation of metallic silver domains observed in

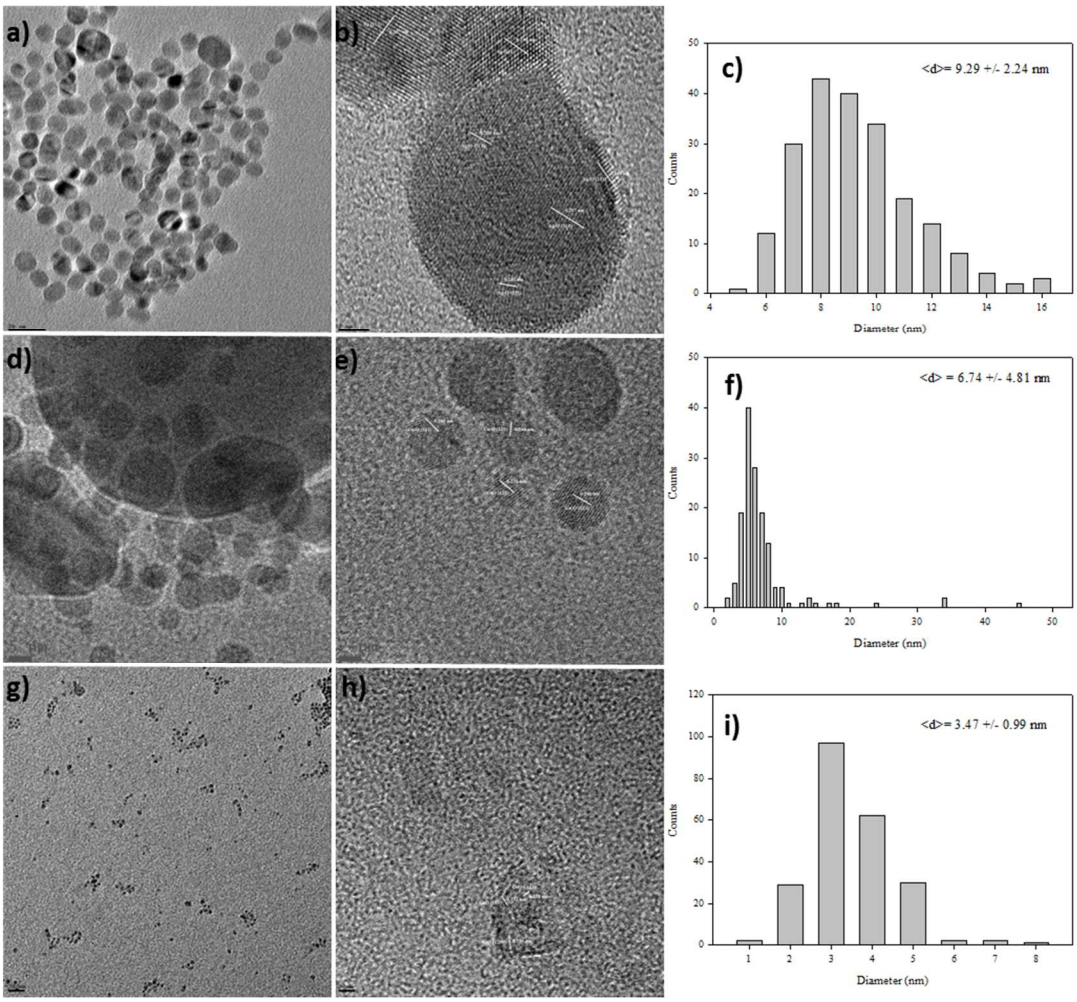

Figure 1. HRTEM images of (a,b) Ag, (d,e) AgCu, and (g,h) Cu nanoparticles with measured lattice spacings indicating Ag, Ag_2O, CuO, and Cu_2O domains as well as corresponding size-distribution histograms (c,f,i).

micrographs of the $AgCu_2$ sample. Pure copper domains, as evidenced by lattice spacings of approximately 2.05 Å, are observed only in the AgCu 1:1 and 1:2 samples which likely results from the stabilization of surface Cu atoms by Ag or AgCu alloy layers. This alloying effect prevents the oxidation of copper atoms on the surface by effectively increasing their reduction potential through charge-transfer from copper to

silver atoms. This is indeed observed as many lattice spacings are found to be between that of pure silver and the corresponding copper oxide. Interestingly, a variety of segregated alloy structures were also observed in several TEM images as is expected given the lattice strain given by the relatively large lattice mismatch (α_{Ag}/α_{Cu} = 1.13) of the two atoms. Additionally, the low reaction temperature serves to lower the configuration entropy which also favors segregation of the atoms. As predicted by the Gibbs free energy model proposed by Peng *et al*., bimetallic AgCu nanostructures prefer to be in the core-shell configuration as the surface energy of silver (0.553 eV/atom) is lower than that of copper (0.707 eV/atom) and under low temperature conditions, the free energy of the homogenous alloy is increased due to a decrease in configuration entropy.[36] Although these predictions suggest Janus structures to be unfavorable under the synthetic conditions used in this study, these structures were indeed observed in the TEM micrographs of the $AgCu_3$ sample. High-magnification images (**Figure S3**) confirm that there are two distinct domains, one comprised of silver/silver oxide and the other of copper oxide. The synthetic conditions in this solution provided the optimal condition to support Janus structures; a relatively few number of silver nuclei to which the large number of copper atoms could form shells around, affording the driving force for overcoming the free energy barrier between Janus and core-shell structures and ultimately resulting in a side-segregated nanostructures.[34,36,37] In contrast, core-shell structures are observed in all AgCu alloy nanoparticle solutions as illustrated by the clear predominance of copper oxide lattice spacings on the majority of nanoparticle surfaces although the underlying surface

composition varies in its Ag and Cu composition with samples having higher initial silver concentrations likely having a larger AgCu alloy domain.

UV-vis spectroscopy was utilized to characterize the optical properties of the as-prepared alloy nanoparticles and provides further evidence for the different types of alloy structures. For alloy nanoparticles synthesized using higher copper ratios (AgCu, $AgCu_2$,$AgCu_3$), a band centered at ~555 nm is observed, corresponding to the surface plasmon resonance (SPR) band of metallic Cu nanoparticles.[38] This is in good agreement with the absorption spectra of as-prepared citrate-capped copper nanoparticles (**Figure 2**) which exhibits a SPR peak centered at 565 nm. Interestingly,

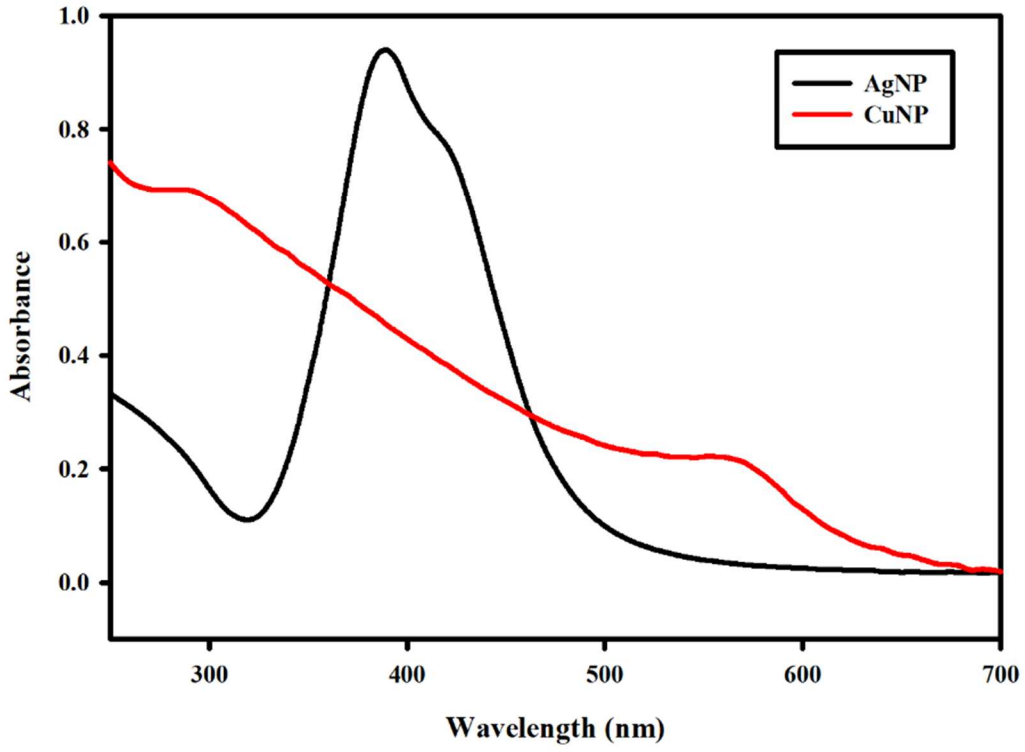

Figure 2. UV-vis spectra of Ag and Cu (x2.5) nanoparticle solutions.

aside from this SPR band and the typical exponential decay characteristic of Mie scattering, these citrate-capped copper nanoparticles also demonstrate an absorption

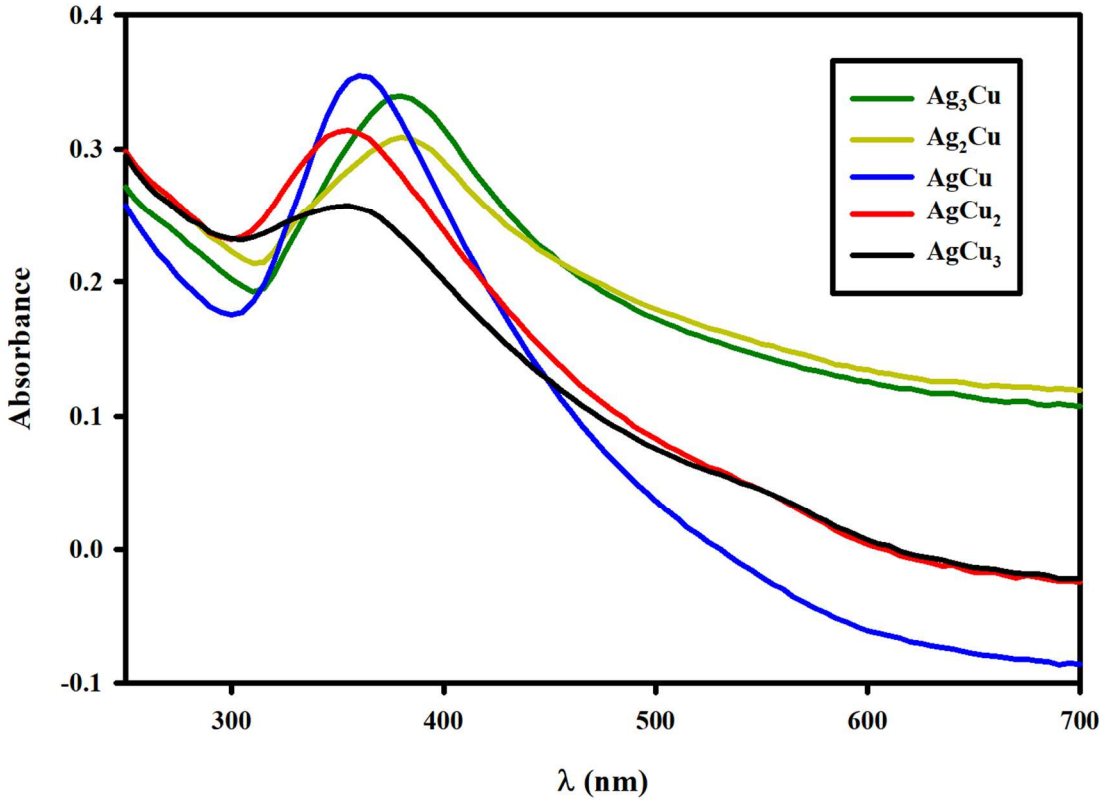

Figure 3. UV-vis spectra of AgCu alloy nanoparticles of carrying composition.

band centered at 290 nm which can be ascribed to molecular-like interband transitions of copper nanoclusters formed during the synthesis.[39-41] For pure silver nanoparticles synthesized under these conditions, the peak of the SPR band is centered at 389 nm, with a shoulder at 420 nm due to the small fraction of larger particles, which is in agreement with previous works.[42] UV-vis spectra for AgCu alloy nanoparticles synthesized at varying Ag and Cu feeding ratios is depicted in **Figure 3,** which

highlights the absorption around Ag SPR frequencies. This SPR peak position is found to blue-shift linearly with increasing copper feeding ratio, with peak positions of 354, 356, 361, 380, and 381 nm observed for $AgCu_3$, $AgCu_2$, AgCu, Ag_2Cu, and Ag_3Cu nanoparticle solutions respectively. This shift in the silver SPR position can be explained by considering the Drude model and the dependence of the plasma frequency (ω_p) on the concentration of free electrons in a metal (n_e):

$$\omega p^2 = (n_e e^2 m_e^{-1} \varepsilon_o^{-1}) \quad (16)$$

where e is the elementary charge of an electron, m_e is the effective mass of the electrons, and ε_o is the permittivity of vacuum.[43] Accordingly, when silver and copper atoms combine to form an alloy structure, copper atoms will transfer their charge to local silver atoms due to differences in electron affinity (1.30 eV for Ag vs 1.23 eV for Cu) resulting in an increased free electron number for silver atoms.[44] Consequently, the Ag ω_p will increase thereby resulting in a blue-shift of the SPR band which is in excellent agreement with theoretical predictions and experimental results.[43,45,46] At higher copper feeding ratios, more reduced copper atoms will be present at any given time, increasing the probability of coalescence with silver atoms to form homogenous alloy structures. These optical signatures therefore provide a good measure of the extent of alloying between the two metals, although further characterization is required to more completely accurately describe their alloy structures.

Ag, Cu and AgCu nanoparticles were characterized using X-ray photoemission spectroscopy (XPS) to identify the chemical environments around Ag

and Cu atoms in these alloy structures. A ligand-exchange reaction with 1-hexanethiol was used to protect nanostructures from oxidation, and the resulting nanostructures dissolved in toluene (**Figure 3**) and drop cast on silicon substrates for characterization. XPS spectra of Ag3d and Cu2p regions for all samples is shown in **Figure 4**, and a summary of Ag, Cu, S, and C peak positions as well as metallic composition is shown in **Table 1**. Two intense peaks are observed in the Ag3d region, confirming that these alloy nanoparticles have a significant silver component, as the typical doublet due to spin-orbit coupling is observed at approximately 367.5 eV (Ag $3d_{5/2}$) and 374.5 eV (Ag $3d_{3/2}$) with the proper spacing (6 eV) and ratio between peaks.[47] The position of the $Ag3d_{5/2}$ peaks for all samples are found to be at lower energy than that of metallic silver (~368.2 eV) indicating that the surfaces of these nanoparticles contain a significant proportion of oxidized silver.[48,49] This is reasonable as the surface of these nanoparticles are passivated by 1-hexanethiol ligands which serve to oxidize the surface Ag and Cu atoms, as well as the purification process being lengthy, allowing time for oxygen to come into contact with nanoparticle surfaces which can also lead to oxidation. This is supported by the presence of $S2p_{3/2}$ peaks (**Figure S5**) at ~167.2 eV, characteristic of metal-sulfate and metal-sulfonic acid bonds which are products of oxidized metal-thiol moieties.[52] Analysis of the Cu2p region reveals peaks characteristic of copper metal at ~932.5 eV ($Cu2p_{3/2}$) and ~952.5 eV ($Cu2p_{1/2}$) with shake-up satellite peaks observed at ~942.5 eV and 962.0 eV in AgCu, $AgCu_2$ and Cu nanoparticle spectra.[54,55] The positions of the $Cu2p_{3/2}$ peaks are found at higher binding energies for all samples except Ag_3Cu

and Ag_2Cu which likely have more segregated (Janus and core-shell) alloy structures resulting in larger pure copper domains which yield Cu2p binding energies closer to that of bulk copper. With Ag:Cu feeding ratios of 1 and lower there is an increase in $Cu2p_{3/2}$ and $Cu2p_{1/2}$ binding energies ($AgCu<AgCu_2<AgCu_3<Cu$) which agrees with UV-vis data as copper atoms in these resulting alloy structures have a greater degree of homogeneity allowing for a larger fraction of copper atoms to donate electron density to silver atoms, resulting in greater shifts of the Cu 2p binding energies to more positive values. This shift could also be due to the formation of copper oxide on nanoparticle surfaces, a likely consequence of charge-transfer to Ag, as samples demonstrating the highest Cu2p binding energies also exhibit satellite peaks in their spectra, indicative of Cu(II) species which readily formed.[54,56] A similar trend in

Table 1. XPS analysis of 1-hexanethiol functionalized AgCu nanoparticles[a]. Composition is quantified by the silver mole fraction (χ_{Ag}) as calculated from integration of Ag and Cu peaks.

	Ag	Ag_3Cu	Ag_2Cu	AgCu	$AgCu_2$	$AgCu_3$	Cu
C1s	285.79	285.37	285.35	285.25	285.21	285.96	286.95
$Ag3d_{5/2}$	367.07	367.28	367.32	367.62	367.83	367.69	-
$Ag3d_{3/2}$	373.06	373.28	373.32	373.81	373.78	373.65	-
$Cu2p_{3/2}$	-	932.42	932.50	932.80	932.99	933.18	933.77
$Cu2p_{1/2}$	-	952.37	952.41	952.84	952.78	953.10	953.69
$S2p_{3/2}$[b]	-	161.47	161.42	161.89	162.37	162.17	161.85
$S2p_{3/2}$[c]	166.91	166.49	166.81	166.96	166.95	167.39	166.93
χ_{Ag}	1	0.858	0.822	0.473	0.564	0.564	0

[a] Binding energies in eV. All values referenced to C1s = 284.5 eV.
[b] Corresponding to metal-sulfur bonds.[50,51]
[c] Corresponding to metal-sulfate/sulfonic acid bonds. [52,53]

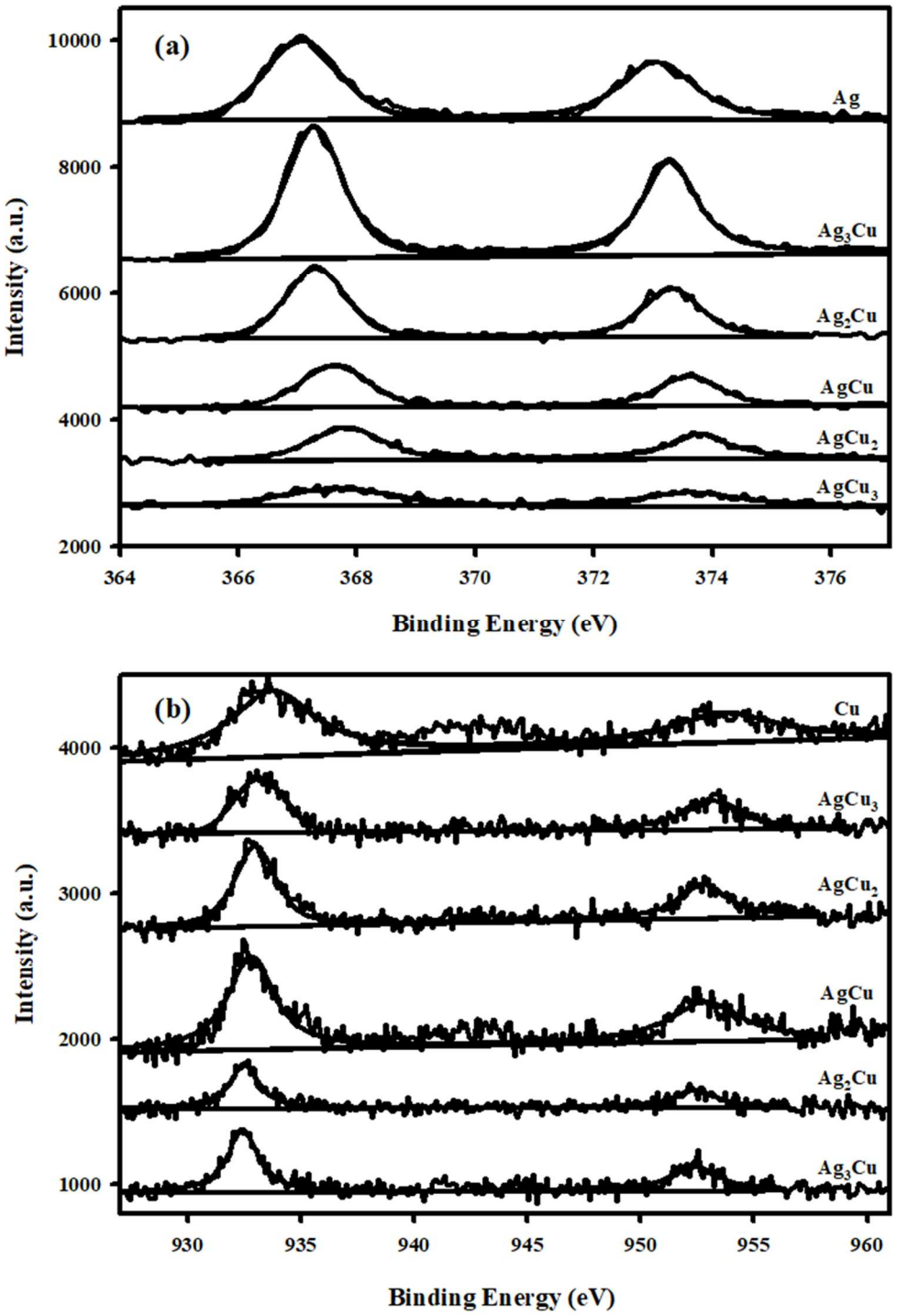

Figure 4. XPS spectra of Ag3d (a) and Cu2p (b) regions for all AgCu alloy nanoparticles.

binding energies is observed in the $Ag3d_{5/2}$ peak positions which demonstrate a roughly linear increase with Cu content. As higher binding energies imply a more metallic silver environment, this is likely due to transfer of electron density from copper atoms to silver atoms in the alloy structure.[48,49] These trends in XPS spectra are in agreement with the linear blue-shift of the Ag SPR position with increasing copper feeding ratio observed in UV-vis spectra, and provide direct evidence for the AgCu alloying effect.

The surface structure and composition of these nanostructures was further analyzed by cyclic voltammetry, allowing for the overall surface composition of alloy nanoparticles was determined. From the voltammogram shown in **Figure 5** and **S6**, it is clear that peaks corresponding to both silver and copper species are present in all alloys, and exhibit composition-dependent ratios of silver to copper peaks as well as peak position. Pure silver nanoparticles exhibited signals at +0.264, +0.319, and +0.662 V vs Ag/AgCl on the anodic sweep, corresponding to the formation of $Ag(OH)_2$, Ag_2O, and AgO layers on nanoparticle surfaces respectively, and, on the cathodic sweep, two peaks at +0.376 and -0.023 V corresponding to the electroreduction of AgO to Ag_2O and Ag_2O to Ag^0 respectively.[57] The voltammogram of pure copper nanoparticles exhibits similar features with peaks in the anodic scan observed at +0.005, and +0.207 V corresponding to the electrooxidation of Cu^0 to Cu_2O, and Cu^0/Cu_2O to CuO, respectively, and on the cathodic sweep, peaks at -0.515 V and -0.984 V are observed, corresponding to the electroreduction of CuO to Cu_2O and Cu_2O to Cu^0 respectively.[58] These features are

also observed in AgCu alloy nanoparticle voltammograms (**Figure S6**) albeit at different positions. A shift towards more positive potentials relative to pure Cu nanoparticles was observed for peaks corresponding to the electrooxidation of Cu^0 to Cu_2O for AgCu, $AgCu_2$, and $AgCu_3$ alloys. This is expected as highly homogeneous alloy structures should observe a shift in Cu electrooxidation potentials to more positive values because copper atoms will be stabilized toward oxidation due to alloying with silver which is in good agreement with UV-vis and XPS data. The AgCu sample affords the most stable copper-rich sample when compared to $AgCu_2$ and $AgCu_3$ nanoparticles, which has dramatic implications on its ion release kinetics, a key factor in targeted delivery.

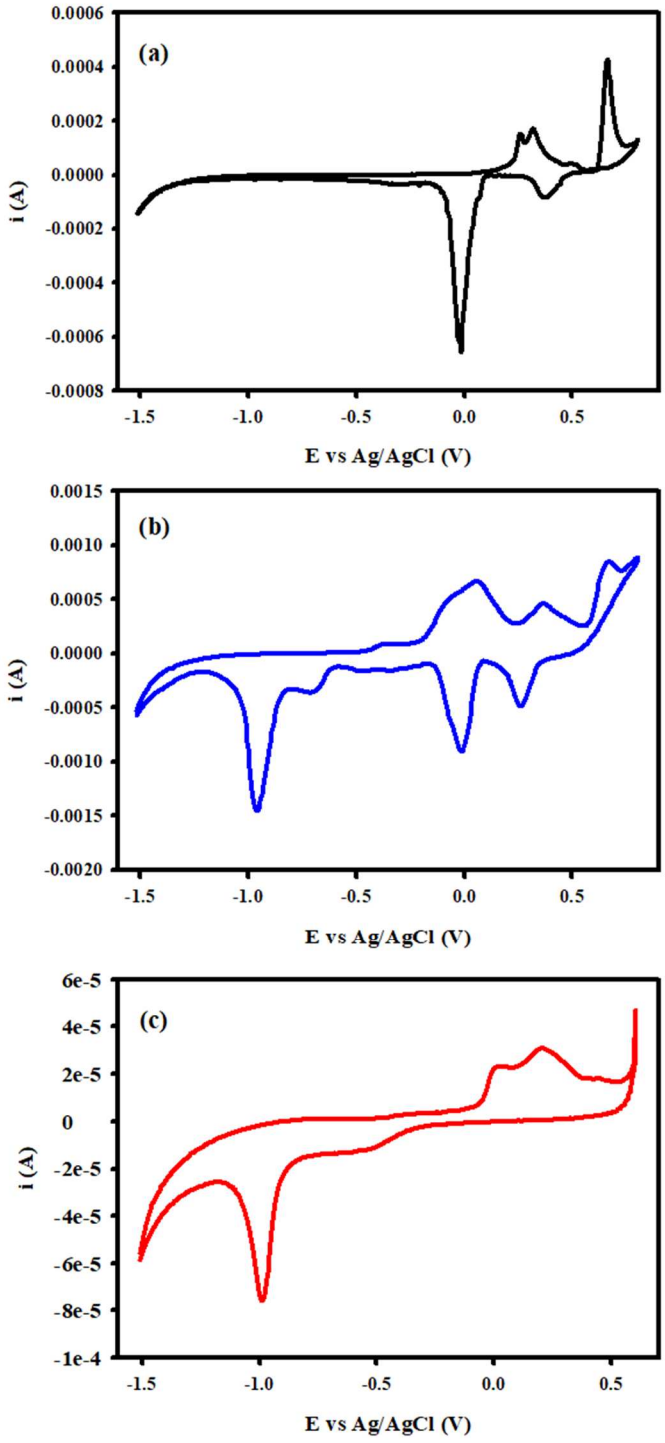

Figure 5. Cyclic voltammogram of 1-hexanethiol-functionalized (a) Ag, (b) AgCu, and (c) Cu nanoparticles in an aqueous, 0.1 M NaOH at a scan rate of 10 mV/s.

The oxidation kinetics of these resulting alloy nanostructures were examined via UV-vis spectroscopy. A micro-cuvette was filled with nanoparticle solutions and oxidation induced by passing a single air bubble to through the solution. UV-vis spectra were taken after each successive oxidation, and are summarized in **Figure 6** for Ag, Cu, and AgCu nanoparticles solutions, with up to 25 separate oxidations recorded depending on the nanoparticle composition. The change in the SPR peak position and absorbance was categorized into 4 discrete events (OE1-4) and is illustrated in **Figure S7**. In the first oxidation event (OE1), a gradual rise in the peak absorbance of the SPR band is observed which can be attributed to the dissolution of Ag atoms from small, less stable nanoparticles by the following mechanisms:

$$4Ag^0 + O_2 \rightarrow 2Ag_2O \quad (15)$$

$$2Ag^0 + 2OH^- \rightarrow Ag_2O + H_2O + 2e^- \quad (16)$$

with subsequent release and reincorporation of Ag^+ ions onto larger nanostructures via galvanic exchange with copper atoms or reduction by dissolved citrate molecules. This increase in peak height is only observed for alloy nanoparticles, as pure copper nanoparticles don't demonstrate a similar increase which suggests that this reincorporation of dissolved atoms occurs only for silver. This is likely because of the much larger reduction potential of Ag/Ag^+ compared with Cu/Cu^{2+}. A rapid decrease and red-shift of the absorption maxima is observed (OE2) following this ripening period, with copper-rich nanostructures exhibiting more dramatic changes in UV-vis spectra with fewer oxidation steps. This is due to the formation of a surface oxide layer which effectively increases the dielectric constant of the environment around

the metallic core, resulting in dampening and red-shifting of the SPR band.[37,59] Concurrently, an increase of absorption at 260 nm is observed, which corresponds to absorption due to copper-citrate complexes, and is a good measure of the number of copper ions released by the nanoparticles due to oxidation.[60] This is followed by a second, more abrupt increase in the SPR band absorption (OE3) likely due to a combination of a decreased dielectric constant due to dissolution of the oxide layer and the reincorporation of dissolved Ag^+ ions into nanostructures via galvanic exchange.[61] This is followed by a final decrease in absorption due to oxidation and subsequent dissolution (OE4) of the resulting structures. Samples with higher copper content experience a more dramatic decrease in SPR peak absorption over the course of oxidation steps, with a loss of 60%, and 51% observed for $AgCu_3$, and $AgCu_2$ samples respectively. This is much more stable however, than pure copper nanoparticles as these solutions lose 99% of their peak absorption in less than half the oxidation steps as depicted in **Figure 6c**. In contrast, alloy nanoparticles with larger silver content were much more stable over the course of these oxidation steps, with losses of only 22%, and 20% peak absorption observed for Ag_2Cu and Ag_3Cu nanostructures respectively as expected due to the enhanced stability of silver atoms towards oxidation. UV-vis spectra of AgCu alloy nanoparticle solutions after undergoing oxidation steps is shown in **Figure S8**. Relative to its copper content (52.7% by mass), the AgCu sample observed the highest stability toward oxidation,

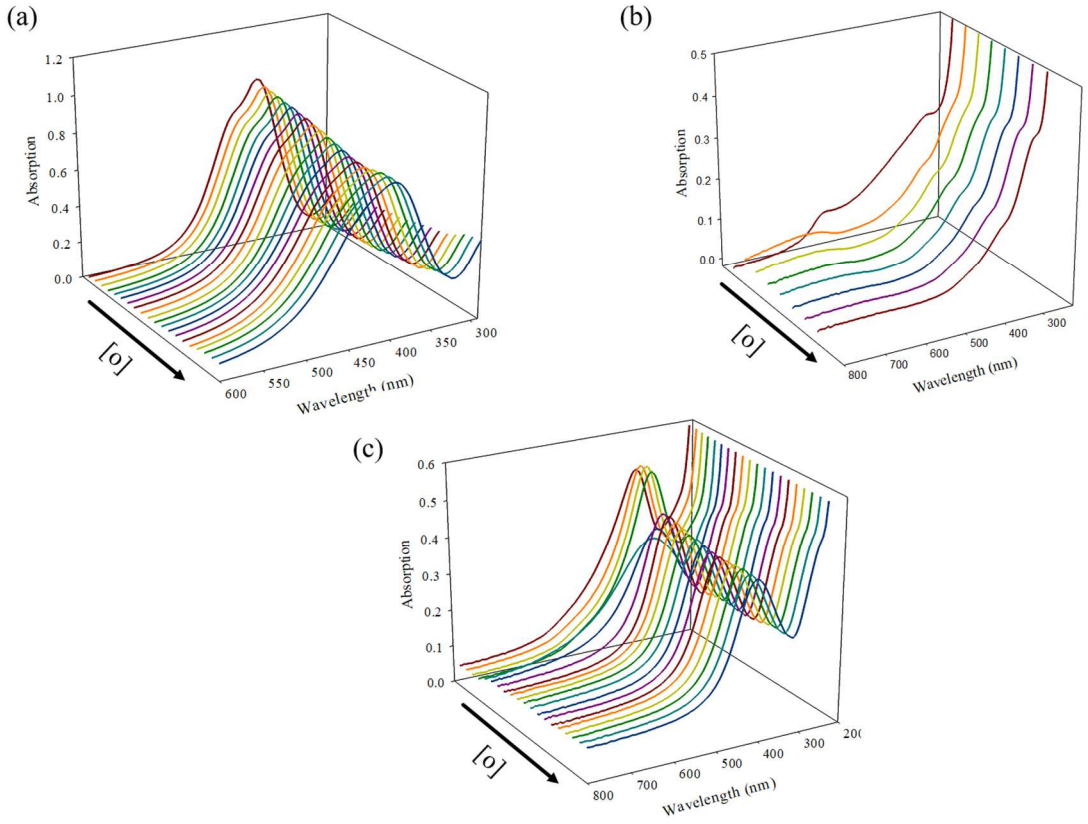

Figure 6. UV-vis spectra of Ag (a), AgCu (b), Cu (c) nanoparticle solutions over the course of oxidation.

with only a 26% drop in peak absorption over the course of oxidation steps. This is comparable to that of the silver-rich alloys and given that the majority of the structure is composed of copper, this sample is characterized by a markedly higher resistance toward oxidation likely due to the homogeneity of the alloy structure, and shift of alloyed Cu atoms oxidation potential to more negative values. This is expected as copper-rich surfaces such as those resulting from the Janus (**Figure S3**) alloy structures observed in the $AgCu_3$ nanostructures have a large fraction of their constituent copper atoms unalloyed, and localized on the particle surface which can

easily oxidize in solution and release Cu^{2+} ions. In contrast, the AgCu structures have much more homogenously alloyed structures (**Figure 1**) which stabilize copper atoms towards oxidation, resulting in a relatively slow release of Cu^{2+} ions into solution. A slow dissolution rate is highly advantageous for solution-phase antibacterial applications, as a delayed oxidation and subsequent dissolution increases the likelihood of nanostructures internalizing into bacterial cells and delivering their cytotoxic metal ions directly to biochemical targets. Release of cytotoxic metal ions by nanoparticles inside of a cell effectively increases the local concentration of Ag and Cu to values much higher than would be otherwise be achieved with equal concentrations of free ions in the bulk solution. This allows for toxic levels of these metal ions to be reached at much lower concentrations than that required when introducing ionic species into the solution. This targeted delivery also avoids sequestration by environmental complexing agents such as adenosine triphosphate released as a product of bacterial metabolism, and exopolysaccharides used in biofilm production.[62,63] As environments which can facilitate bacterial growth typically have a variety of complexing and chelating ligands present in addition to those released by bacterial cells themselves, a material which can remain stable under these conditions and therefore deliver these ions effectively into bacterial cells is highly advantageous for antimicrobial applications.

2.4.2 Antibacterial Activity of Ag,Cu, and AgCu Nanoparticles

AgCu alloy nanoparticle solutions were introduced into liquid cultures of *Escherichia coli* at varying concentration, and their antimicrobial activity evaluated. A table with a representative set of experimental conditions for this assay is shown in **Table S1**, and **Figures 7** and **S9** show growth curves at varying concentrations of nanoparticle solutions. Interestingly, copper nanoparticle solutions demonstrated no apparent inhibition of bacterial growth even at elevated concentrations as shown in **Figure S9**. In contrast, Ag, and especially AgCu alloy nanoparticle solutions indeed inhibited bacterial growth as defined by several growth parameters *vide infra*. To obtain a more quantitative assessment of the effects of nanoparticle solutions on bacterial growth, growth rate constants (k_g) were calculated over the first 30 minutes of the exponential growth phase by modeling bacterial growth as a first-order differential equation:

$$dN/dt = k_gN \quad (17)$$

where N is the number of bacteria at time t, and kg is the first-order growth rate constant. As optical density at 600 nm is proportional to the number of bacteria[64], this differential equation can be solved in terms of absorption, yielding the final expression:

$$\ln(A/A_o) = k_gt \quad (18)$$

where A and Ao are the absorptions at time t and at the onset of exponential phase, respectively. Linear regression analysis of equation 18 over the first 30 minutes of the

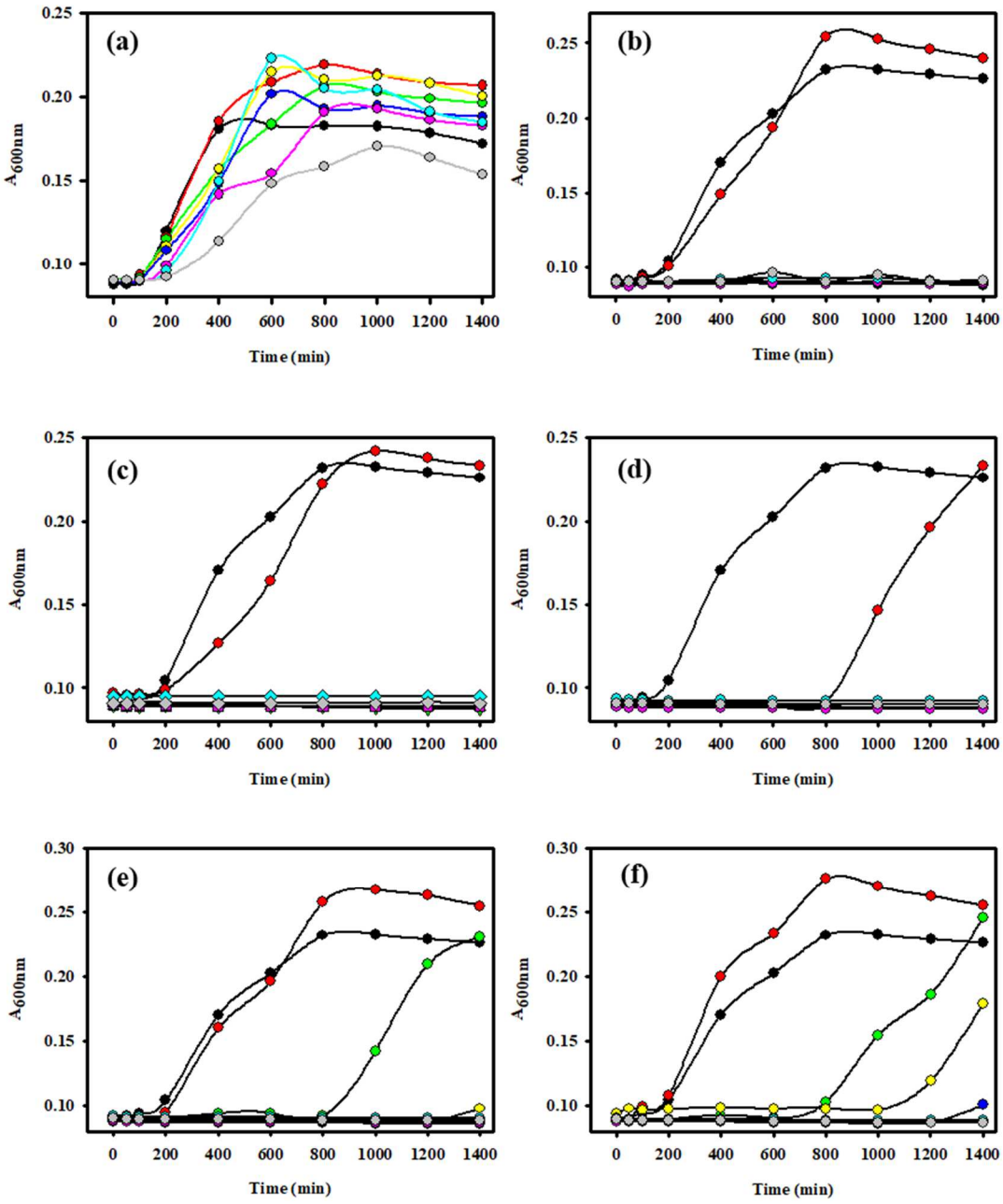

Figure 7. Growth curves for *E. coli* liquid cultures incubated with Ag (a), Ag_3Cu (b), Ag_2Cu (c), AgCu (d), $AgCu_2$ (e), and $AgCu_3$ (f) nanoparticle solutions. Black circles represent solutions with no AgCu nanoparticles added, red, green, yellow, blue, purple, cyan, and grey circles correspond to 2.5, 5.0, 6.0, 7.0, 8.0, 9.0, and 10.0 μM total nanoparticle concentrations respectively.

exponential growth phase allows for the calculation bacterial growth rate constants are shown in **Figure S9 and S10**, and values summarized n **Table S2-S4**. It is evident that even at extremely low (2.5 μM) concentrations, alloy nanoparticle solutions impede bacterial growth as evidenced by a decrease in k_g. At slightly higher concentration (5 μM), the growth rate constant is observed to increase for all samples which demonstrated growth, indicative of a strong metabolic response to the stress induced in response to cytotoxicity of Ag and Cu ions. This is expected as a study conducted by Weber *et al.* on the genome-wide transcriptional response of *E. coli* cells to various stress conditions (non-optimal temperature, pH shift, extreme osmolarity, and nutrient depletion) demonstrates a marked induction of the primary stress regulating sigma factor σ_S (RpoS), resulting in the upregulation of genes involved in metabolic processes such as glycolysis (pfkA, pfkB) and the electron transport chain (cybC, qor).[65] This boost in metabolism results in rapid consumption of ATP molecules as cellular processes are redirected from growth to homeostasis in order to repair and regenerate damaged and depleted cellular components. The return to homeostasis after adapting to stress from nanoparticle toxicity can be indirectly observed and quantified by the lag phase duration (T_L), as affected bacterial cells require longer periods of time to achieve optimal conditions for exponential growth after exposure to cytotoxic nanoparticle solutions. Lag phase durations were found to increase with concentration of nanoparticle solutions for all samples as depicted in **Figure 8** and is summarized in **Table 2**. The growth rate constant and lag phase duration can therefore provide parameters by which to evaluate the effects of

nanoparticle toxicity on bacterial cell proliferation, and comparisons between different nanostructures can be made more thoroughly. The two universally accepted evaluations of an antimicrobial agent's effectiveness are the minimum inhibitory concentration (M.I.C.), the concentration at which no observable increase in the absorption at 600 nm is observed over the growth period, and the minimum bactericidal concentration (M.B.C.), the concentration at which no viable cells remain after a subsequent incubation period, which were both quantified for each nanoparticle solution. The MICs for Ag and AgCu alloy nanoparticles are

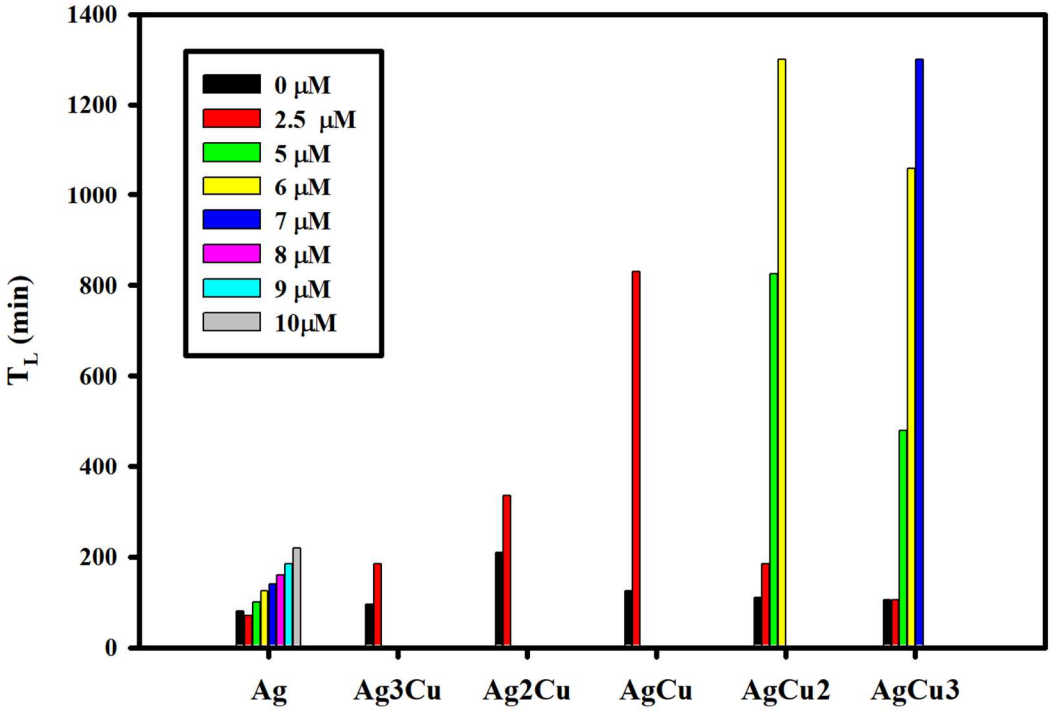

Figure 8. Bar Chart summarizing lag phase duration (TL) at varying concentrations of Ag and AgCu alloy nanoparticle solutions.

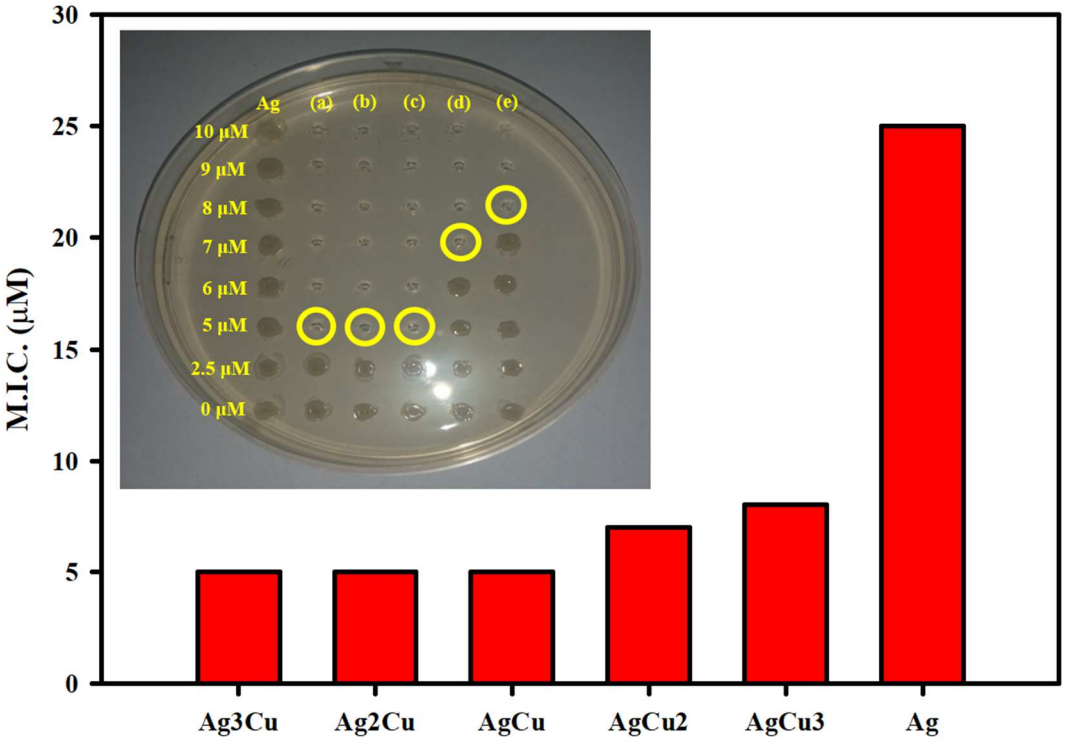

Figure 9. Bar chart indicating minimum inhibitory concentrations (M.I.C.) values obtained from *E. coli* growth curves for Ag and AgCu alloy nanoparticle solutions. A representative picture of a viability experiment illustrating the minimum bactericidal concentration (M.B.C.) is shown in the inset, demonstrating the results for Ag, (a) Ag_3Cu, (b) Ag_2Cu, (c) AgCu, (d) $AgCu_2$, and (e) $AgCu_3$ nanoparticle solutions.

summarized in **Figure 9**, and a representative photograph of the stamp plate used to quantify the M.B.C. with highlighted areas lacking growth are shown in the inset. From the comparison of these values, as well as growth kinetic parameters, a general trend in the activity seems to be apparent: AgCu alloy nanoparticles synthesized with larger silver feeding ratios were found to be more effective at inhibiting *E. coli*

growth as evidenced by lower M.I.C. values and a longer lag phase at sub-inhibitory concentrations. The sample with the highest antibacterial activity however, was found

Table 2. Summary of *Escherichia coli* lag-phase durations (T_L) at varying concentrations for AgCu alloy nanoparticle solutions.

Ag_mCu_n	0 µM	2.5 µM	5.0 µM	6.0 µM	7.0 µM	8.0 µM	9.0 µM	10.0 µM
Ag	80	70	100	125	140	160	185	220
Ag_3Cu	95	185	-	-	-	-	-	-
Ag_2Cu	210	335	-	-	-	-	-	-
AgCu	125	830	-	-	-	-	-	-
$AgCu_2$	110	185	825	1300	-	-	-	-
$AgCu_3$	105	105	480	1060	1300	-	-	-

to be the AgCu alloy nanostructure, the root of which is likely from its composition as it had a similar size distribution as Ag_3Cu and Ag_2Cu nanostructures, but a significantly higher copper content by mass as calculated by XPS. This nanoparticle solution not only exhibited an equal M.I.C. value (5 µM) as those of the Ag_3Cu and Ag_2Cu samples, but also demonstrated a markedly longer TL (830 min) at the sub-inhibitory concentration of 2.5 µM which is 4.5 and 2.5 longer than Ag_3Cu and Ag_2Cu solutions respectively. These values are in stark contrast to the $AgCu_2$ and $AgCu_3$ samples which, although having slightly higher copper contents, observed M.I.C. values of 7 µM and 8 µM respectively and markedly shorter lag phase duration at sub-inhibitory concentrations. TEM micrographs revealed Ag_3Cu, Ag_2Cu, and AgCu nanoparticles to be approximately the same size (~5 nm) on average, with majority of observed particles measured at less than 10 nm. A systematic study by Agnihotri *et al.* correlating the size (5-100 nm) of silver nanoparticles to their antibacterial activity, concluded that smaller silver nanoparticles, particularly those

under 10 nm, were the most effective at inhibiting bacterial growth.[66] The enhanced activity exhibited by smaller nanoparticles is attributed to an enhanced surface-to-volume ratio which provides increased interactions with target molecules, in the case of gram-negative bacteria such as *E. coli*, as the oxygen functional groups of the O-antigen domain of lipopolysaccharide (LPS) molecules located on the cell surface.[66-69] Furthermore, the extremely small size of these nanoparticles affords a greater number of undercoordinated atoms on nanoparticle surfaces which increase the surface energy and consequently, their reactivity.[66,70] The AgCu nanoparticles however, demonstrated a higher antibacterial activity than the Ag3Cu and Ag2Cu solutions, which, when considering the similarity in average size, is attributed to the substantial difference in copper content of the resulting nanostructures. The AgCu nanoparticle cores were found to be composed of 48% copper and 52% silver by XPS analysis, which agrees with spectroscopic and electrochemical measurements. When compared with Ag nanoparticles of similar size, the difference in activity is substantial as pure silver nanoparticles have a M.I.C. value of 25 μM which is far higher than any of the AgCu alloy nanoparticles as observed previously.[71] This also agrees with a previous study conducted by Yoon *et al.* comparing the antibacterial activity of commercial silver and copper nanoparticles which found that copper nanoparticles were superior in inhibiting the growth of both *Escherichia coli* and *Bacillus subtilis* in liquid media.[72] This does not however, explain the markedly lower activity of the $AgCu_2$ and $AgCu_3$ alloy nanostructures as they have only slightly (~9%) less copper content than the highly active AgCu sample, yet demonstrated a

significantly lower activity. One reason for this discrepancy may be the difference in size, as a significant population of $AgCu_2$ and $AgCu_3$ nanostructures were larger than 10 nm with particles as large as 50 nm observed in both solutions. Larger particle sizes are highly disadvantageous for antibacterial applications as it is much more difficult for large structures to penetrate cell membranes and deliver the ionic species directly inside bacterial cells. The discrepancy in activity can however, also be rationalized in terms stability and subsequent ion release of copper atoms within the nanoparticle structure. This is evident as AgCu nanostructure metallic cores are 53% copper by mass, yet demonstrate considerably higher stability in oxidative conditions compared with $AgCu_3$ and $AgCu_2$ copper nanoparticles which were both calculated to be approximately 43% copper by mass. This enhanced stability was quantified by UV-vis spectroscopy (**Figure S8**) in which the SPR band for AgCu nanoparticles retained 74% of its peak absorption over the course of extensive oxidation, in stark contrast to $AgCu_2$ and $AgCu_3$ nanoparticle solutions which retained only 40% and 49% of their SPR absorbance over the same respectively. Although the Ag_2Cu and Ag_3Cu structures were found to be more stable with 78% and 80% SPR peak retention respectively, they contained relatively low copper content which explains the slightly lower antibacterial activity compared with that of the AgCu sample. The primary basis for the superior antibacterial activity of AgCu nanostructures is therefore concluded to originate from having an optimal alloy structure for stabilizing and subsequently delivering high concentrations of copper ions directly into bacterial cells, thereby exhibiting the highest synergistic Ag and Cu cytotoxicity.[71] This is

supported by findings by Valodkar *et al.* who studied the inhibitory effects of silver-copper alloys and concluded that copper ions were the more active antibacterial species[72]. Cu^{+} ions are soft acids and therefore have similar affinities to molecular targets as that of Ag^{+} ions, so the difference in their antibacterial activity is most likely due to thermodynamically favorable Fenton chemistry. As these Cu species produce reactive oxygen species directly, more severe oxidative damage via hydroxyl radicals and superoxide anions is expected.[16] This was experimentally observed *in-vivo* by utilizing fluorescence microscopy and CellROX Green, a cell-permeable fluorescent dye which is activated specifically by hydroxyl radicals and superoxide anions inside cells. A 2 μL drop of *E. coli* cell suspension (O.D.600 nm = 0.1) incubated with 5 μM CellROX was first placed onto a glass slide and brought into focus. Once an optimal focal plane was established, images were captured every second using a 488 nm laser at an exposure time of 100 ms for a total of 12 min. After a given time period, a 2 μL drop of Ag, AgCu, or Cu nanoparticles was added to the bacterial suspension and fluorescence intensity observed over time. Representative frames before addition, and 1, 5, and 10 minutes after addition in **Figure 10**. Associated graphs of average CellROX fluorescence over time are illustrated in **Figure 11**, and show that AgCu alloy nanoparticle solutions create the highest levels of ROS inside bacterial cells over the given time frame. Interestingly, although CuNP solutions do not inhibit bacterial cell growth even at elevated concentrations, they produce an almost equal level of ROS over the same time frame. The rate of ROS generation by these nanoparticle solutions can be quantified via linear regression of

the fluorescence intensity over the first 30 seconds of stable fluorescence increase, by the following equation:

$$\ln(I/I_o) = k_{ROS}t \quad (18)$$

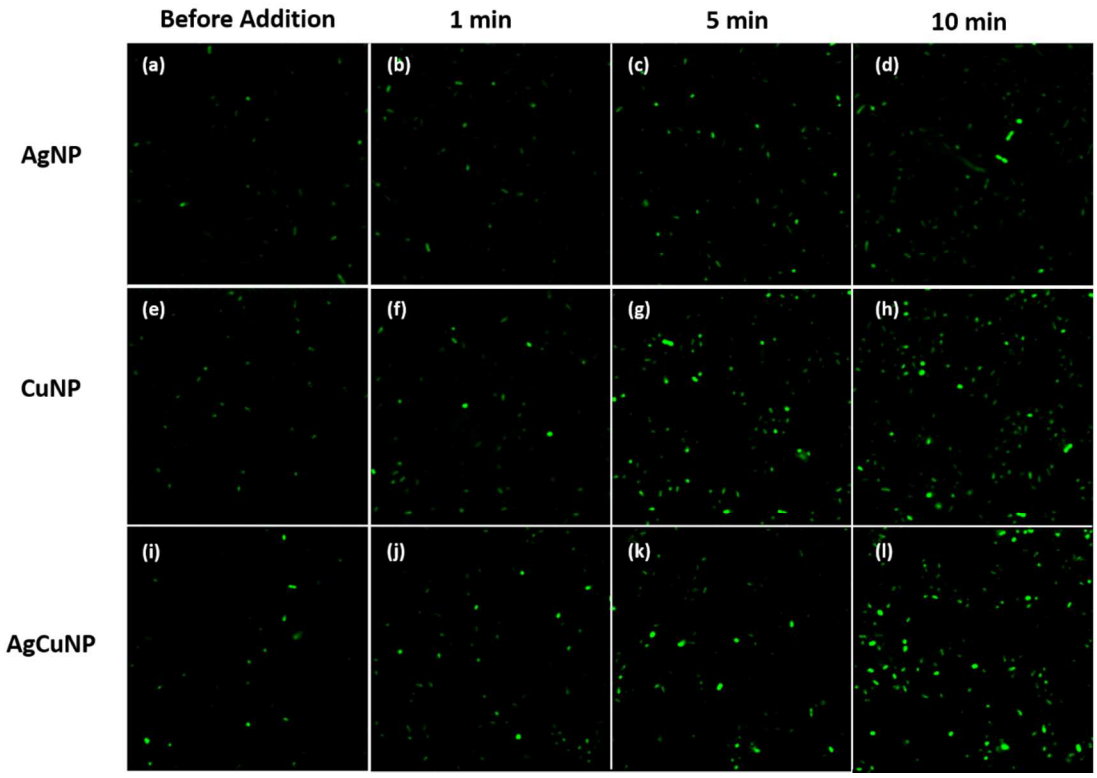

Figure 10. Fluorescence microscopy images of *E. coli* cells incubated with 5 μM CellROX at different time intervals before and after addition of Ag (a-c), AgCu (d-f), and Cu (g-i) nanoparticle solutions.

where I and Io are the fluorescence intensities at time t and at the onset of stable, linear fluorescence increase respectively, and k_{ROS} is the pseudo-first-order rate constant for the generation of ROS inside bacterial cells. These plots are shown in **Figure 12**, and a bar chart summarizing the calculated rate constants in the inset.

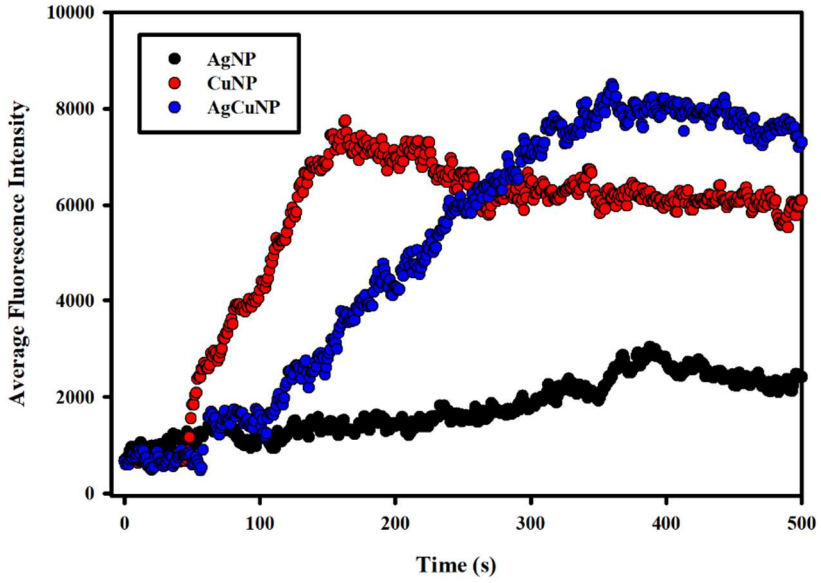

Figure 11. Normalized CellROX fluorescence intensity of *E. coli* cell suspensions immediately following the addition of Ag, AgCu, and Cu nanoparticle solutions.

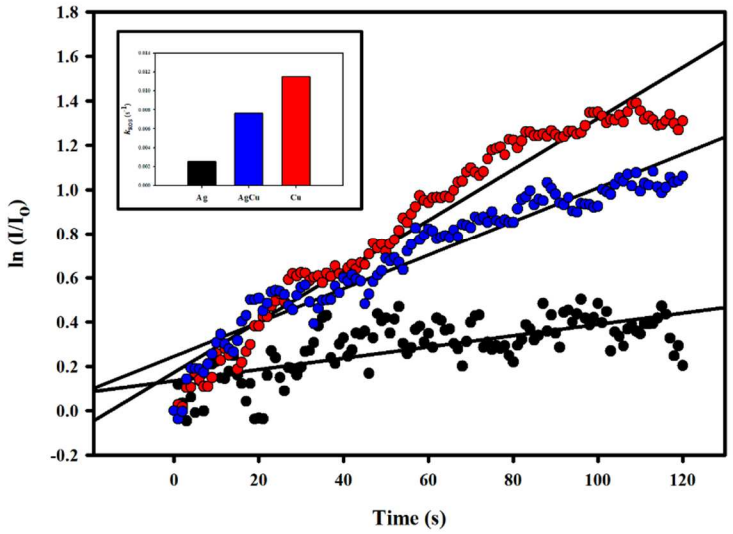

Figure 12. Log plot of the ratio of fluorescence intensity at time t to the baseline fluorescence vs time with bar chart (inset) summarizing k_{ROS} values obtained from regression lines in for Ag, Cu, and AgCu alloy nanoparticle solutions.

Values of k_{ROS} were determined to be 2.4 e^{-3}, 7.9 e^{-3}, and 2.1 e^{-2} s^{-1} for Ag, AgCu, and Cu nanoparticle solutions respectively. A correlation between the rate of ROS production inside cells and their copper content can therefore be drawn, and ROS production inside cells concluded to be significantly increased by copper species in the nanoparticle structure, most likely through direct catalysis of Fenton reactions. Copper species will generate ROS both directly through Fenton chemistry, and indirectly by exchanging with iron in the iron-sulfur clusters of respiratory chain proteins resulting in the release of Fe^{2+} ions which subsequently produce ROS via the Haber-Weiss cycle.[5,10,16] This sudden increase in levels of reactive oxygen species is observed to correlate with aggregation of bacterial cells as can be seen in **Figure 13**. After only 15 seconds, Cu and AgCu nanoparticle solutions begin to induce noticeable aggregation of bacterial cells, whereas aggregations became apparent only after 30 seconds for Ag nanoparticle solutions. After 5 minutes, significant aggregation is seen for Cu and AgCu, which cause the largest, most intensely fluorescent aggregates whereas Ag nanoparticles solutions roughly half as many aggregations. It is known that dead or damaged bacterial cells release DNA and other extracellular biomolecules such as polysaccharides into their environments as a result of membrane disruption or lysis, both of which are expected consequences of

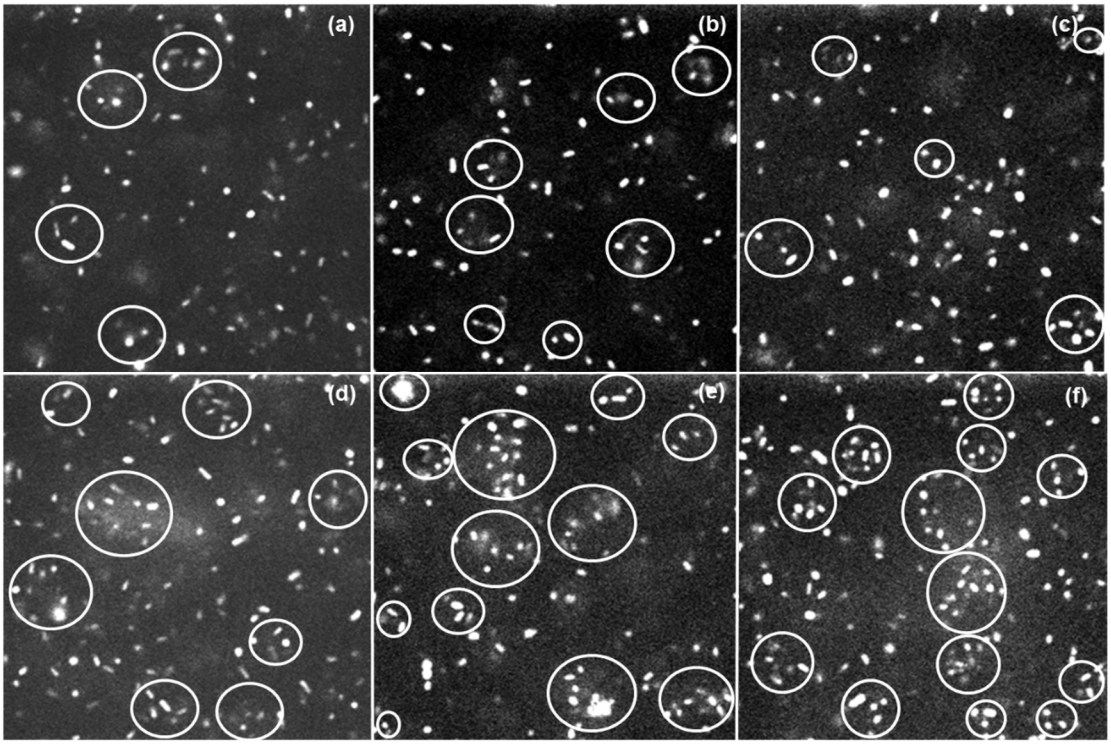

Figure 13. Fluorescence microscopy images of bacterial aggregations resulting from addition Ag (a,d), AgCu (b,e), and Cu (c,f) nanoparticles to cell suspensions. Top panels a,b, and c show images taken 30, 15, and 30 seconds after addition respectively, and images in bottom panels (d,e,f) were taken 300 seconds after addition.

Ag, AgCu, and Cu nanoparticle toxicity.[73,74] Although Cu nanoparticles had no inhibitory activity, they were observed to cause a significant degree of aggregation, much more even than that of the Ag nanoparticle solution which had apparent cytotoxicty. It has been reported that bacterial cells will release cellular biomolecules, particularly K^+, in the presence of Cu^{2+} in an attempt to reestablish a viable membrane potential.[75] Additionally, leakage of other charged biomolecules occurs, all of which increase the effective ionic strength of the surrounding media thereby effectively lowering the ionic repulsions of negatively charged bacterial surfaces and

causing cells to aggregate. In fact, disruption of the membrane potential also causes a misbalance of the H^+ gradient which could effectively increase the pH around the inner membrane where H_2O_2 levels are elevated, resulting in an increased rate of Fenton reactions in the presence of Fenton-active metals. This agrees with findings by Gonzalezflecha *et al.* which suggested that as much as 87% of cellular hydrogen peroxide is synthesized as a byproduct of the enzymes of the electron-transport chain (NADH dehydrogenase and ubiquinone), therefore Cu ion-catalyzed Fenton reactions will be primarily localized around the inner-membrane.[76] This model correlates well with the rate of ROS production inside bacterial cells observed in fluorescent micrographs, as Ag nanoparticles had a k_{ROS} value over three times less than AgCu nanoparticles, and almost an order of magnitude less than that of Cu nanoparticles. As these k_{ROS} values seem linear with Cu composition, the observed generation of ROS is likely direct, catalyzed primarily by Cu Fenton chemistry, for Cu and AgCu alloy nanoparticles and indirect, catalyzed by released Fe^{2+} ions for Ag nanoparticles. Although levels of ROS are maximal for Cu nanoparticles, this induced oxidative stress does not inhibit the growth of *E.coli*, as cells show no growth inhibition even at elevated concentrations of Cu nanoparticles. This can be explained by the evolution of bacterial cells in an aerobic environment; as ROS are always present in bacterial cells, often at very elevated concentrations, they have evolved very effective mechanisms of detoxification in order to survive this type of cytotoxicity. Therefore, an environment with elevated ROS concentration, such as that caused by Cu nanoparticles, will be easily adapted to and bacteria will survive without major

inhibition of growth. Silver toxicity however, is not a typical environment which bacteria have adapted to, therefore exposure to this element will severely damage bacterial cells and cause growth inhibition as observed in this study. The observed superior antibacterial activity of AgCu alloy nanoparticles must therefore arise from a synergistic combination of enhanced ROS generation provided primarily by copper species, and non-ROS toxicity by Ag species including dysfunction of proteins caused by oxidation of cysteine residues and other cellular sulfur species, and transcriptional arrest resulting from the binding heterocyclic nitrogens of DNA base-pairs.[4,76]

To provide additional evidence for this conclusion, the *in-vitro* production of hydroxyl radicals through Fenton chemistry was measured using electron paramagnetic resonance (EPR) and the spin trap 4-POBN. This molecule is utilized as a hydroxyl radicals trap, as these ROS species react readily with its nitrone moiety to form a stable, nitroxide spin adduct that can be detected using EPR. Upon addition of Ag, Cu, and AgCu alloy nanoparticles to a buffered (pH=2) solution containing 4-POBN and hydrogen peroxide, an EPR spectrum with characteristic hyperfine splitting of the 4-POBN-hydroxyl radical spin adduct resulted, demonstrating six lines with signal intensities ratios of 1:1:1:1:1:1 as seen in **Figure 14**. The splitting parameters measured for this spin adduct were a_N = 15.1 G and a_H = 1.7 G which are in agreement with previous measurements of hydroxyl radical and 4-POBN spin adducts[78]. By measuring the peak-to-peak height of the center line of the 4-POBN signal, the relative amount of hydroxyl radicals generated can be compared between

nanoparticle solutions. A close-up of this doublet centered at 3365 G is seen in **Figure 15**, which visually demonstrates differences in the peak-to-peak amplitude of the EPR line for each sample. It can be clearly seen from the bar chart that AgCu alloy nanoparticles generate more hydroxyl radicals then both Ag and Cu

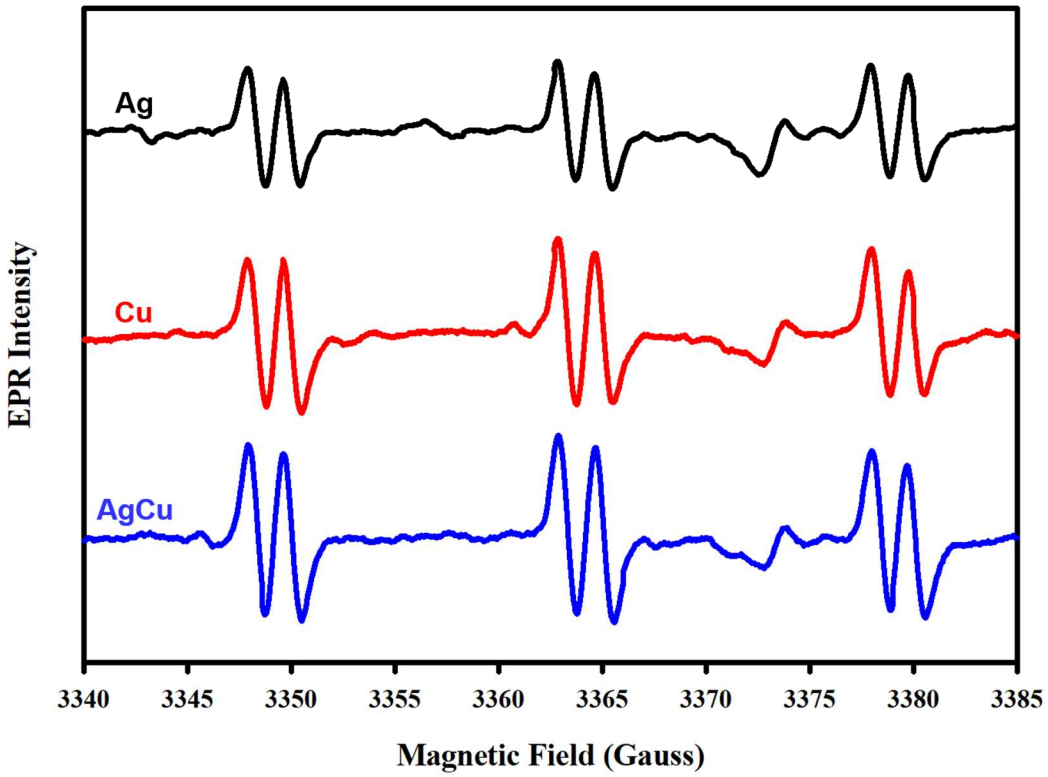

Figure 14. EPR spectra of solutions containing 100 μM 4-POBN, H_2O_2, and Ag (Black Curve), Cu (Red Curve), and AgCu alloy (Blue Curve) nanoparticle solutions.

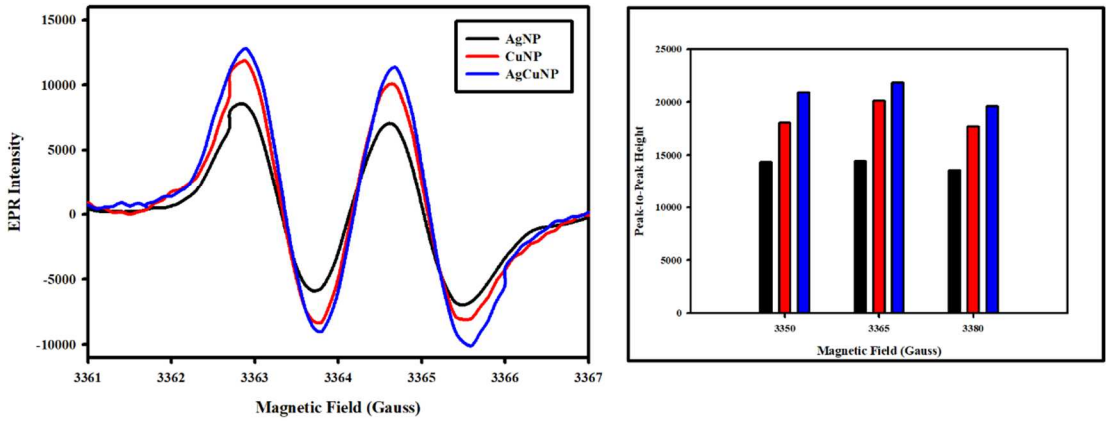

Figure 15. Comparison of EPR intensities for peak centered at 3365 G for Ag, Cu, and AgCu alloy nanoparticle solutions (left) and bar chart (right) comparing peak-to-peak heights for each set of peaks.

nanoparticle solutions, which is in excellent agreement with fluorescence micrographs. As line-widths of the 4-POBN signal were not different between nanoparticle solutions, the same spin adduct is concluded to be formed by all nanoparticles.[78] This indicates that AgCu alloy nanoparticles, although having less than half the copper content than Cu nanoparticles, catalyzes Fenton reactions more readily. Based on previously mentioned spectroscopic evidence, this can be concluded to be due to the alloying effect stabilizing Cu atoms from oxidation by molecular oxygen, thereby increasing their likelihood to catalyze Fenton reactions. Additionally, the Ag atoms in these alloy nanoparticles could also be participating in Fenton reactions. Compared with the pure Ag nanoparticles, their reduction potential experiences a decrease due to alloying thus becoming closer to that of the hydrogen peroxide/hydroxyl radical redox potential, thereby increasing the rate of Fenton reaction catalysis. Combined, fluorescence micrographs and EPR spectra give an *in-*

vivo and in-vitro evaluation of the ROS generation capability of Ag, Cu, and AgCu nanoparticles respectively allowing for the differentiation of the mechanisms of their cytotoxicity towards bacterial cell. A schematic model of the proposed mechanisms of AgCu alloy nanoparticle cytotoxicity is given in **Figure 16**, and illustrates the enhanced stability of Cu atoms towards oxidation, the enhanced activity of Ag atoms towards Fenton reactions, and the effect this has on the overall ROS generation and cytotoxicity

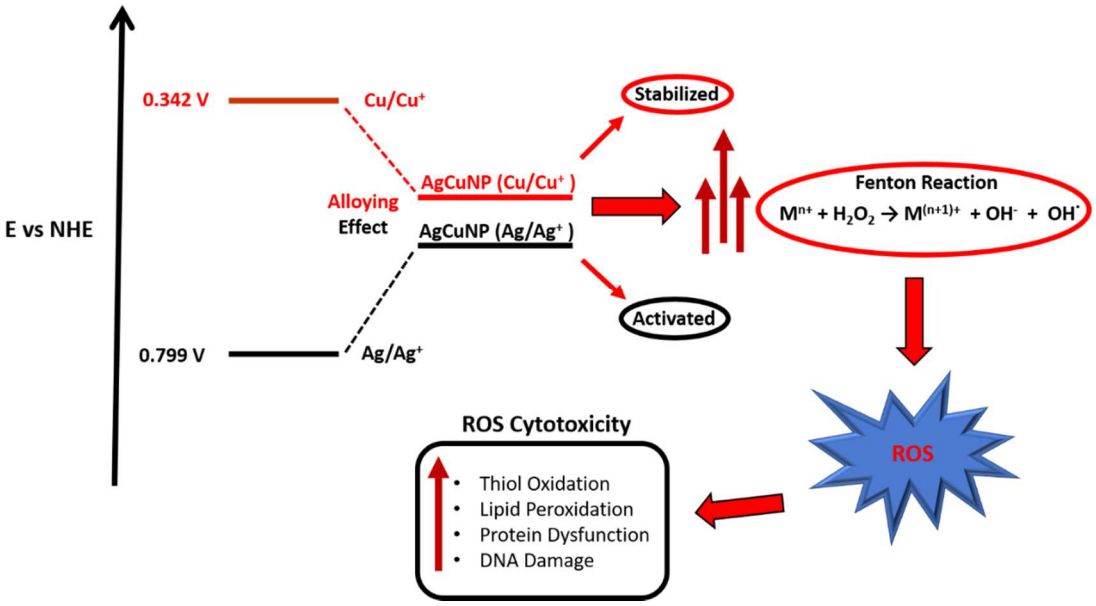

Figure 16. Schematic diagram of proposed mechanism of enhanced cytotoxicity for AgCu alloy nanoparticles, highlighting their increased propensity for Fenton chemistry.

towards bacterial cells. The combination of enhanced ROS generation of alloyed Ag and Cu atoms, as well as their specific cytotoxic effects allow AgCu alloy nanoparticles to exert a significant synergistic antibacterial activity, creating an even more broad-spectrum effect than each individual species alone. This unique,

homogeneously alloyed nanostructure, provides the effective antibacterial activity required to address the antibiotic resistance crisis, and presents a fundamental platform by which to design broad-spectrum antimicrobial materials.

2.4 Conclusion

Silver-copper alloy nanostructures of varying size and composition were successfully synthesized using a facile co-reduction of silver and copper ions in an aqueous solution. The antibacterial activity of the resulting structures was evaluated against *Escherichia coli*, and AgCu nanoparticles with nearly equal Ag and Cu content were found to exhibit the highest antibacterial activity. Spectrokinetic studies revealed these nanoparticles to be highly stable towards oxidation and subsequent release of copper ions, likely due to their homogenously alloyed structure. By utilizing fluorescence microscopy, the generation of reactive oxygen species by these metallic nanoparticles was observed *in-vivo* and in real-time for the first time. These micrographs agree well with electron paramagnetic resonance studies indicating that AgCu alloy nanoparticles have superior ROS generation capabilities likely due to stabilized Cu atoms in their structures. Alloying of two bactericidal metals at the nano-scale was found to be an effective method for enhancing the antibacterial activity of Ag and Cu nanostructures, and, by systematically studying their structural properties, a foundation for understanding Ag and Cu cytotoxicity in bacterial cells was established

2.5 Acknowledgements

We would like to thank Dr. Bill Saxton and Dr. Susan Strome of the UC Santa Cruz MCD biology department for access to their spinning disk confocal microscope, as well as Dr. Benjamin Abrams for training and technical assistance with fluorescence microscopy experiments.

2.6 Supporting Information

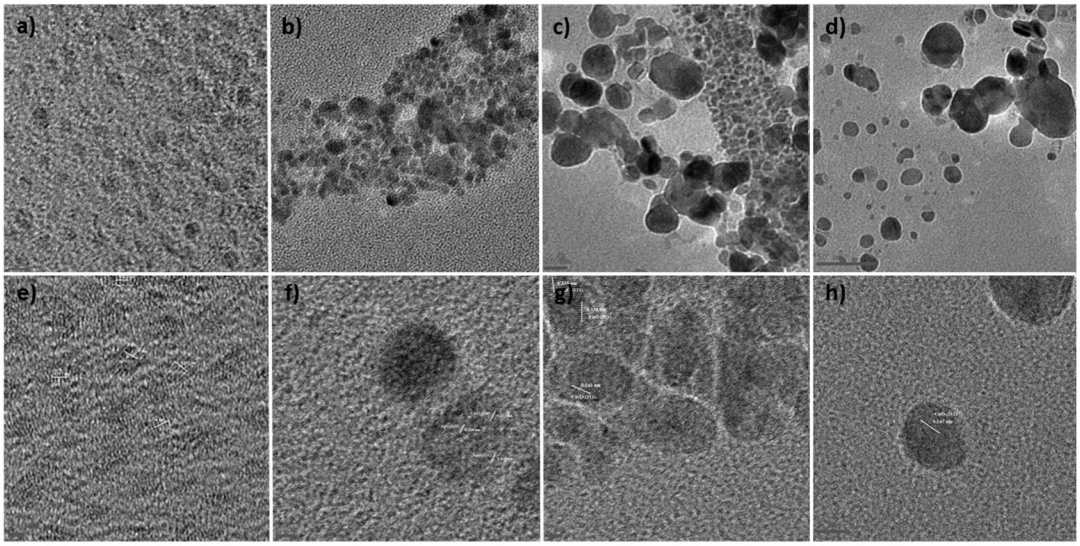

Figure S1. HRTEM images of (a, e) Ag_3Cu, (b, f) Ag_2Cu, (c, g) $AgCu_2$, and (d, h) $AgCu_3$ nanoparticles with highlighted lattice spacings (e, f, g, h) for each sample.

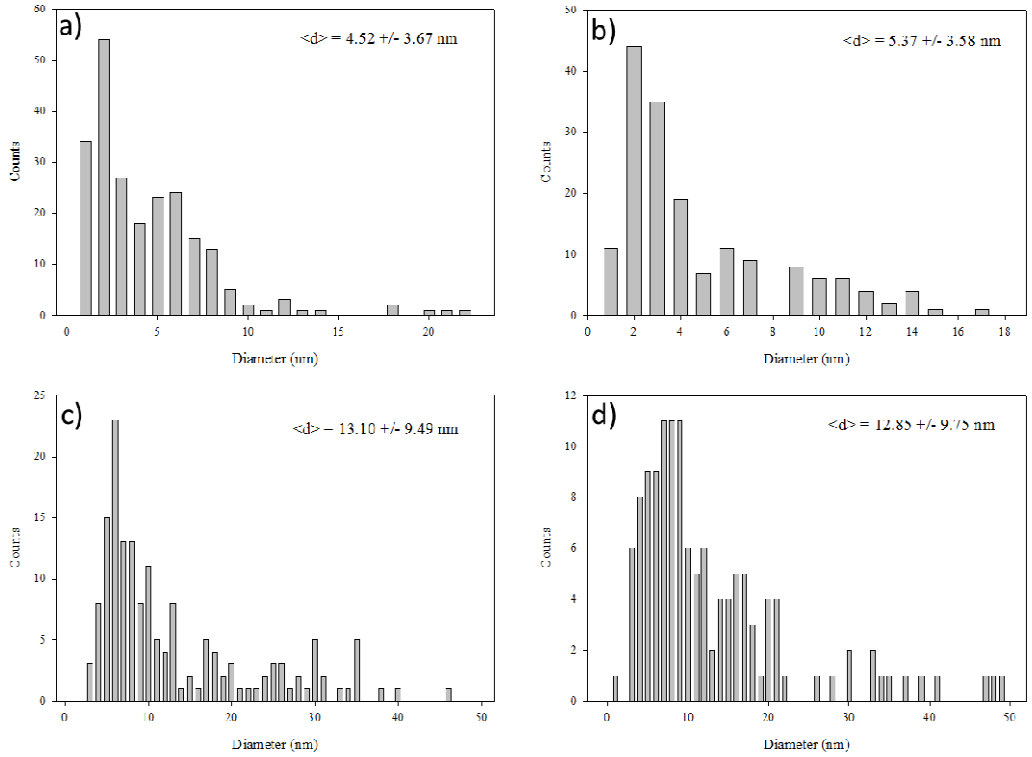

Figure S2. Size-distribution histograms for Ag_3Cu (a), Ag_2Cu (b), $AgCu_2$ (c), and $AgCu_3$ (d).

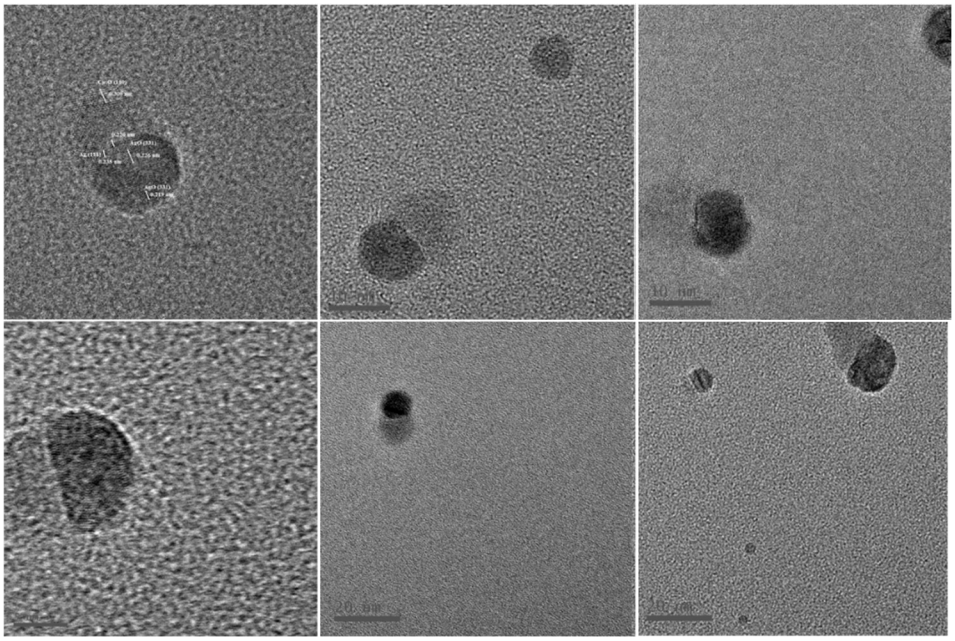

Figure S3. HRTEM images of Janus nanostructures observed in the AgCu nanoparticle solutions with measured lattice spacings.

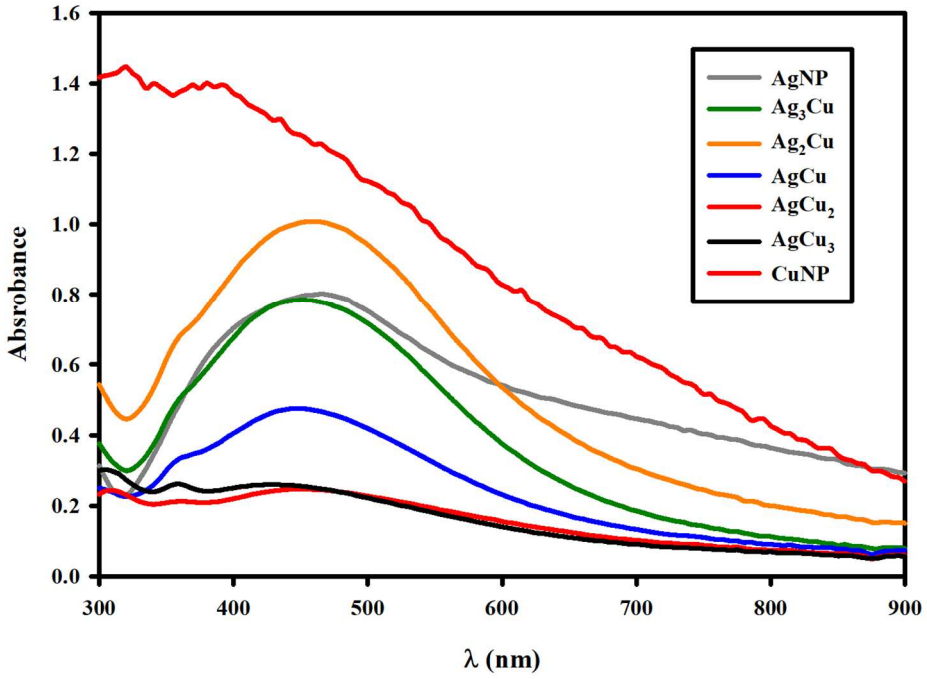

Figure S4. UV-vis spectra of Ag, Cu, and AgCu alloy nanoparticles in toluene after undergoing ligand-exchange reaction with 1-hexanethiol.

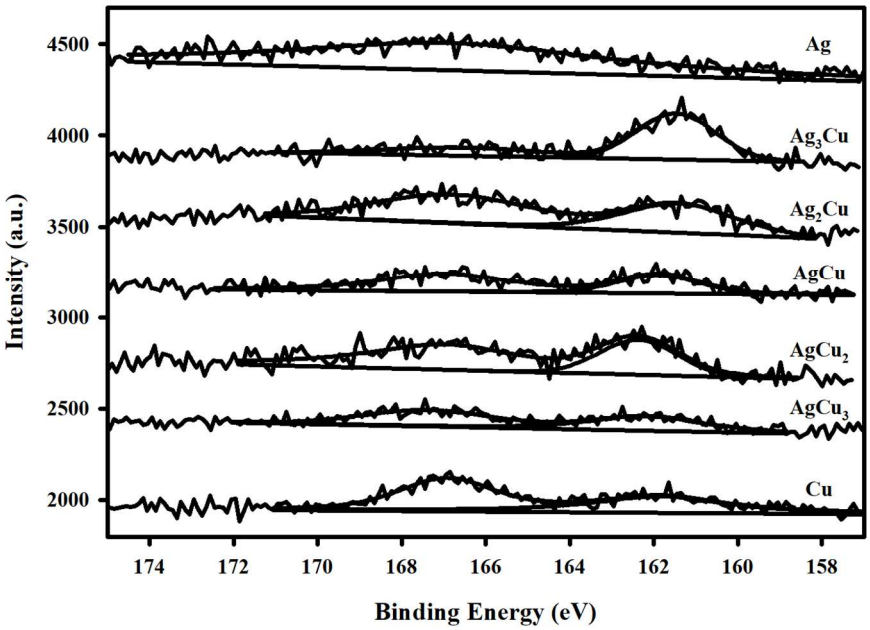

Figure S5. XPS spectra of S2p region for Ag, Cu, and AgCu alloy nanoparticles.

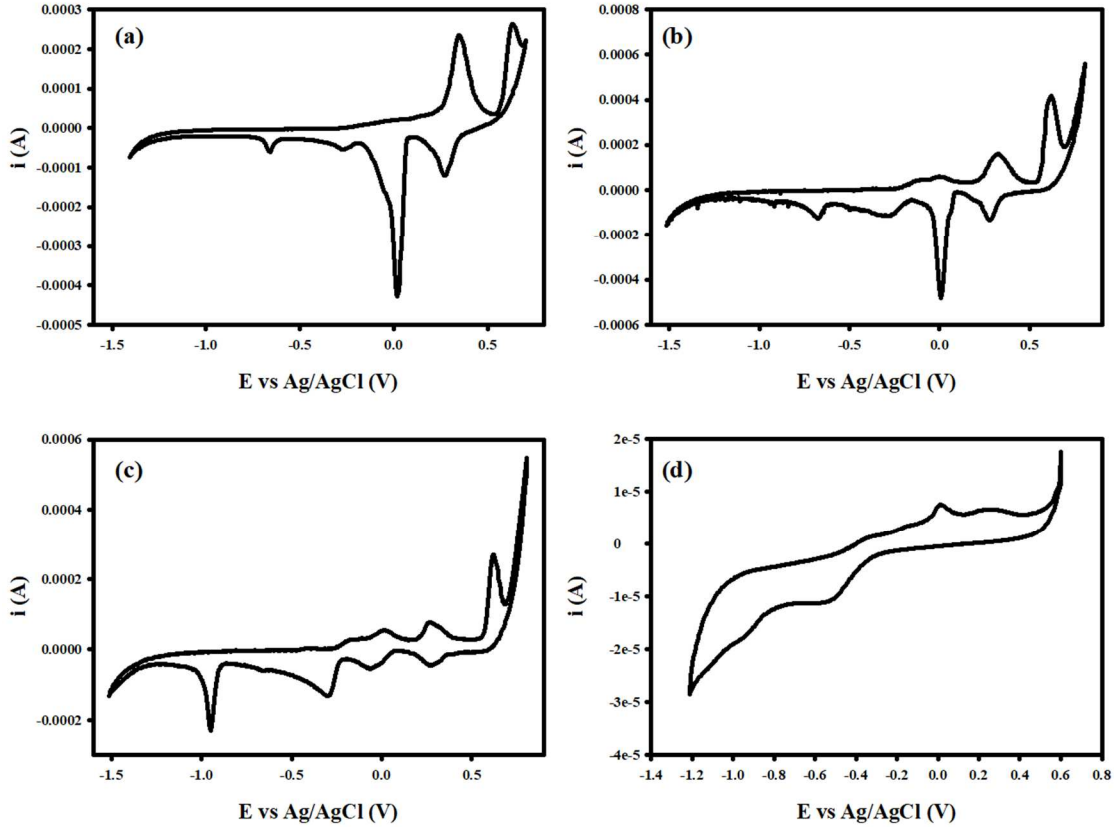

Figure S6. Cyclic voltammograms of 1-hexanethiol functionalized Ag:Cu 3:1 (a), 2:1 (b), 1:2 (c), and 1:3 (d), alloy nanoparticles performed in an aqueous 0.1 M NaOH solution at a scan rate of 10 mV/s.

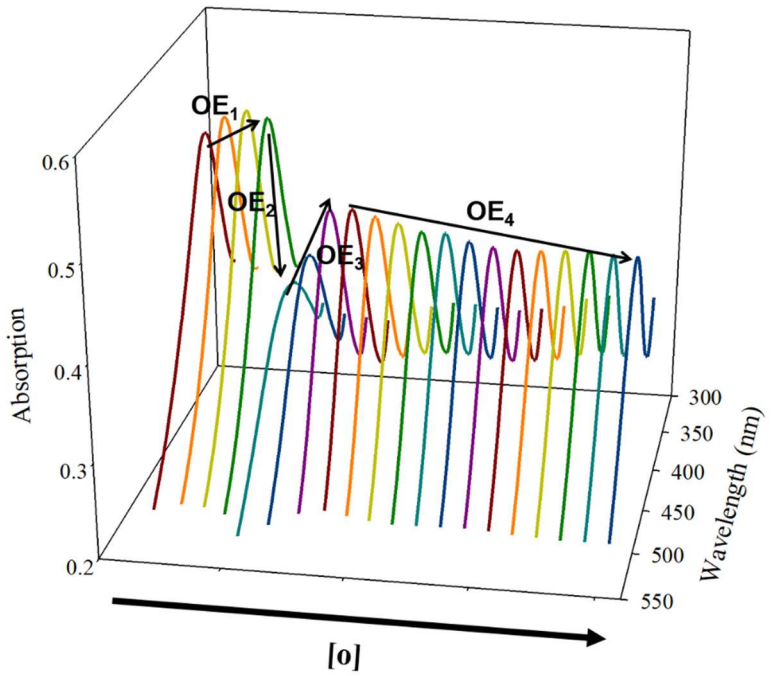

Figure S7. Zoomed-in, UV-vis spectra of AgCu nanoparticle solution over the course of oxidation with arrows distinguishing discrete oxidation events which are labeled in order of occurrence.

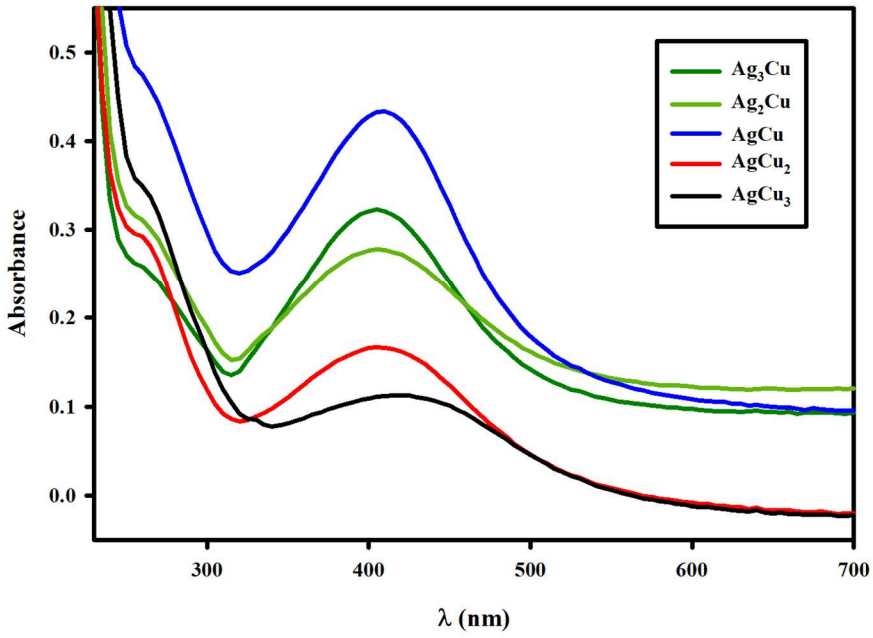

Figure S8. UV-vis spectra of AgCu alloy nanoparticle solutions after oxidation experiment.

Table S1. Volumes of AgCu alloys, nanopure H_2O, luria broth, and *E. coli* suspension with resulting total nanoparticle concentration for a typical 96-well plate growth experiment.

	V_{AgCu} (µL)	V_{H_20} (µL)	V_{LB} (µL)	$V_{E.coli}$ (µL)	[AgCu] (µM)
A	20	140	20	20	10
B	18	142	20	20	9
C	16	144	20	20	8
D	14	146	20	20	7
E	12	148	20	20	6
F	10	150	20	20	5
G	5	155	20	20	2.5
H	0	160	20	20	0

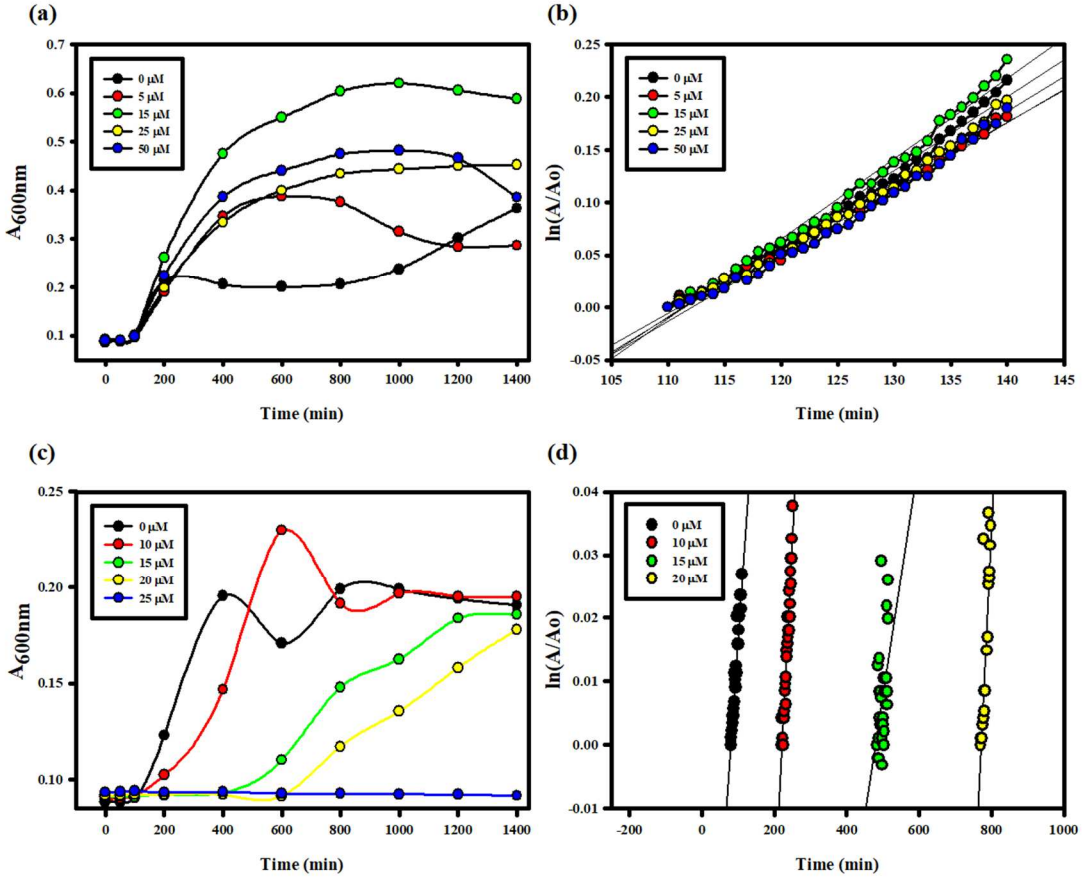

Figure S9. Growth curves of E. coli cultures grown in (a) Cu and (c) Ag nanoparticle solutions of elevated concentration, with corresponding linear regression plots (b,d) over the first 30 minutes of exponential growth used to determine growth rate constants.

Table S2. Summary of Escherichia coli growth rate constants (*k*g) in varying concentrations of AgCu alloy nanoparticle solutions.

	0 µM	**2.5 µM**	**5.0 µM**	**6.0 µM**	**7.0 µM**	**8.0 µM**	**9.0 µM**	**10.0 µM**
Ag	$8.40e^{-4}$	$1.08e^{-3}$	$1.63e^{-3}$	$1.47e^{-3}$	$1.81e^{-3}$	$1.24e^{-3}$	$1.88e^{-3}$	$1.12e^{-3}$
Ag_3Cu	$1.28e^{-3}$	$9.86e^{-4}$	-	-	-	-	-	-
Ag_2Cu	$3.13e^{-3}$	$2.81e^{-3}$	-	-	-	-	-	-
AgCu	$1.69e^{-3}$	$1.37e^{-3}$	-	-	-	-	-	-
$AgCu_2$	$1.39e^{-3}$	$1.04e^{-3}$	$1.80e^{-3}$	$1.55e^{-3}$	-	-	-	-
$AgCu_3$	$1.29e^{-3}$	$9.06e^{-4}$	$1.15e^{-3}$	$2.32e^{-4}$	$5.92e^{-4}$	-	-	-

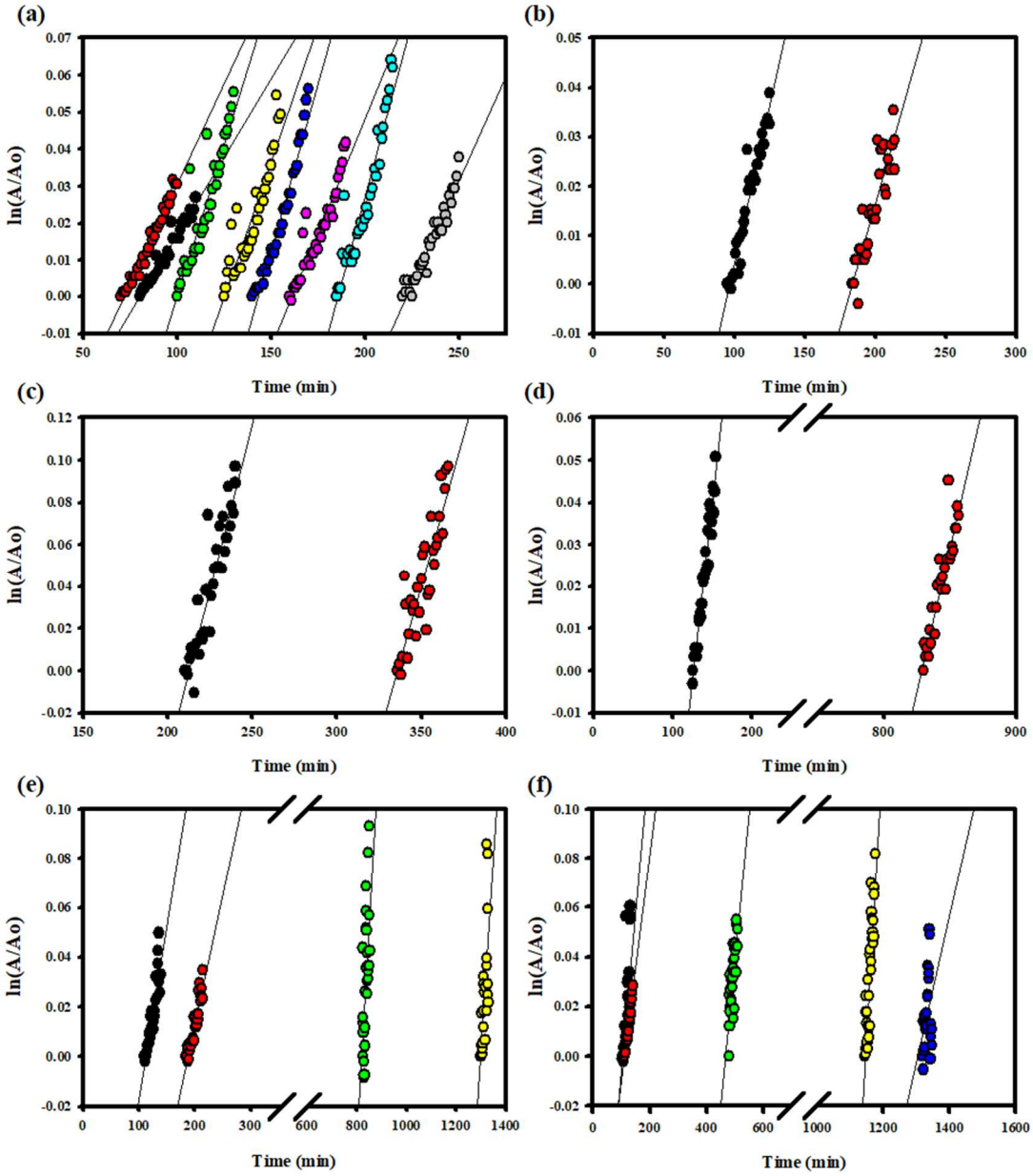

Figure S10. Linear regression plots over the first 30 minutes of exponential growth for E. coli cultures grown in Ag (a), Ag_3Cu (b), Ag_2Cu (c), AgCu (d), $AgCu_2$ (e), and $AgCu_3$ (f) nanoparticle solutions. Black, red, green, yellow, blue, pink, cyan and grey circles correspond to 0.0, 2.5, 5.0, 6.0, and 7.0 μM nanoparticle concentrations respectively.

Table S3. Summary of growth rate constants (kg) and lag phase durations (T_L) for E. coli cultures grown in the presence of elevated concentrations of Cu nanoparticles.

	0 µM	5.0 µM	15.0 µM	25.0 µM	50 µM
k_g (min^{-1})	$6.99e^{-03}$	$6.06e^{-03}$	$7.62e^{-03}$	$6.55e^{-03}$	$6.30e^{-03}$
T_L (min)	100	100	100	100	100

Table S4. Summary of growth rate constants (k_g) and lag phase durations (T_L) for E. coli cultures grown in the presence of elevated concentrations of Ag nanoparticles.

	0 µM	10.0 µM	15.0 µM	20.0 µM
k_g (min^{-1})	$8.40e^{-04}$	$1.12e^{-3}$	$3.74e^{-04}$	$1.21e^{-03}$
T_L (min)	80	220	485	770

2.6 References

(1) Russell, A.; Hugo, W. *Progress in Medicinal Chemistry* **1994**, *31*, 351–370.
(2) Dupont, C. L.; Grass, G.; Rensing, C. *Metallomics* **2011**, *3* (11), 1109.
(3) Pearson, R. G. *Journal of the American Chemical Society* **1963**, *85* (22), 3533–3539.
(4) Liau, S.; Read, D.; Pugh, W.; Furr, J.; Russell, A. *Letters in Applied Microbiology* **1997**, *25* (4), 279–283.
(5) Macomber, L.; Imlay, J. A. *Proceedings of the National Academy of Sciences* **2009**, *106* (20), 8344–8349.
(6) Holt, K. B.; Bard, A. J. *Biochemistry* **2005**, *44* (39), 13214–13223.
(7) Friedrich, T. *Biochimica et Biophysica Acta (BBA) - Bioenergetics* **1998**, *1364* (2), 134–146.
(8) Cecchini, G.; Schröder, I.; Gunsalus, R. P.; Maklashina, E. *Biochimica et Biophysica Acta (BBA) - Bioenergetics* **2002**, *1553* (1-2), 140–157.
(9) Brown, O.; Smykrandall, E.; Draczynskalusiak, B.; Fee, J. *Archives of Biochemistry and Biophysics* **1995**, *319* (1), 10–22.
(10) Haber, F.; Weiss, J. *Proceedings of the Royal Society A: Mathematical, Physical and Engineering Sciences* **1934**, *147* (861), 332–351.
(11) Baxendale, J. H.; Evans, M. G.; Park, C. S. *Transactions of the Faraday Society* **1946**, *42*, 155.
(12) Stohs, S. *Free Radical Biology and Medicine* **1995**, *18* (2), 321–336.
(13) Cabiscol, E.; Tamarit, J.; Ros*, J. Int Microbiol* **2000**, *3*(1), 3-8.
(14) Wilks, J. C.; Slonczewski, J. L. *Journal of Bacteriology* **2007**, *189* (15), 5601–5607.
(15) Maurer, L. M.; Yohannes, E.; Bondurant, S. S.; Radmacher, M.; Slonczewski, J. L. *Journal of Bacteriology* **2005**, *187* (1), 304–319.

(16) Goldstein, S.; Meyerstein, D.; Czapski, G. *Free Radical Biology and Medicine* **1993**, *15* (4), 435–445.
(17) Grass, G.; Rensing, C.; Solioz, M. *Applied and Environmental Microbiology* **2011**, *77* (5), 1541–1547.
(18) Santo, C. E.; Taudte, N.; Nies, D. H.; Grass, G. *Applied and Environmental Microbiology* **2008**, *74* (4), 977–986.
(19) Park, H.-J.; Kim, J. Y.; Kim, J.; Lee, J.-H.; Hahn, J.-S.; Gu, M. B.; Yoon, J. *Water Research* **2009**, *43* (4), 1027–1032.
(20) Djoko, K. Y.; Mcewan, A. G. *ACS Chemical Biology* **2013**, *8* (10), 2217–2223.
(21) Panek, H. R.; Obrian, M. R. *Journal of Bacteriology* **2004**, *186* (23), 7874–7880.
(22) Kim, J. S.; Kuk, E.; Yu, K. N.; Kim, J.-H.; Park, S. J.; Lee, H. J.; Kim, S. H.; Park, Y. K.; Park, Y. H.; Hwang, C.-Y.; Kim, Y.-K.; Lee, Y.-S.; Jeong, D. H.; Cho, M.-H. *Nanomedicine: Nanotechnology, Biology and Medicine* **2007**, *3* (1), 95–101.
(23) Sondi, I. *Journal of Colloid and Interface Science* **2004**, *275* (1), 177–182.
(24) Das, R.; Gang, S.; Nath, S. S.; Bhattacharjee, R. *Journal of Bionanoscience* **2010**, *4* (1), 82–86.
(25) Ramyadevi, J.; Jeyasubramanian, K.; Marikani, A.; Rajakumar, G.; Rahuman, A. A. *Materials Letters* **2012**, *71*, 114–116.
(26) Ruparelia, J. P.; Chatterjee, A. K.; Duttagupta, S. P.; Mukherji, S. *Acta Biomaterialia* **2008**, *4* (3), 707–716.
(27) Ren, G.; Hu, D.; Cheng, E. W.; Vargas-Reus, M. A.; Reip, P.; Allaker, R. P. *International Journal of Antimicrobial Agents* **2009**, *33* (6), 587–590.
(28) Azam, A.; Ahmed; Oves; Khan; Habib; Memic, A. *International Journal of Nanomedicine* **2012**, 6003.
(29) Vargas-Reus, M. A.; Memarzadeh, K.; Huang, J.; Ren, G. G.; Allaker, R. P. *International Journal of Antimicrobial Agents* **2012**, *40* (2), 135–139.
(30) Kim, J. H.; Ehrman, S. H.; Germer, T. A. *Applied Physics Letters* **2004**, *84* (8), 1278–1280.
(31) Jia, B.; Mei, Y.; Cheng, L.; Zhou, J.; Zhang, L. *ACS Applied Materials & Interfaces* **2012**, *4* (6), 2897–2902.
(32) Cioffi, N.; Torsi, L.; Ditaranto, N.; Tantillo, G.; Ghibelli, L.; Sabbatini, L.; Bleve-Zacheo, T.; Dalessio, M.; Zambonin, P. G.; Traversa, E. *Chemistry of Materials* **2005**, *17* (21), 5255–5262.
(33) Besner, S. C. C.; Meunier, M. *The Journal of Physical Chemistry C* **2010**, *114* (23), 10403–10409.
(34) Tsuji, M.; Hikino, S.; Tanabe, R.; Matsunaga, M.; Sano, Y. *CrystEngComm* **2010**, *12* (11), 3900.
(35) Firmansyah, D. A.; Kim, T.; Kim, S.; Sullivan, K.; Zachariah, M. R.; Lee, D. *Langmuir* **2009**, *25* (12), 7063–7071.

(36) Peng, H.; Qi, W.; Li, S.; Ji, W. *The Journal of Physical Chemistry C* **2015**, *119* (4), 2186–2195.
(37) Pellarin, M.; Issa, I.; Langlois, C.; Lebeault, M.-A.; Ramade, J.; Lermé, J.; Broyer, M.; Cottancin, E. *The Journal of Physical Chemistry C* **2015**, *119* (9), 5002–5012.
(38) Lisiecki, I.; Pileni, M. P. *The Journal of Physical Chemistry* **1995**, *99* (14), 5077–5082.
(39) Wei, W.; Lu, Y.; Chen, W.; Chen, S. *Journal of the American Chemical Society* **2011**, *133* (7), 2060–2063.
(40) Ehrenreich, H.; Philipp, H. R. *Physical Review* **1962**, *128* (4), 1622–1629.
(41) Cao, H.; Chen, Z.; Zheng, H.; Huang, Y. *Biosensors and Bioelectronics* **2014**, *62*, 189–195.
(42) Henglein, A.; Giersig, M. *The Journal of Physical Chemistry B* **1999**, *103* (44), 9533–9539.
(43) Mulvaney, P. *Langmuir* **1996**, *12* (3), 788–800.
(44) Pakiari, A. H.; Jamshidi, Z. *The Journal of Physical Chemistry A* **2010**, *114* (34), 9212–9221.
(45) Henglein, A.; Mulvaney, P.; Holzwarth, A.; Sosebee, T. E.; Fojtik, A. *Berichte der Bunsengesellschaft für physikalische Chemie* **1992**, *96* (6), 754–759.
(46) Fauth, K.; Kreibig, U.; Schmid, G. *Zeitschrift fur Physik D Atoms, Molecules and Clusters* **1991**, *20* (1-4), 297–300.
(47) Kong, H.; Jang, J. *Chemical Communications* **2006**, No. 28, 3010.
(48) Pol, V. G.; Srivastava, D. N.; Palchik, O.; Palchik, V.; Slifkin, M. A.; Weiss, A. M.; Gedanken, A. *Langmuir* **2002**, *18* (8), 3352–3357.
(49) Sun, X.; Dong, S.; Wang, E. *Macromolecules* **2004**, *37* (19), 7105–7108.
(50) Hostetler, M. J.; Zhong, C.-J.; Yen, B. K. H.; Anderegg, J.; Gross, S. M.; Evans, N. D.; Porter, M.; Murray, R. W. *Journal of the American Chemical Society* **1998**, *120* (36), 9396–9397.
(51) Ang, T. P.; Chin, W. S. *The Journal of Physical Chemistry B* **2005**, *109* (47), 22228–22236.
(52) Laibinis, P. E.; Whitesides, G. M.; Allara, D. L.; Tao, Y. T.; Parikh, A. N.; Nuzzo, R. G. *Journal of the American Chemical Society* **1991**, *113* (19), 7152–7167.
(53) Laibinis, P. E.; Whitesides, G. M. *Journal of the American Chemical Society* **1992**, *114* (23), 9022–9028.
(54) Mcintyre, N. S.; Cook, M. G. *Analytical Chemistry* **1975**, *47* (13), 2208–2213.
(55) Ang, T. P.; Wee, T. S. A.; Chin, W. S. *The Journal of Physical Chemistry B* **2004**, *108* (30), 11001–11010.
(56) Larson, P. E. *Journal of Electron Spectroscopy and Related Phenomena* **1974**, *4* (3), 213–218.

(57) Rehim, S. S. A. E.; Hassan, H. H.; Ibrahim, M. A. M.; Amin, M. A. *Monatshefte für Chemie / Chemical Monthly* **1998**, *129* (11), 1103–1117.
(58) Reyter, D.; Odziemkowski, M.; Bélanger Daniel; Roué Lionel. *Journal of The Electrochemical Society* **2007**, *154* (8), K36–K44.
(59) Chatterjee, K.; Banerjee, S.; Chakravorty, D. *Physical Review B* **2002**, *66* (8).
(60) Mishra, G.; Singh, D.; Yadawa, P. K.; Verma, S. K.; Yadav, R. R. *Platinum Metals Review* **2013**, *57* (3), 186–191.
(61) Kelly, K. L.; Coronado, E.; Zhao, L. L.; Schatz, G. C. *The Journal of Physical Chemistry B* **2003**, *107* (3), 668–677.
(62) Mempin, R.; Tran, H.; Chen, C.; Gong, H.; Ho, K. K.; Lu, S. *BMC Microbiology* **2013**, *13* (1), 301.
(63) Junkins, A. D.; Doyle, M. P. *Current Microbiology* **1992**, *25* (1), 9–17
(64) Sezonov, G.; Joseleau-Petit, D.; Dari, R. *Journal of Bacteriology* **2007**, *189* (23), 8746–8749.
(65) Rensing, C.; Fan, B.; Sharma, R.; Mitra, B.; Rosen, B. P. *Proceedings of the National Academy of Sciences* **2000**, *97* (2), 652–656.
(66) Agnihotri, S.; Mukherji, S.; Mukherji, S. *RSC Adv.* **2014**, *4* (8), 3974–3983
(67) Lu, Z.; Rong, K.; Li, J.; Yang, H.; Chen, R. *Journal of Materials Science: Materials in Medicine* **2013**, *24* (6), 1465–1471.
(68) Martínez-Castañón, G. A.; Niño-Martínez, N.; Martínez-Gutierrez, F.; Martínez-Mendoza, J. R.; Ruiz, F. *Journal of Nanoparticle Research* **2008**, *10* (8), 1343–1348.
(69) Pal, S.; Tak, Y. K.; Song, J. M. *Applied and Environmental Microbiology* **2007**, *73* (6), 1712–1720.
(70) Morones, J. R.; Elechiguerra, J. L.; Camacho, A.; Holt, K.; Kouri, J. B.; Ramírez, J. T.; Yacaman, M. J. *Nanotechnology* **2005**, *16* (10), 2346–2353.
(71) Taner, M.; Sayar, N.; Yulug, I. G.; Suzer, S. *Journal of Materials Chemistry* **2011**, *21* (35), 13150.
(72) Valodkar, M.; Modi, S.; Pal, A.; Thakore, S. *Materials Research Bulletin* **2011**, *46* (3), 384–389.
(73) Nielsen, K. M.; Johnsen, P. J.; Bensasson, D.; Daffonchio, D. *Environmental Biosafety Research* **2007**, *6* (1-2), 37–53.
(74) Palmen, R.; Hellingwerf, K. J. *Current Microbiology* **1995**, *30* (1), 7–10.
(75) Cabral, J. *FEMS Microbiology Letters* **1990**, *72* (1-2), 109–112.
(76) González-Flecha, B.; Demple, B. *Journal of Biological Chemistry* **1995**, *270* (23), 13681–13687.
(77) Yamane, T.; Davidson, N. *Biochimica et Biophysica Acta* **1962**, *55* (5), 609–621.
(78) Buettner, G. R. *Free Radical Biology and Medicine* **1987**, *3* (4), 259–303.
(79) Pou, S.; Ramos, C.; Gladwell, T.; Renks, E.; Centra, M.; Young, D.; Cohen, M.; Rosen, G. *Analytical Biochemistry* **1994**, *217* (1), 76–83.

Chapter 3: Cytotoxicity and Phototoxicity of Graphene Oxide Quantum Dots

3.1 Abstract

Graphene oxide quantum dots (GOQD) and a sodium borohydride-reduced derivative (rGOQD) were synthesized and their antibacterial activity in both dark and under light irradiation were investigated. HRTEM micrographs showed that the resulting nanostructures had an average diameter of 7.1 ± 0.3 nm and UV-vis spectra displayed typical absorption features of graphitic nanoparticles at 230 nm and 260 nm, with the ladder becoming enhanced after reduction. Photoluminescence measurements revealed fluorescence spectra typical of graphitic structures, which blue-shifted and increased in intensity after reduction by sodium borohydride. These structures were also characterized by Raman spectroscopy, and demonstrated characteristic D and G bands with a decrease in the D to G ratio after reduction. *Escherichia coli* cells were incubated with GOQD and rGOQD solutions, and toxicity was evaluated in dark conditions, as well as under visible light irradiation. As-prepared GOQD demonstrated apparent toxicity in the dark, likely due to redox-active phenanthroline moieties. Under light irradiation, only rGOQD demonstrated phototoxicity, likely due to removal of exciton trap states after reduction which is supported by a longer excited state lifetime as measure by fluorescence lifetime measurements. A possible correlation between the chemical structure of graphitic

nanostructures and their toxicity towards bacterial cells is established, and can be extended to all carbon nanostructures.

3.2 Introduction

Graphene is currently the subject of intense research due to the unique optical, electronic, and mechanical properties that result from its two-dimensional sp^2 hybridized carbon structure. Recently, there has been particular interest in using graphene nanomaterials for biomedical applications, such as drug delivery, sensing, tissue regeneration, and cancer therapy.[1–7] As graphene nanostructures have been found to exhibit limited toxicity towards eukaryotic cells, the utilization of graphene derivatives for biological applications has been attracting significant attention from the scientific community.[8–12] A particularly alarming issue in world health today is the rise and prevalence of antibiotic-resistant bacteria, which significantly increases death rates and costs of treatment. According to the World Health Organization, many countries around the world have observed last-resort antibiotics to be ineffective in over half of patients afflicted by common pathogenic bacteria such as *Escherichia coli* and *Klebsiella pneumoniae*. Even more alarming is the prevalence of antibiotic-resistant bacteria in countries with advanced medical facilities such as the United States, where, according to the CDC, over 2 million people become infected by these resistant pathogens leading to over 23,000 deaths annually. Therefore, it is imperative that as these antibiotic-resistant bacteria evolve, so must the medicines that are utilized to treat them. To this end, antibacterial nanostructures have recently gained

serious consideration by the healthcare community.[13,14] The antibacterial applications of graphene-based nanomaterials are still relatively new however. In fact, although there are several excellent reviews that summarize recent progress in the studies of the antimicrobial activity of graphene nanostructures, few discuss the mechanisms of action in detail.[15–20] In order to develop next-generation antimicrobial materials, a comprehensive understanding of the mechanisms of action of graphene nanostructures is desired. Accordingly, mechanistic models have yet to be established, be established. Although a mechanism of action is generally provided in many studies, the experimental evidence substantiating most claims is generally limited. The most commonly proposed mechanisms of action fall under four categories: (a) oxidative stress induction,[21–23] (b) protein dysfunction,[24,25] (c) membrane damage,[23,26,27] and (d) transcriptional arrest.28,29 Independently, these represent unique cellular toxicities with specific biomolecular targets such as iron sulfur clusters, cysteine residues of proteins, membrane lipids, and DNA molecules. However, as biological processes are intricately linked, the exact effects of nanomaterial toxicity are difficult to isolate. Compounding the problem even further, each of these forms of toxicity can independently result in the other three, with the generation of reactive oxygen species (ROS) being the most commonly reported outcome. It is understandable then that the exact mechanism of graphene nanostructure cytotoxicity is obscure, resulting in largely speculative claims based on indirect evidence. As in vitro experiments such as glutathione (GSH) oxidation and ROS-generation assays are utilized to provide evidence for a specific mechanism of

action, the cytotoxic effects of these nanomaterials inside bacterial cells are typically oversimplified.[30–35] There is however, good examples of direct evidence for some of these mechanisms, most interestingly, oxidative stress. One noteworthy example of direct evidence that graphene nanomaterials are indeed Fenton-active, is given by Zhao *et al.*[36] who characterized the Fenton-like catalytic degradation of Orange II in the presence of H_2O_2 with graphene oxide (GO) and hydrogen-reduced graphene oxide (hrGO) nanosheets. The oxidation of Orange II was found to be much less efficient with GO than with hrGO, which the authors attributed to the increasing number of defects in the sp^2 domains produced by hydrogenation. This study suggests that there is a structural correlation between graphene nanomaterials and their redox activity, which supports the notion that direct generation of ROS via redox chemistry is indeed one of the mechanisms of cytotoxicity exhibited by graphene materials. Liu *et al.*[34] reached similar conclusions in their study of carbon nanomaterial reactivity towards molecular oxygen. Their results demonstrated that oxygen adsorbed on the surface of graphene primarily at defect sites, formed superoxide intermediates (e.g., $O2^{\bullet-}$ and $HO^{\bullet}_2$) which subsequently oxidized cellular GSH and released the bound superoxide species into the environment. The proposed reaction mechanism is supported by experimental and theoretical evidence.[37,38] This provides further evidence for a semi-stepwise mechanism for ROS generation on graphene surfaces. Other groups claim that charge transfer between graphene derivatives and redox-active species other than H_2O_2 is responsible for the generation of ROS. For instance, Li *et al.*[21] provided noteworthy evidence for this charge transfer mechanism by

varying the conductive nature of the substrate onto which a graphene film was deposited and comparing the bactericidal effects. Interestingly, the antibacterial activity exhibited clear dependence on the conductivity of the graphene–metal substrates, with the inhibition of S. aureus and *E. coli* growth increasing in the order of graphene/SiO2 < graphene/Ge < graphene/Cu. They proposed that respiratory chain electrons were extracted from the electron transport chain (ETC) by graphene through a charge transfer mechanism, and only when a substrate with a vacant energy state below the Fermi level of graphene was utilized, could the extracted electrons be transferred from the graphene to the circuit and cause cytotoxicity. As adenosine triphosphate (ATP), the molecule which provides the energy required for many cellular processes via hydrolysis of the phosphate groups, is synthesized using the energy of H^+ ions moving down the electrochemical gradient created by the redox reactions of the ETC. Extraction of these mobile electrons causes a depletion of intracellular ATP, leading to cell death. The ROS species produced from graphene and its derivatives are therefore considered to be generated through interaction with oxygen or other ETC carriers (e.g., NADH, NADPH, or $FADH_2$). As these biomolecules span a large range of electrochemical potentials, charge transfer reactions with graphene derivatives are likely to occur in the proximity of cellular membranes.[39] Further evidence as to the nature of this charge-transfer process will need to be acquired in order to establish a structure-function relationship between graphene family nanostructures and their cytotoxic structural motifs. This study aims

to address this by relating the cytotoxicity of small, highly uniform graphene oxide nanostructures to their chemical structure.

3.3 Experimental

3.3.1 Synthesis of Graphene Oxide Quantum Dots

An established[40], top-down approach was utilized to synthesize as-prepared GOQDs. In brief, 1g of commercially available carbon pitch fiber was added to a 500 mL, two-neck, round-bottom flask along with 60 mL sulfuric acid, and 40 mL nitric acid. The resulting mixture was first sonicated for 4 hours, then refluxed at 125 °C for 16 hours. After the reaction was complete, the GQD solution was neutralized by adding a saturated solution of sodium hydroxide. The final, neutralized solution was dialyzed (AMW 2000 Da) for approximately 72 hours in nanopure water with frequent changes of water. The purified GOQDs were then concentrated by rotary evaporator, and placed in a vacuum chamber to dry.

3.3.2 Synthesis of Reduced Graphene Oxide Quantum Dots

To synthesize reduced GOQDs (rGOQDs), 100 mg of as-prepared GOQDs were first dissolved in 5 mL of nanopure water, bringing the solution to a final concentration of 20 mg/mL. While stirring at 1000 rpm, 1 g of $NaBH_4$ was added all at once, causing vigorous bubbling of the solution. The reaction was allowed to stir for 5 minutes, then immediately dialyzed for 24 hours with frequent changes of water with the resulting solution being dried in a vacuum to afford rGOQD powder.

3.2.3 Characterization Methods

As-prepared and reduced GOQDs were characterized by UV-visible (UV-vis) absorption spectroscopy using an Agilent Cary 60 UV-vis spectrometer with a 1 cm quartz cuvette, photoluminescence spectroscopy using a PTI photoluminescence spectrometer, and by high resolution transmission electron microscopy (HRTEM) on a Phillips CM300 operating at 300 kV. The average diameter of the resulting structures was obtained by counting over 200 individual particles. Raman spectra were acquired with a DeltaNu Advantage 532 Raman system powered by a 532 nm laser. X-ray photoemission spectra (XPS) were acquired with a PHI 5400/XPS instrument equipped with an Al Kα source operated at 350 W and 10−9 Torr.

3.2.4 Fluorescence Lifetime Measurements

Time-correlated single photon counting (TCSPC) was carried out on a home built apparatus. The excitation source was a pulsed Super K EXTREME (NKT Photonics) supercontinuum laser coupled to a Super K SELECT (NKT Photonics) acousto-optic filter and external RF driver (NKT Photonics) to select the wavelength of the excitation pulse. Measurements were carried out at a 78 MHz pulse repetition rate with 14.2 μW (400 nm) power, as measured near the sample. Both excitation and emission beams were horizontally polarized by mounted Glan-Thompson polarizers (Thorlabs). Emission light was collimated and refocused by a set of achromatic doublets (Thorlabs). Long pass filters were used to minimize the in-fluence of the

reflected excitation beam. Emission wavelengths were selected by an Acton Spectra Pro SP-2300 monochromator (Princeton Instruments), on which
two detectors were mounted for steady-state and time-resolved measurements. An air cooled PIXIS 100 CCD (Princeton Instruments) was used to record the steady-state spectra. A hybrid PMT with minimal after-pulsing (Becker and Hickl) was used to record the time-resolved fluorescence decay. An SPC-130 photon counting module (Becker and Hickl) coupled to a Simple-Tau 130 table-top TCSPC system was used for photon counting. Emitted photons were collected for 5s, and each measurement was repeated 50 times prior to averaging and subsequent analysis.

3.2.5 Cytotoxicity Assays

Escherichia coli (ATCC 25922) cells were obtained by first spreading frozen liquid cultures (20% glycerol, -72 °C) on Luria broth (LB) agar plates and incubating them at 37 °C overnight. From these plates, one individual colony was selected and used to inoculate 3 mL of sterile liquid LB and incubated at 37 °C for 18 h with constant shaking at 250 rpm. Upon completion of this growth period, a 1 mL aliquot of this culture was removed and centrifuged at 5000 rpm for 5 min. The supernatant was discarded, and the pellet re-suspend 1 mL sterile nanopure water. This process was repeated once, and enough of the second re-suspension was added to 5 mL of sterile nanopure water to bring the optical density (O.D.) at 600 nm to 0.100. A 100 µL aliquot of this 0.1 O.D. suspension was added to 1.5 mL centrifuge tubes containing 990 µL of GOQD and rGOQD solutions, both at 1 mg/mL concentration., as well as 990 µL of nanopore water as a control. A 100 µL aliquot was taken out of

each solution every minute for 4 minutes and spread on fresh luria broth agar plates using silica beads. To characterize the cytotoxicity of GOQD and rGOQD solutions under light irradiation, samples were prepared similarly in 1.5 mL centrifuge tubes, but held 10 cm above a 100 W, L.E.D. array (Hongke Lighting) with a 395-400 nm emission band, and irradiated for 1 minute before plating a 100 μL aliquot on LB agar plates. All plates were incubated for 18 h at 37 °C, after which individual colonies were counted.

3.3 Results and Discussion

3.3.1 Structural Characterizations of Graphene Oxide Quantum Dots

The GOQD nanostructures resulting from the acidic exfoliation of carbon pitch fibers were examined by high-resolution transmission electron microscopy (HRTEM) and, as seen in **Figure 1a**, had plate-like morphologies with an average reveals their lattice spacing to be 0.35-0.37 nm, characteristic of graphene oxide.[41] The optical properties of these GOQD and sodium borohydride-reduced derivative (rGOQD) were first analyzed by UV-visible spectroscopy (**Figure 2**), which revealed diameter of 7.1 ± 0.3 nm. A close-up micrograph (**Figure 1b**) of these quantum dots a typical Mie scattering profile with peaks at 230 nm corresponding to C=C $\pi \rightarrow \pi^*$ transitions originating from the sp^2 domains of the graphitic structure, and a shoulder

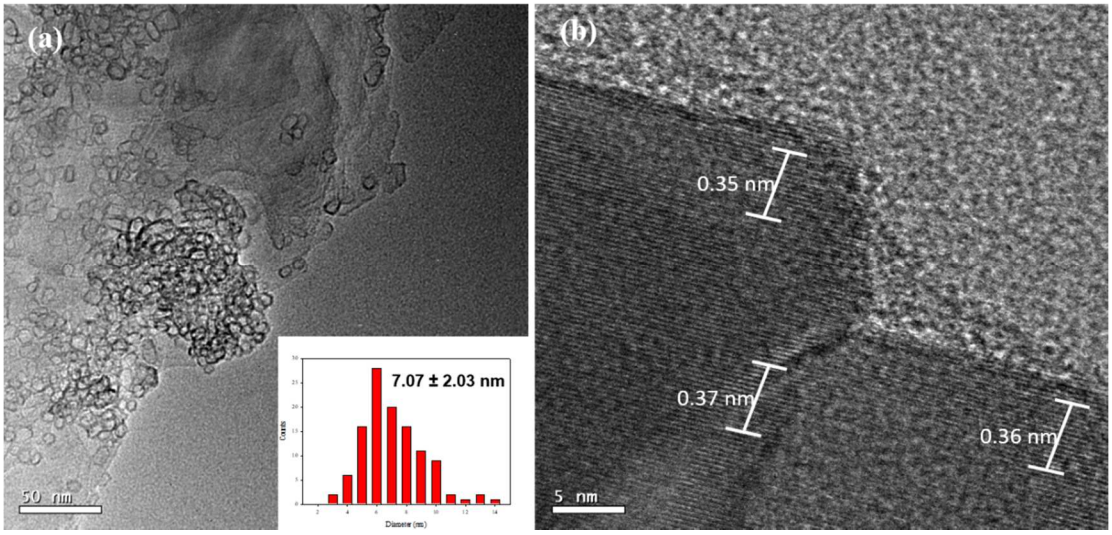

Figure 1. HRTEM micrographs of GOQD structures. A representative population is shown in (a) with a size-distribution histogram and average diameter in the inset. A zoomed-in micrograph with measured lattice spacings of one individual GOQD nanostructure is shown in (b).

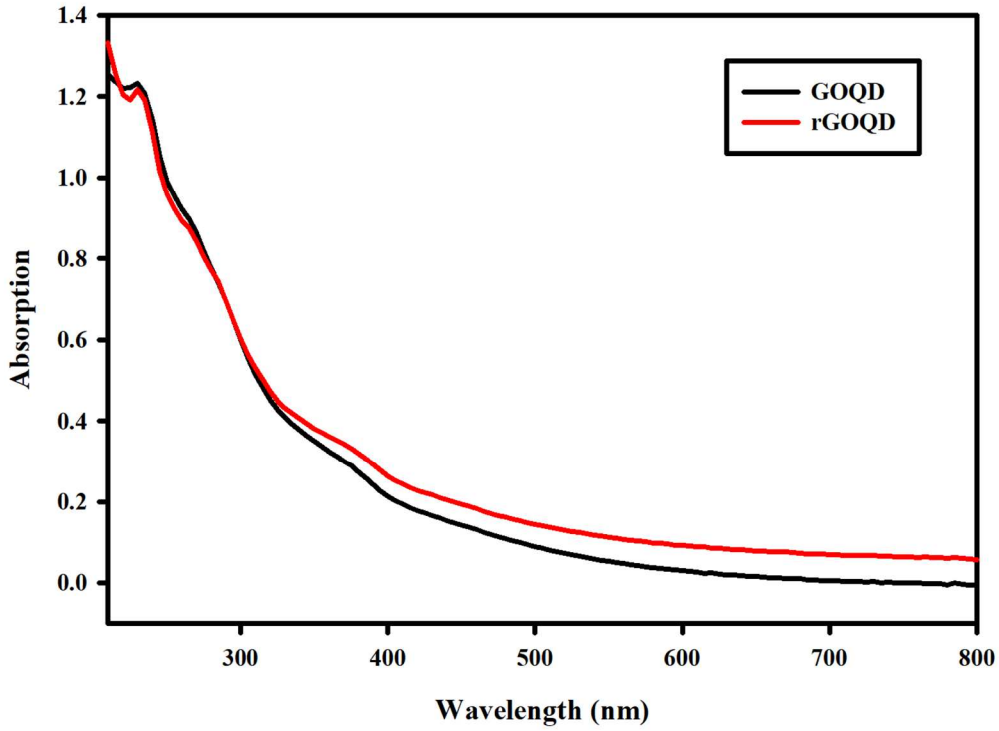

Figure 2. UV-vis spectra of GOQD and rGOQD solutions.

at 260 nm indicative of larger sp^2 domains, as well as a broad shoulder at around 360 nm corresponding to $n \rightarrow \pi^*$ transitions of C=O moieties in the structure.[42-45] The fluorescence spectra of these structures were also acquired and are shown in **Figure 3**. As-prepared GOQD solutions displayed two excitation bands, centered at 355 and 465 nm, and an emission band centered at 535 nm. Upon reduction, the fluorescence spectra increased markedly in intensity, and the excitation band and the emission

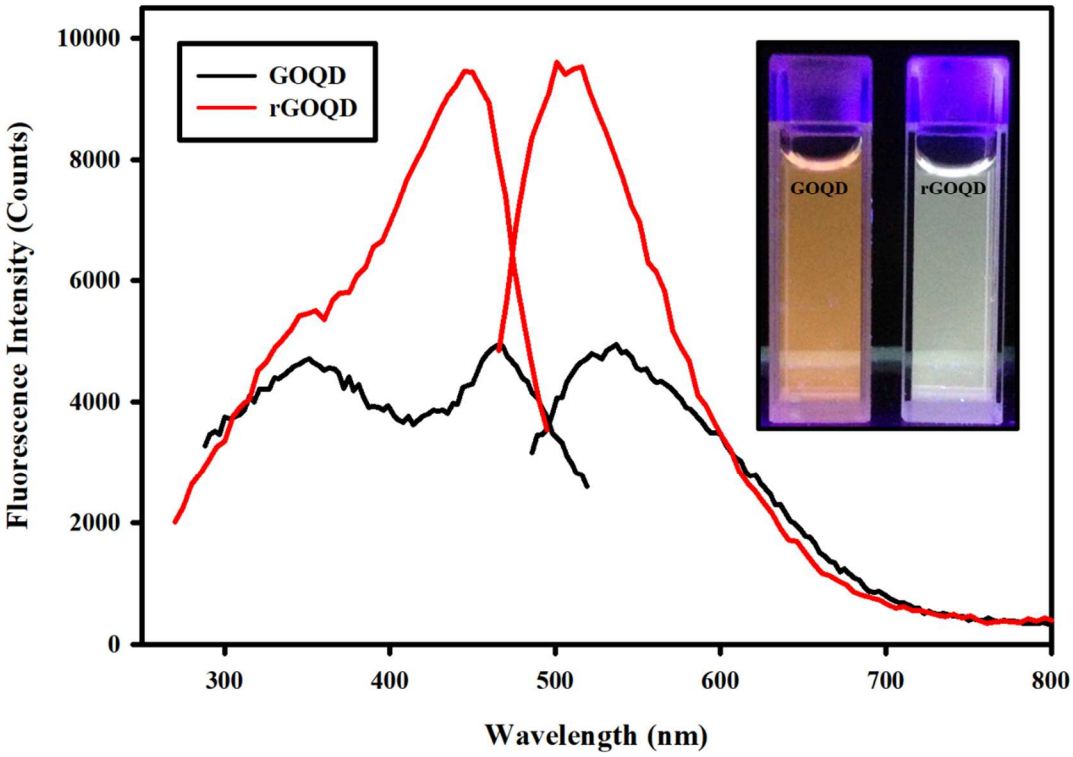

Figure 3. Photoluminescence spectra of GOQD and rGOQD solutions with photograph of these solutions under 365 nm excitation.

band both blue-shift by about 20 nm. These features are likely due to radiative e^- and h^+ recombination, the energy of which is known to be dependent on the size of the

excited sp^2 domain implying that smaller sp^2 domains are present after reduction.[46-47] Borohydride reduction is commonly used to reduced graphene oxide structures, yet the chemical changes due to this reaction are still not clear. To shed light on the fate of these GOQDs after sodium borohydride reduction, the Raman spectra shown in **Figure 4** are considered. The D and G bands for GOQD and rGOQD are highlighted, and both show very similar peak positions, with D and G bands at 1363 cm^{-1} and 1599 cm^{-1} for GOQD, and 1359 cm^{-1} and 1596 cm^{-1} for rGOQD. This slight red-shift has been observed for graphene oxide structures after reduction, and suggests a decrease in average sp^2 domains size in agreement with fluorescence measurements.[48-49] The D to G ratio is typically used a measure in the overall disorder of a graphitic system, and can provide further evidence to the effects of borohydride reduction. GOQD structures have an overall D to G ratio of 1.10, which increases slightly to 1.26 after reduction, indicating an increase in disorder of the carbon structure. These measurements, together with UV-vis and photoluminescence measurements suggest that upon reduction, an increased number of smaller sp^2 carbon domains exist on the GOQD structures. More in-depth characterization of the resulting structure can be obtained by x-ray photoemission (XPS) spectroscopy (**Figure 5**) which will give a more quantitative assessment of the types of carbon present on these surfaces. The C 1s signal is shown in high-resolution, and from peak deconvolution, the composition of the different species of carbon for both GOQD and rGOQD samples can be determined. The first major peak centered at

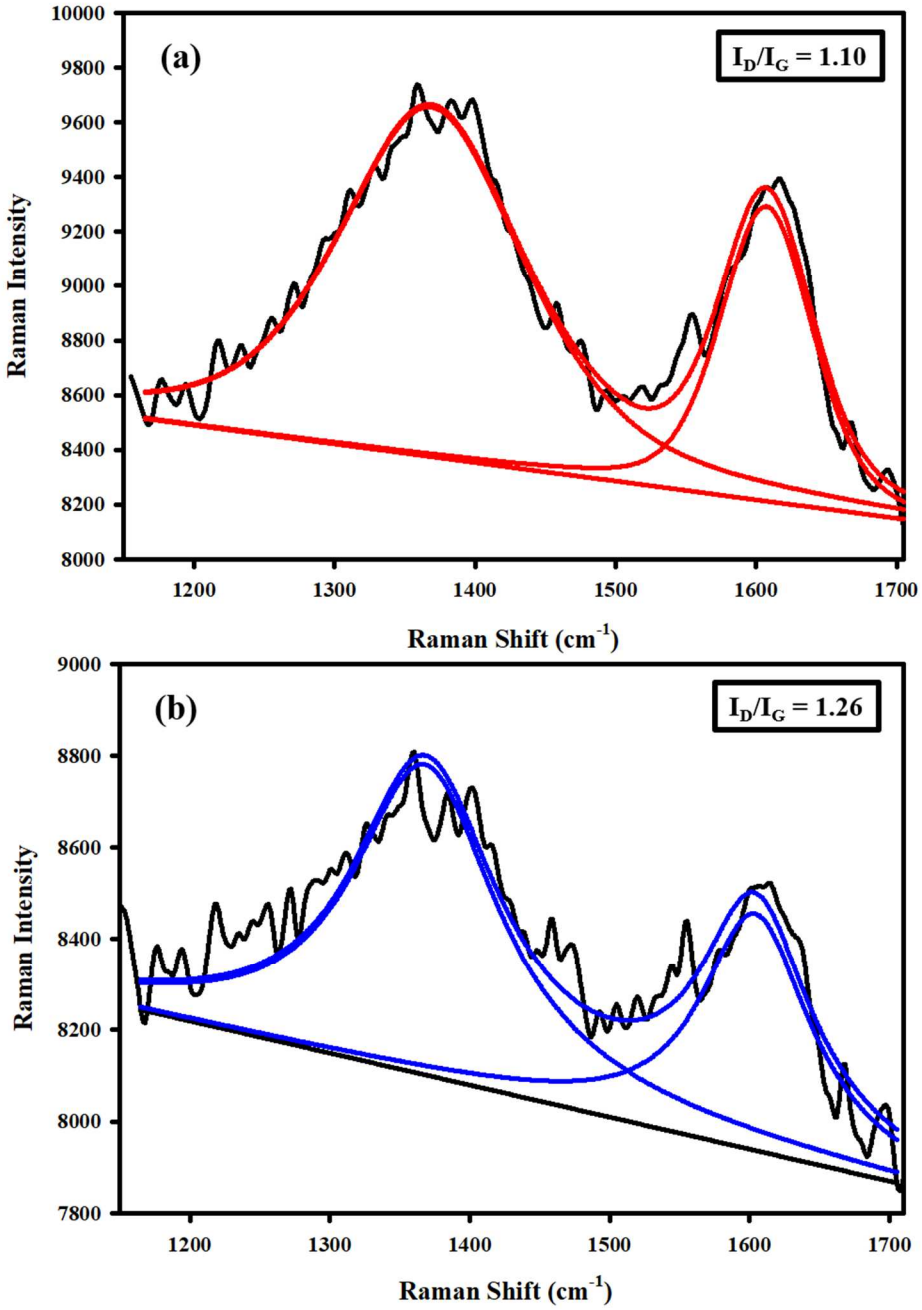

Figure 4. Raman spectra of (a) GOQD and (b) rGOQD samples, highlighting the D and G bands. D to G ratio as calculated peak heights is shown in the upper right corners.

around 283.8 eV corresponds to carbons forming C-H, C-C, and C=C bonds within the structure, the second, at 284.3 eV to carbons with single bonds to oxygen species (C-O, C-O-C), the third at around 285.1 eV to C=O in aldehydes and ketones, and finally the peak at 288.2 eV to carbons which are part of a carboxylic acid bond. The overall composition of these types of carbons for GOQD and rGOQD is summarized in **Table 1**, and indicates a nearly complete loss of aldehyde and ketone species after reduction, with correspondingly significant increase in C-O bonds. These results can

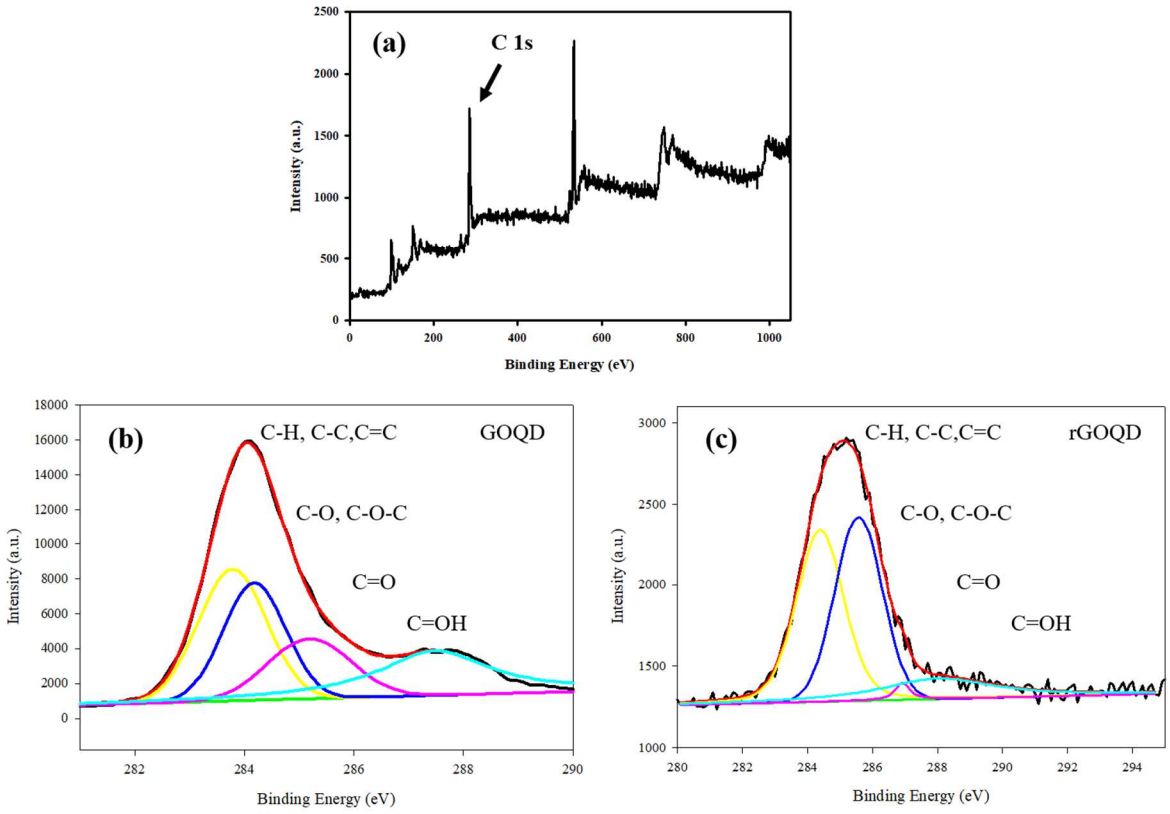

Figure 5. X-ray photoemission spectra of GOQD and rGOQD nanostructures. Panel (a) shows a representative survey spectrum of GOQDs. Panels (b) and (c) show the C 1s spectra in high resolution and with deconvolutions for each type of carbon of GOQDs and rGOQDs nanostructures respectively.

Table 1. Summary of the carbon species composition of GOQDs and rGOQDs calculated from C 1s deconvolution.

Functional Group	GQD Composition (%)	rGOQD Composition (%)
C=C	42	43
C-OH	25	48
C=O	20	2
C=OH	11	7

be explained by considering the reactions of sodium borohydride outlined in **Figure 6**. It is well-established that sodium borohydride can be utilized to reduce aldehydes and ketones to alcohols by the mechanisms illustrated in **Figure 6a** and **b**, which explains the loss of nearly all C=O signals as well as the significant increase of C-O signals in XPS measurements. Additionally, the formation of double bonds by acid-catalyzed elimination reaction is illustrated in **Figure 6d**, providing a plausible mechanism for the formation of small sp^2 domains after reduction as suggested by spectroscopic evidence. Additionally, aromatic carboxylic acids can also be reduced to alcohols by the more complex mechanism outlined in **Figure 6e**, which would

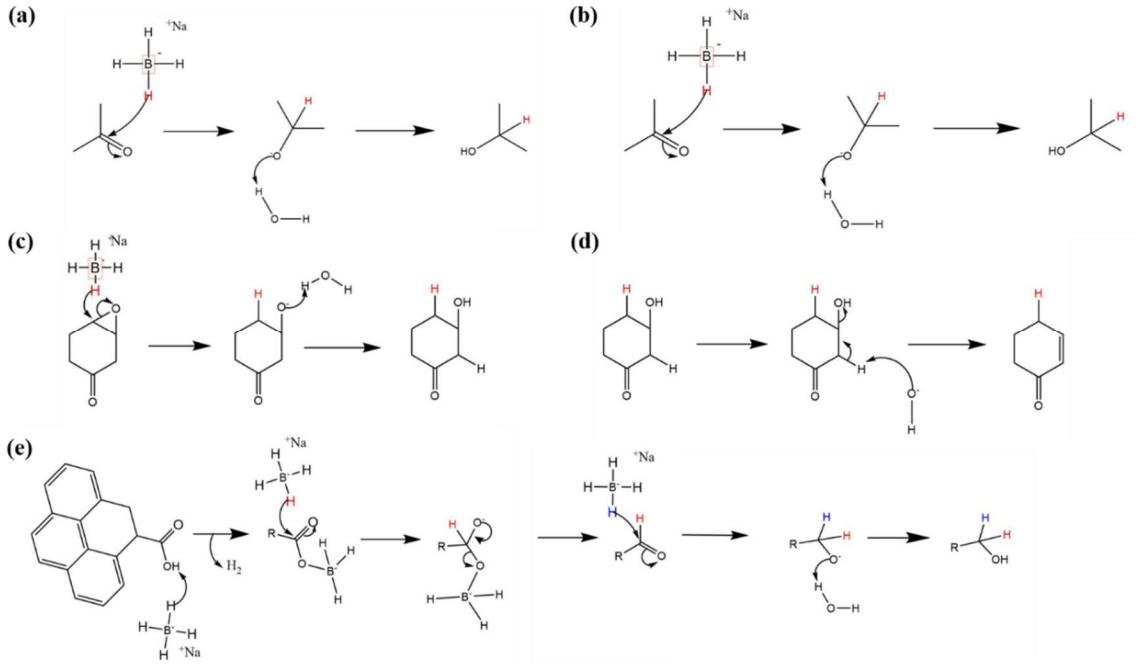

Figure 6. Reaction mechanisms of sodium borohydride relevant to GOQD functional groups. Reduction of (aldehydes (a) and ketones (b). Formation of alcohols from epoxides, (c) elimination of hydroxyl groups to form double-bonds (d), and reduction of aromatic carboxylic acids (d).

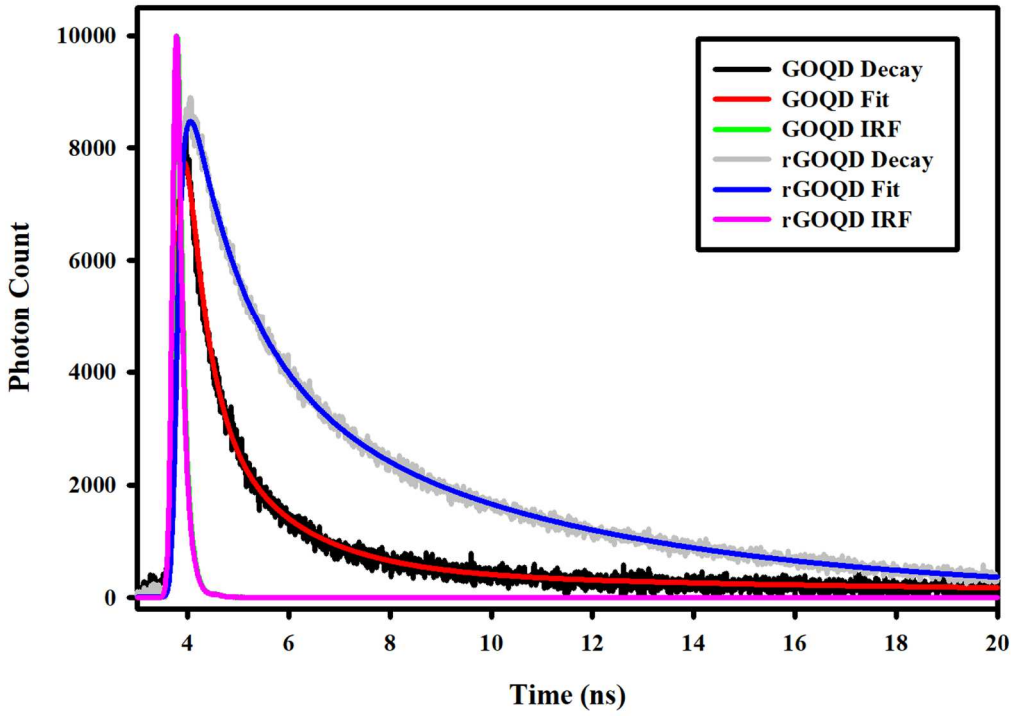

Figure 7. Time-resolved fluorescence decay traces for GOQD and rGOQD samples.

Table 2. Summary of fluorescence lifetimes and % composition of each species derived from tri-exponential fitting results of fluorescent decays shown in Fig. 7.

	τ_1 (ns)	%	τ_2 (ns)	%	τ_3 (ns)	%
GOQD	0.369	99.9	1.62	0.07	6.44	0.002
rGOQD	0.468	97.8	4.81	0.23	1.55	1.9

explain the slight decrease in carboxylic acid composition after reduction. It is also possible however, that the beta carbons of α, β-unsaturated carbonyl compounds can act as electrophiles and be hydrogenated by hydride ions. As β carbons are soft electrophiles and hydride ions relatively soft nucleophiles, it is likely that this

reaction would occur at elevated sodium borohydride concentrations. The GOQD structure has a large number of double-bonded carbons so the likelihood that they are in conjugation with an edge site containing a carbonyl moiety is quite high. Hydrogenation of these double bonds would also result in smaller sp^2 domains and potentially remove the pathway electrons could travel toward a quenching site. In order to shed light on this plausible mechanism, fluorescence lifetime measurements were performed using time-correlated single-photon counting (TCSPC) and used to quantify the fluorescence lifetimes of GOQD and rGOQD species. The resulting fluorescence decay traces taken after irradiation at 400 nm is shown in **Figure 7**, and results summarized in **Table 2**. The results were fitted to a tri-exponential decay, with majority (> 99%) of the charge-carriers contributing to the GOQD decay having a lifetime of 369 ps, a value that increases by about 25% after reduction to 468 ps and remains the dominant contributor to the fluorescence decay. These values agree with that observed for GQD structures in previous studies[50] and suggests that trap states are removed upon reduction of GOQD structures by sodium borohydride, and is likely due to breaking of sp^2-domain conjugation to carbonyl species. These results give further insight as to the nature of borohydride reduction of graphene oxide nanostructures, with potentially significant implications for their bactericidal activities.

3.3.2 Cytotoxicity of Graphene Oxide Quantum Dots

To evaluate the cytotoxicity of GOQD and rGOQD structures towards bacterial cells, freshly grown *E. coli* cells were suspended in GOQD and rGOQD solutions at 1 mg/mL concentrations and viability over time quantified via plate-counting method. Upon addition of these cells to GOQD and rGOQD solutions, the suspension was immediately vortexed and a 100 μL aliquot was spread on a luria broth agar plate using silica beads. This process was repeated every minute for 4 min, and plates were incubated at 37 °C for 18 h before individual colonies were counted. The results are summarized in **Figure 8**, which displays the colony-forming units (CFU) per mL at each time point. As can be seen, a substantial loss in viability is observed for bacteria incubated with GOQD nanostructures, whereas no significant change in the number of colonies was observed for those incubated with rGOQD or with pure water. This result is interesting in that the reduction by sodium borohydride resulted in complete loss of cytotoxicity towards bacterial cells. The reason for this may lie in the chemical functional groups that exist in the GOQD structure before reduction. Tian *et al.* synthesized carbon nanoparticles through a similar method as was utilized in this study, by refluxing candle soot in strong acids to yield highly-luminescent carbon nanoparticles.[51] They further characterized the resulting carbon nanostructures by cyclic voltammetry and found that these carbon nanoparticles demonstrated two redox peaks which were assigned to phenanthroquinone-like moieties. As the synthetic procedure was similar in the preparation of GOQD structures, it is reasonable to expect these species to exist in GOQD structures. The

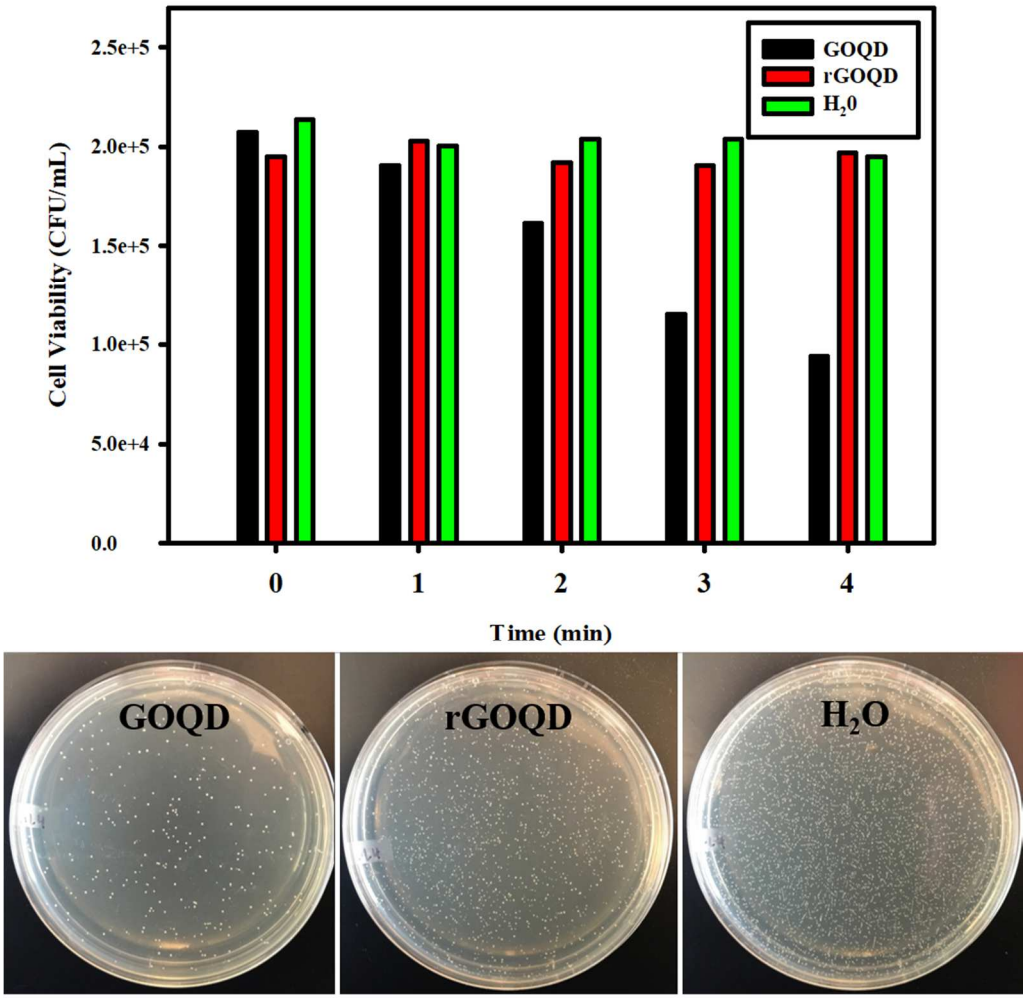

Figure 8. Summary of colony-forming units counted from agar plates inoculated by bacterial cells at increasing incubation time with GOQD, rGOQD, and pure water as a control with photographs of the plates inoculated by bacteria after 3 minutes of incubation.

significance of this is that phenanthroquinone derivatives have been shown to induce cellular toxicity by Rodriguez *et al.* which they attributed to its redox activity.[52] The proposed mechanism of this molecules toxicity toward bacteria is summarized in **Figure 9**, and involves the oxidation of vital electron transport chain (ETC) redox

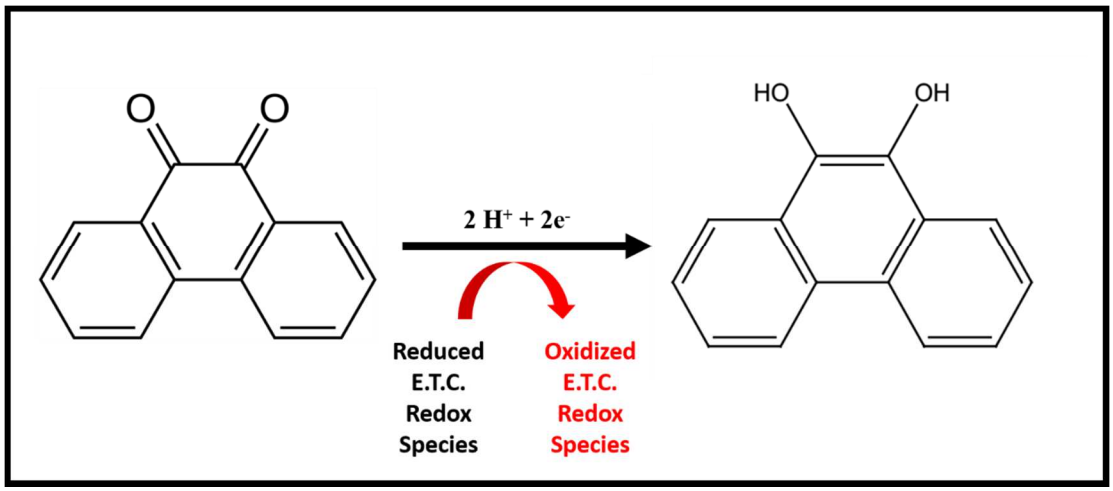

Figure 9. Proposed mechanism of the 9,10 phenanthroquinone moiety cytotoxicity.

mediators, namely, any species with a reduction potential less positive than -0.12 V including $FADH_2$, $FMNH_2$, NADH, and ferridoxins, all of which are critical for propagation of electrons through the ETC and cellular respiration. By reducing the ketone species of these molecules, the oxidative nature of this moiety is lost, and with it, its cytotoxic potential. This explains the lack of cytotoxicity demonstrated by rGOQD structures, and provides a foundation by which to evaluate all carbon nanostructures.

3.3.3 Phototoxicity of Graphene Oxide Quantum Dots

In addition to the plating experiments with GOQD and rGOQD solutions in the dark, separate suspensions prepared similarly were irradiated by an LED array (λ_{em} = 395-400 nm) and plated on LB agar plates immediately following this irradiation period and the results summarized in **Figure 10** below. As clearly seen, significant loss in viability is observed by rGOQD cell suspensions, whereas cells

suspended in GOQD solution observed very minimal loss in viability with colony counts being as high as those from cells suspended and irradiated in pure water.

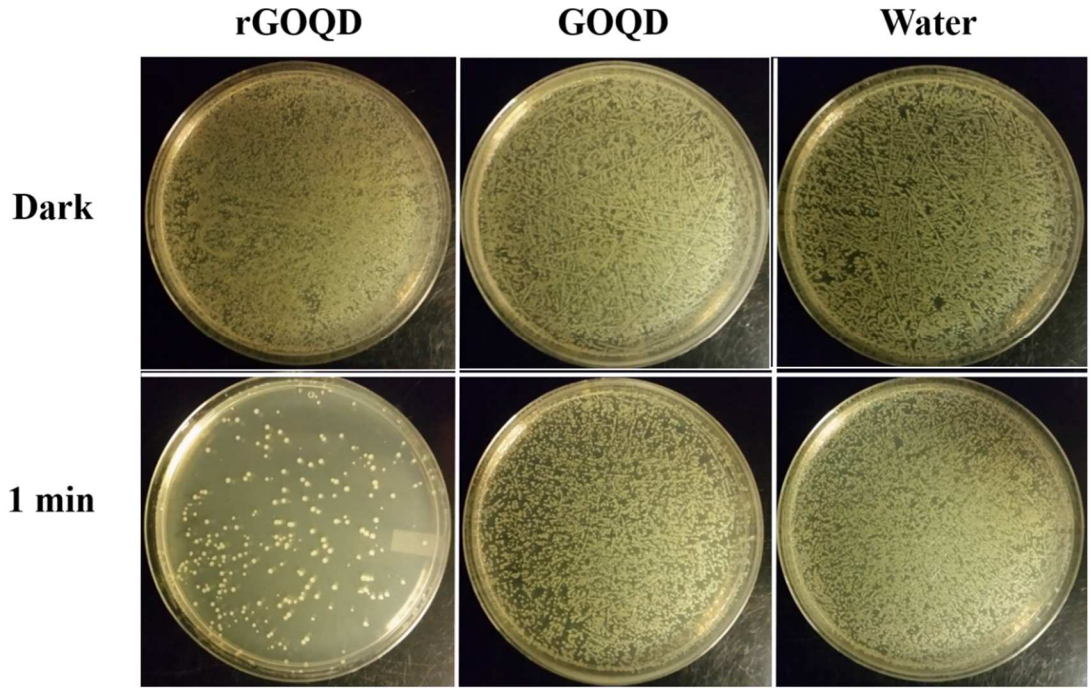

Figure 10. Photographs of LB agar plates inoculated with *E. coli* cell suspensions after 1 minute of irradiation by LED light in the presence of GOQD and rGOQD solutions.

This is likely due to the longer excited-state lifetime exhibited by rGOQD nanostructures as calculated by fluorescence lifetime measurements. By having a longer-live excited state, photo-generated electrons and holes have a higher probability of reacting with species inside bacterial cells, as well as with functional groups on the GOQD and rGOQD surface which could create radical species. Indeed, a study by Hou *et al.* concluded that upon irradiation, carbon-oxygen bonds of hydroxyl functional groups located in the graphene oxide structure are easily cleaved, resulting in hydroxyl radical formation which as detected by EPR.[53] This is likely the

same mechanism of phototoxicty on GOQD and rGOQD structures, with the combination of longer excited-state lifetime and significantly higher hydroxyl group composition affording the marked phototoxicity observed in plate experiments.

3.4 Conclusion

Graphene oxide and reduced graphene oxide quantum dots were synthesized via oxidative acidic exfoliation of carbon pitch fibers, yielding uniform, highly oxidized structures. Upon reduction by sodium borohydride, the fluorescence intensity markedly increases, as does the fluorescence lifetime which is likely due to removal of both functional groups which induced recombination, and conjugated pathways to these recombination sites. The cytotoxicity of these two graphene structures towards bacterial cells was evaluated in dark and light conditions, with GOQDs observing toxicity only in the dark, and rGOQDs only under light irradiation. The former is postulated to be due to phenanthroquinone moieties that are removed upon reduction, and the ladder to longer excited-state lifetime and higher number of hydroxyl groups. These studies provide foundations for graphene family nanostructure toxicity, and can be extended to all carbon nanostructures which will surely be of increasing importance as these nanostructures become increasingly utilized for biomedical applications.

3.6 References

(1) Mao, H. Y.; Laurent, S.; Chen, W.; Akhavan, O.; Imani, M.; Ashkarran, A. A.; Mahmoudi, M. *Chem Rev* **2013**, *113*, 3407-3424.

(2) Liu, J. Q.; Cui, L.; Losic, D. *Acta Biomater* **2013**, *9*, 9243-9257.

(3) McCallion, C.; Burthem, J.; Rees-Unwin, K.; Golovanov, A.; Pluen, A. *Eur J Pharm Biopharm* **2016**, *104*, 235-250.

(4) Lee, J.; Kim, J.; Kim, S.; Min, D. H. *Adv Drug Deliv Rev* **2016**.

(5) Ding, X. L.; Liu, H. F.; Fan, Y. B. *Adv Healthc Mater* **2015**, *4*, 1451-1468.

(6) Patel, S. C.; Lee, S.; Lalwani, G.; Suhrland, C.; Chowdhury, S. M.; Sitharaman, B. *Ther Deliv* **2016**, *7*, 101-16.

(7) Yang, K.; Feng, L.; Liu, Z. *Adv Drug Deliv Rev* **2016**.

(8) Sasidharan, A.; Panchakarla, L. S.; Sadanandan, A. R.; Ashokan, A.; Chandran, P.; Girish, C. M.; Menon, D.; Nair, S. V.; Rao, C. N. R.; Koyakutty, M. *Small* **2012**, *8*, 1251-1263.

(9) Zhang, Y. B.; Ali, S. F.; Dervishi, E.; Xu, Y.; Li, Z. R.; Casciano, D.; Biris, A. S. *Acs Nano* **2010**, *4*, 3181-3186.

(10) Mao, H. Y.; Chen, W.; Laurent, S.; Thirifays, C.; Burtea, C.; Rezaee, F.; Mahmoudi, M. *Colloid Surface B* **2013**, *109*, 212-218.

(11) Duch, M. C.; Budinger, G. R. S.; Liang, Y. T.; Soberanes, S.; Urich, D.; Chiarella, S. E.; Campochiaro, L. A.; Gonzalez, A.; Chandel, N. S.; Hersam, M. C.; Mutlu, G. M. *Nano Lett* **2011**, *11*, 5201-5207.

(12) Barua, S.; Thakur, S.; Aidew, L.; Buragohain, A. K.; Chattopadhyay, P.; Karak,

N. *RSC Advances* **2014**, 4 (19), 9777.

(13) Hajipour, M. J.; Fromm, K. M.; Ashkarran, A. A.; de Aberasturi, D. J.; de Larramendi, I. R.; Rojo, T.; Serpooshan, V.; Parak, W. J.; Mahmoudi, M. *Trends Biotechnol* **2012**, *30*, 499-511.

(14) Moritz, M.; Geszke-Moritz, M. *Chem Eng J* **2013**, *228*, 596-613.

(15) Tegou, E.; Magana, M.; Katsogridaki, A. E.; Ioannidis, A.; Raptis, V.; Jordan, S.; Chatzipanagiotou, S.; Chatzandroulis, S.; Ornelas, C.; Tegos, G. P. *Biomaterials* **2016**, *89*, 38-55.

(16) Ji, H.; Sun, H.; Qu, X. *Adv Drug Deliv Rev* **2016**.

(17) Shi, L.; Chen, J.; Teng, L.; Wang, L.; Zhu, G.; Liu, S.; Luo, Z.; Shi, X.; Wang, Y.; Ren, L. *Small* **2016**, *12*, 4165-84.

(18) Zou, X.; Zhang, L.; Wang, Z.; Luo, Y. *J Am Chem Soc* **2016**, *138*, 2064-77.

(19) Hegab, H. M.; Elmekawy, A.; Zou, L.; Mulcahy, D.; Saint, C. P.; Ginic-

Markovic, M. *Carbon* **2016**, 105, 362–376.

(20) Szunerits, S.; Boukherroub, R. *Journal of Materials Chemistry B* **2016**, 4 (43),

6892–6912.

(21) Li, J. H.; Wang, G.; Zhu, H. Q.; Zhang, M.; Zheng, X. H.; Di, Z. F.; Liu, X. Y.; Wang, X. *Sci Rep-Uk* **2014**, *4*.

(22) Gurunathan, S.; Han, J. W.; Dayem, A. A.; Eppakayala, V.; Kim, J. H. *Int J Nanomedicine* **2012**, *7*, 5901-14.

(23) Krishnamoorthy, K.; Veerapandian, M.; Zhang, L. H.; Yun, K.; Kim, S. J. *J Phys Chem C* **2012**, *116*, 17280-17287.

(24) Akhavan, O.; Choobtashani, M.; Ghaderi, E. *J Phys Chem C* **2012**, *116*, 9653-9659.

(25) Santhosh, C.; Kollu, P.; Doshi, S.; Sharma, M.; Bahadur, D.; Vanchinathan, M. T.; Saravanan, P.; Kim, B. S.; Grace, A. N. *Rsc Adv* **2014**, *4*, 28300-28308.

(26) Liu, S. B.; Hu, M.; Zeng, T. H.; Wu, R.; Jiang, R. R.; Wei, J.; Wang, L.; Kong, J.; Chen, Y. *Langmuir* **2012**, *28*, 12364-12372.

(27) Hui, L.; Piao, J. G.; Auletta, J.; Hu, K.; Zhu, Y.; Meyer, T.; Liu, H.; Yang, L. *ACS Appl Mater Interfaces* **2014**, *6*, 13183-90.

(28) Ren, H.; Wang, C.; Zhang, J.; Zhou, X.; Xu, D.; Zheng, J.; Guo, S. *Acs Nano* **2010**, *4*, 7169-74.

(29) Liu, M.; Zhang, Q.; Zhao, H.; Chen, S.; Yu, H.; Zhang, Y.; Quan, X. *Chem Commun (Camb)* **2011**, *47*, 4084-6.

(30) Ellman, G. L.; Courtney, K. D.; Andres, V., Jr.; Feather-Stone, R. M. *Biochem Pharmacol* **1961**, *7*, 88-95.

(31) Liu, S.; Zeng, T. H.; Hofmann, M.; Burcombe, E.; Wei, J.; Jiang, R.; Kong, J.; Chen, Y. *Acs Nano* **2011**, *5*, 6971-80.

(32) Perreault, F.; de Faria, A. F.; Nejati, S.; Elimelech, M. *ACS Nano* **2015**, *9*, 7226-36.

(33) Ahmad, A.; Qureshi, A. S.; Li, L.; Bao, J.; Jia, X.; Xu, Y.; Guo, X. *Colloids Surf B Biointerfaces* **2016**, *143*, 490-8.

(34) Liu, X.; Sen, S.; Liu, J.; Kulaots, I.; Geohegan, D.; Kane, A.; Puretzky, A. A.; Rouleau, C. M.; More, K. L.; Palmore, G. T.; Hurt, R. H. *Small* **2011**, *7*, 2775-85.

(35) Zhang, M.; Zhao, Y.; Yan, L.; Peltier, R.; Hui, W.; Yao, X.; Cui, Y.; Chen, X.; Sun, H.; Wang, Z. *ACS Appl Mater Interfaces* **2016**, *8*, 8834-40.

(36) Zhao, Y.; Chen, W. F.; Yuan, C. F.; Zhu, Z. Y.; Yan, L. F. *Chinese J Chem Phys* **2012**, 25, 335-338.

(37) Yang, H. H.; McCreery, R. L. *J Electrochem Soc* **2000**, 147, 3420-3428.

(38) Qu, D. Y. *Carbon* **2007**, 45, 1296-1301.

(39) Jiao, Y.; Qian, F.; Li, Y.; Wang, G.; Saltikov, C. W.; Gralnick, J. A. *Journal of Bacteriology* **2011**, 193 (14), 3662–3665.

(40) Peng, J.; Gao, W.; Gupta, B. K.; Liu, Z.; Romero-Aburto, R.; Ge, L.; Song, L.; Alemany, L. B.; Zhan, X.; Gao, G.; Vithayathil, S. A.; Kaipparettu, B. A.; Marti, A. A.; Hayashi, T.; Zhu, J.-J.; Ajayan, P. M. *Nano Letters* **2012**, 12 (2), 844–849.

(41) Zhao, H.-X.; Wang, Y.-C.; Zhang, L.-Y.; Wang, M. *New Journal of Chemistry* **2015**, 39 (1), 98–101.

(42) Li, D.; Müller, M. B.; Gilje, S.; Kaner, R. B.; Wallace, G. G. *Nature Nanotechnology* **2008**, 3 (2), 101–105.

(43) Paredes, J. I.; Villar-Rodil, S.; Martínez-Alonso A.; Tascón J. M. D. *Langmuir* **2008**, 24 (19), 10560–10564.

(44) Guardia, L.; Villar-Rodil, S.; Paredes, J.; Rozada, R.; Martínez-Alonso, A.; Tascón, J. *Carbon* **2012**, 50 (3), 1014–1024.

(45) Kumar, P. V.; Bardhan, N. M.; Tongay, S.; Wu, J.; Belcher, A. M.; Grossman, J. C. *Nature Chemistry* **2013**, 6 (2), 151–158.

(46) Robertson, J.; O'Reilly, E. P. *Physical Review B* **1987**, 35 (6), 2946–2957.

(47) Bredas, J. L.; Silbey, R.; Boudreaux, D. S.; Chance, R. R. *Journal of the American Chemical Society* **1983**, 105 (22), 6555–6559.

(48) Stankovich, S.; Dikin, D. A.; Piner, R. D.; Kohlhaas, K. A.; Kleinhammes, A.; Jia, Y.; Wu, Y.; Nguyen, S. T.; Ruoff, R. S. *Carbon* **2007**, 45 (7), 1558–1565.

(49) Tuinstra, F.; Koenig, J. L. *The Journal of Chemical Physics* **1970**, 53 (3), 1126–1130.

(50) Du, J.; Wang, H.; Wang, L.; Zhu, S.; Song, Y.; Yang, B.; Sun, H. *Journal of Materials Chemistry C* **2016**, 4 (11), 2235–2242.

(51) Tian, L.; Ghosh, D.; Chen, W.; Pradhan, S.; Chang, X.; Chen, S. *Chemistry of Materials* **2009**, 21 (13), 2803–2809.

(52) Rodriguez, C. E.; Shinyashiki, M.; Froines, J.; Yu, R. C.; Fukuto, J. M.; Cho, A. K. *Toxicology* **2004**, 201 (1-3), 185–196.

(53) Hou, X.-L.; Li, J.-L.; Drew, S. C.; Tang, B.; Sun, L.; Wang, X.-G. *The Journal of Physical Chemistry C* **2013**, 117 (13), 6788–6793.